SANDIA REPORT
SAND2006-4455
Unlimited Release
Printed August 2006

Characterization of Aluminum Honeycomb and Experimentation for Model Development and Validation

Volume II: Honeycomb Experimentation for Model Development and Validation

Terry D. Hinnerichs, Thomas G. Carne, Wei-Yang Lu, Eric C. Stasiunas, Michael K. Neilsen, William Scherzinger, and Brendan R. Rogillio

Prepared by
Sandia National Laboratories
Albuquerque, New Mexico 87185 and Livermore, California 94550

Sandia is a multiprogram laboratory operated by Sandia Corporation, a Lockheed Martin Company, for the United States Department of Energy's National Nuclear Security Administration under Contract DE-AC04-94AL85000.

Issued by Sandia National Laboratories, operated for the United States Department of Energy by Sandia Corporation.

Available to DOE and DOE contractors from
U.S. Department of Energy
Office of Scientific and Technical Information
P.O. Box 62
Oak Ridge, TN 37831

Telephone: (865) 576-8401
Facsimile: (865) 576-5728
E-Mail: reports@adonis.osti.gov
Online ordering: http://www.osti.gov/bridge

Available to the public from
U.S. Department of Commerce
National Technical Information Service
5285 Port Royal Rd.
Springfield, VA 22161

Telephone: (800) 553-6847
Facsimile: (703) 605-6900
E-Mail: orders@ntis.fedworld.gov
Online order: http://www.ntis.gov/help/ordermethods.asp?loc=7-4-0#online

SAND2006-4455
Unlimited Release
Printed August 2006

Characterization of Aluminum Honeycomb and Experimentation for Model Development and Validation

Volume II: Honeycomb Experimentation for Model Development and Validation

Terry D. Hinnerichs, Thomas G. Carne,
Eric C. Stasiunas, Michael K. Neilsen,
William M. Scherzinger, and Brendan R. Rogillio
Solid Mechanics/Structural Dynamics Sciences
Sandia National Laboratories
P.O. Box 5800
Albuquerque, New Mexico 87185-0372

Wei-Yang Lu
Mechanics of Materials
Sandia National Laboratories
P.O. Box 0969
Livermore, California 94551-0969

Abstract

The crush of aluminum honeycomb is a very attractive shock mitigation concept for dissipating large amounts of kinetic energy in laydown weapon systems such as the B61-7 and for shipping container applications. This report is the second of a three-volume set describing aluminum honeycomb crush behavior and model validation. Volume I documents an experimental study of the crush behavior of high-density aluminum honeycombs. Volume III is yet to be published. It will cover the execution of the validation plan described in Volume II. This report, Volume II, describes the need for an improved constitutive model for the large deformation of aluminum honeycomb and is intended to document the procedure that was followed to provide data to calibrate and validate a new constitutive model for large deformation of aluminum honeycomb. The emphasis is on the experimental procedures, but sufficient model description is given to motivate the experiments that were documented herein. The model is first discussed along with the metric, or measuring stick, that will be used to quantify the model's fit with test data. Next, a description of the necessary constitutive tests and the associated test data are shown that are being used to calibrate the model parameters for the new Honeycomb Crush Model. Parameters for the linear elastic portion of the model are described first, followed by the nonlinear crush parameters. Next, a description of the dynamic experiments used to quantify strain rate sensitivity of the honeycomb are given. The final three chapters cover the basic model (single physics or Tier 1) validation and the combined physics or Tier II model validation steps. Finally, all the calibration and validation data are presented.

ACKNOWLEDGMENTS

For Chapter 1, the authors acknowledge the following people associated with the B61 Common Radar Nose development team: Mike Skaggs, Darren Hoke, Vern Willan, Jose Montoya, Jeanne Lewis, and Darrla Giersch.

For Chapter 3, the authors acknowledge Dave Reedy for providing the honeycomb cross-section images and Barry Boughton for providing assistance on the sensitivity analyses.

For Chapter 5, the authors acknowledge the following people: David Kelton for tremendously diligent design work on the dynamic test fixture and for his development of all the test procedures and in performing all the testing; Barry Boughton for assisting in the initial intermediate rate testing and helping to write the data processing software; John Korellis for the design of the constant rate test setup and shear-pin break-off mechanism; and Simon Scheffel for preparing honeycomb specimens.

CONTENTS

FIGURES

TABLES

NOMENCLATURE

AoA	angle of attack
CCD	charge-coupled device
CI	confidence interval
EW	East-West
HCM	Honeycomb Crush Model
MAC	Modal Assurance Criteria
MF	modulus function
MTS	Servo hydraulic material testing system made by MTS Systems Corp.
NS	North-South
OCM	Orthotropic Crush Model
ORM	Orthotropic Rate Model
STS	Stockpile-to-Target-Sequence

EXECUTIVE SUMMARY

The crush of aluminum honeycomb is a very attractive shock mitigation concept for dissipating large amounts of kinetic energy in laydown weapon systems such as the B61-7 and for shipping container applications. This report is the second of a three-volume set describing aluminum honeycomb crush behavior and model validation. Volume I documents an experimental study of the crush behavior of high-density aluminum honeycombs. Volume III is yet to be published. It will cover the execution of the validation plan described in Volume II. This report, Volume II, describes the need for an improved constitutive model for the large deformation of aluminum honeycomb and is intended to document the procedure that was followed to provide data to calibrate and validate a new constitutive model for large deformation of aluminum honeycomb. The emphasis is on the experimental procedures, but sufficient model description is given to motivate the experiments that were documented herein. The model is first discussed along with the metric, or measuring stick, that will be used to quantify the model's fit with test data. Next, a description of the necessary constitutive tests and the associated test data are shown that are being used to calibrate the model parameters for the new Honeycomb Crush Model. Parameters for the linear elastic portion of the model are described first, followed by the nonlinear crush parameters. Next, a description of the dynamic experiments used to quantify strain rate sensitivity of the honeycomb are given. The final three chapters cover the basic model (single physics or Tier 1) validation and the combined physics or Tier II model validation steps. Finally, all the calibration and validation data are presented.

Intentionally Left Blank

CHAPTER 1. INTRODUCTION

Terry Hinnerichs

Problem Description

Sandia National Laboratories needs to utilize modeling and simulation to a greater degree to qualify or certify a nuclear weapon system. The goals for modeling and simulation include reducing the number of required system-level tests and maximizing the value of tests conducted by providing increased understanding of the physical mechanisms that are controlling the performance of the weapon system. Models that can be relied upon for predictive answers are crucial to obtaining these goals. The specific application here is the B61 weapon system life extension program [1].

The B61 mod 7 and mods 3/4/10 are laydown weapon systems, or bombs that are released from a delivery aircraft, retarded in their descent by a parachute, and must survive an impact with ground targets at various impact conditions. Normal and oblique impact angles with velocities up to 150 ft/sec are part of the Stockpile-to-Target-Sequence (STS) requirements [2,3].

The ability to survive these impact conditions is primarily provided by shock mitigation devices designed into the nose of the bomb. These devices include electronic subsystems, foam, foam-filled aluminum honeycomb, or in the latest design for the B61 Common Radar Nose, high-density aluminum honeycomb [4]. The devices dissipate the descending bomb's kinetic energy by converting it to strain energy and heat through the plastic deformation and crush during impact. This document will focus on the high-density aluminum honeycomb design.

A full system model of the B61-7 with the Common Radar Nose has been developed in the PRESTO transient dynamic finite element code [5]. The PRESTO model and the Orthotropic Crush [6] constitutive model (OCM) for the honeycomb work quite well for impact conditions that cause the nose to crush parallel with the principal material axes of the honeycomb inside the nose. However, the OCM cannot accurately predict the behavior of oblique impacts where the honeycomb experiences off-axis crush and includes significant shear stress [7,8]. A new constitutive model has been hypothesized to better handle off-axis crush behavior but requires calibration and validation. Therefore, the specific problem discussed in this report is the validation of this new constitutive model for high-density aluminum honeycomb and ascertaining its accuracy for predicting on-axis and off-axis crush behavior of aluminum honeycomb over the entire STS impact environment for designs similar to the B61 Common Radar Nose.

Aluminum honeycomb is an excellent shock mitigation material for payload protection during impacts. It is orthotropic, with three principal material directions that result due to its composition of corrugated and flat aluminum sheets. These directions – T, the strongest; L, the intermediate strength; and W, the weakest – are labeled in Figure 1-1.

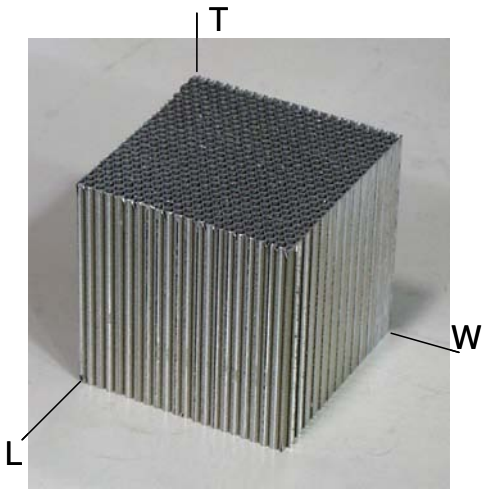

Figure 1-1. Aluminum honeycomb characteristics.

Deliverables

The deliverables for this effort include mechanical crush force and displacement test data to calibrate and validate the new honeycomb constitutive model, and this report to document these data.

Approach

Through many discovery experiments involving off-axis crush and plastic deformation of aluminum honeycomb, as described by Lu in Volume I of this report, a new constitutive model has been developed and is described in the next chapter.

The new honeycomb crush model was used to identify the needed tests to calibrate all of the model's parameters. The details of these uniaxial and biaxial tests and their results are described in Chapters 4, 5, and 6.

A separate matrix of validation experiments was also identified and conducted that includes off-axis crush behavior of honeycomb samples, and these will be used to validate the new model. The results of these Tier I tests are given in Chapter 6.

The model's relevance to the B61 application was more closely evaluated by incorporating the Common Radar Nose geometry and confinement structure into a validation test article design. A matrix of tests was conducted with this coupled-physics or Tier II model validation approach and is described in Chapters 7 and 8.

Material Variability

There are currently only two vendors that fabricate aluminum honeycomb in the United States: the Hexcel Corporation and the Alcore Corporation. Material was procured from both of these suppliers and qualified through compression tests to meet the standard strength requirements for

the B61 Common Radar Nose [9]. Even though both vendors could meet the material specifications, there was significant variability in mechanical properties between suppliers and even within batches of material from a given supplier. Consequently, to reduce one source of variability, material from only one vendor and one batch of material was used for these tests described in this document. Either vendor could have been chosen, but Hexcel was the supplier used.

References

1. Hinnerichs, T.D., *Validation Plan for the B61-3/4/7/10 Radar Nose Assembly Crush Model*, SAND2001-0817. Sandia National Laboratories, Albuquerque, NM, 2001.

2. Stockpile-to-Target Sequence requirements for the B61-7, SB344592.

3. Stockpile-to-Target Sequence requirements for the B61-3/4/10, SB309707.

4. B61 Common Radar Nose design, MC4432.

5. Koteras, J.R., and A.S. Gullerud, *PRESTO User's Guide Version 1.05*, SAND2003-1089. Sandia National Laboratories, Albuquerque, NM, April 2003.

6. Whirley, R.G., B.E. Engelman, and J.O. Hallquist, *DYNA3D Users Manual*, Lawrence Livermore National Laboratory, Livermore, CA, 1991.

7. Lu, W-Y., and T.D. Hinnerichs, Crush of High Density Aluminum Honeycombs (IMECE2001/AMD-25453), *Proceedings of 2001 ASME International Mechanical Engineering Congress and Exposition*, New York, NY, November 11-16, 2001.

8. Lu, W-Y, J. Korellis, and T.D. Hinnerichs, Shear Deformation of High Density Aluminum Honeycombs (IMECE2003-44092), *Proceedings of 2003 ASME International Mechanical Engineering Congress and Exposition*, Washington, D.C., November 15-21, 2003.

9. Honeycomb, Aluminum, Material Specification, SS706955, Issue B, May 1999.

Intentionally left blank

CHAPTER 2. HONEYCOMB CRUSH MODEL

Terry Hinnerichs, Mike Neilsen, and William Scherzinger

This chapter describes the Honeycomb Crush Model (HCM), a newly developed constitutive model for large deformation of aluminum honeycomb. HCM evolved from the Orthotropic Crush Model (OCM) [1], and the more recent Orthotropic Rate Model (ORM), which has been implemented in the PRESTO transient dynamic finite element code [2]. Similar to these earlier models for an orthotropic honeycomb material, the HCM is a multi-surface plasticity model with six yield surfaces.

In the HCM model, the initial honeycomb orientation is defined by the user and used to construct a rotation tensor that defines the honeycomb orientation in the material frame. As the honeycomb is deformed, the material frame rotates due to rigid body rotation or shearing deformation, but the honeycomb orientation in the material frame is assumed to remain unchanged as the honeycomb is deformed. The material frame rotates according to the rotation tensor obtained from the polar decomposition of the deformation gradient [3,4]. A key assumption here is that the honeycomb material axes remain orthogonal during deformation and that the rotation of the honeycomb during deformation is simply given by the rotation tensor as described above. This assumption requires small shear strains and therefore is a weakness of the model when applied to large shear deformation cases. This weakness in the model is a candidate for future improvements to the model.

Elastic response of the honeycomb is assumed to evolve from a linear orthotropic response representative of uncompacted honeycomb to a linear and much stiffer isotropic response representative of fully compacted honeycomb. The linear orthotropic elastic response of the uncompacted honeycomb is given by the following equation,

$$\begin{Bmatrix} \sigma_{tt} \\ \sigma_{ll} \\ \sigma_{ww} \\ \sigma_{tl} \\ \sigma_{lw} \\ \sigma_{wt} \end{Bmatrix} = \begin{bmatrix} E_{tttt} & E_{ttll} & E_{ttww} & & & \\ E_{ttll} & E_{llll} & E_{llww} & & 0 & \\ E_{ttww} & E_{llww} & E_{wwww} & & & \\ & & & E_{tltl} & & \\ & 0 & & & E_{lwlw} & \\ & & & & & E_{wtwt} \end{bmatrix} \begin{Bmatrix} \varepsilon_{tt} \\ \varepsilon_{ll} \\ \varepsilon_{ww} \\ \varepsilon_{tl} \\ \varepsilon_{lw} \\ \varepsilon_{wt} \end{Bmatrix} \qquad \text{(Eq. 2-1)}$$

The elastic moduli for uncompacted 38 pcf aluminum honeycomb were obtained from unit cell simulations, which are described in Chapter 3. The moduli, assumed to vary as a function of the engineering volume strain as the honeycomb is crushed, obtain the crushed isotropic values given in Equation 2-2 (with Lame constants) when the transition parameter in the modulus function (MF) obtains a value equal to 1.0. The MF is a user-defined tabular function that describes the transition from orthotropic to isotropic elastic constants. The values chosen are given in Table 2-1. When the honeycomb is in the undeformed state the transition parameter has a value of 0.0 and the elasticity tensor is equal to the orthotropic elasticity tensor given in Equation 2-1. The honeycomb is fully compacted when the transition parameter reaches a value of 1.0. For intermediate states, a linear combination of the original orthotropic elasticity tensor and the fully compacted isotropic tensor is used. The values given in Table 2-1 define the transition to start at 0.74 volumetric strain and complete at the value of 0.77.

$$\begin{Bmatrix} \sigma_{tt} \\ \sigma_{ll} \\ \sigma_{ww} \\ \sigma_{tl} \\ \sigma_{lw} \\ \sigma_{wt} \end{Bmatrix} = \begin{bmatrix} \lambda+2\mu & \lambda & \lambda & & & \\ \lambda & \lambda+2\mu & \lambda & & 0 & \\ \lambda & \lambda & \lambda+2\mu & & & \\ & & & 2\mu & & \\ & 0 & & & 2\mu & \\ & & & & & 2\mu \end{bmatrix} \begin{Bmatrix} \varepsilon_{tt} \\ \varepsilon_{ll} \\ \varepsilon_{ww} \\ \varepsilon_{tl} \\ \varepsilon_{lw} \\ \varepsilon_{wt} \end{Bmatrix} \quad \text{(Eq. 2-2)}$$

Table 2-1. Modulus function.

Modulus Function	
Volumetric Strain	**Transition Parameter**
-1	0
0	0
0.74	0
0.77	1
1	1

The general form for the yield functions were based on a Schreyer and Zuo [5] study, which showed that interesting coupling exists between the elastic and plastic response of materials and that appropriate yield functions can often be derived from the eigentensors associated with the fourth-order elasticity tensor. The six yield functions for the HCM were based on the six symmetric eigentensors associated with the orthotropic elasticity tensor for this honeycomb and are given in Equation 2-3. The first three yield functions in Equation 2-3 exhibit coupling between the normal stress terms. The last three yield functions in Equation 2-3 control the shear behavior. Klintworth and Stronge [6] showed that yield functions that define the in-plane response of regular hexagonal honeycomb also exhibit coupling between stress terms. The hardening functions were derived based on an observation that the crush strength increases dramatically but the crush load (i.e., engineering stress) in the T direction stays approximately constant as a sample is equal biaxially crushed in the T and L, or T and W directions. Also, these hardening functions allow the material to migrate towards isotropy as it compacts towards solid aluminum. Initially, the hardening functions were implemented in tabular form for flexibility, and some of them remain as tabular functions, but it was found that some of these best-fit tabular functions could be well-represented by analytic functions that greatly simplify the model parameter identification. Detailed descriptions of the parameters and functions are as follows

$$\begin{aligned}
\Psi_T &= \left|a_1\sigma_{TT} + b_1\sigma_{LL} + c_1\sigma_{ww}\right| - TS * H_T(e_{vol}) * G(rate) * TTP(e_{tt}) * TLP(e_{ll}) * TWP(e_{ww}) * SF \\
\text{where : } SF &= TTLP(e_{tl}) * TTWP(e_{wt}) \\
\Psi_L &= \left|a_2\sigma_{TT} + b_2\sigma_{LL} + c_2\sigma_{ww}\right| - LS * H_L(e_{vol}) * G(rate) * LTP(e_{tt}) * LLP(e_{ll}) * LWP(e_{ww}) \\
\Psi_W &= \left|a_3\sigma_{TT} + b_3\sigma_{LL} + c_3\sigma_{ww}\right| - WS * H_W(e_{vol}) * G(rate) * WTP(e_{tt}) * WLP(e_{ll}) * WWP(e_{ww}) \quad \text{(Eq. 2-3)} \\
\Psi_{TL} &= \left|\sigma_{TL}\right| - TLS * H_{TL}(e_{vol}) * G(rate) * TLTLP(e_{tl}) \\
\Psi_{LW} &= \left|\sigma_{LW}\right| - LWS * H_{LW}(e_{vol}) * G(rate) * LWLWP(e_{lw}) \\
\Psi_{WT} &= \left|\sigma_{WT}\right| - WTS * H_{WT}(e_{vol}) * G(rate) * WTWTP(e_{wt})
\end{aligned}$$

where a_1, b_1, c_1, a_2, b_2, c_2, a_3, b_3, and c_3 are material parameters that define the shape of the yield surface. The diagonal terms a_1, b_2, and c_3 are typically set to unity. The other six parameters can be quantified by uniaxial crush tests where the transverse load is measured in addition to the axial load. For the high-density honeycomb considered here, the T and L directions are very strong compared to the L and W directions, respectively, which drives a_2, a_3, and b_3 to zero. For example, a_2 controls the amount of flow in the T direction when there is crushing in the L direction. The remaining three parameters, b_1, c_1, and c_2, will be estimated with the transverse loads measured in uniaxial strain tests.

The first six strength parameters (TS, LS, WS, TLS, LWS, and WTS) specify the initial yield strength values and are modified by the following multiplicative, dimensionless hardening functions, e.g., $H_T(e_{vol})$ or TWP. Separating these values facilitates parametric studies of the input strength uncertainties.

Six tabular hardening functions (H_T, H_L, H_W, H_{TL}, H_{LW}, and H_{WT}) depend only on engineering volume strain, e_{vol}. These functions have a unit value until the volume strain reaches a few percent below the solidification or lockup strain level and then grow from unity to provide the correct lockup during biaxial crush. Strain rate dependence is captured with the function G(rate), which depends only on a scalar measure of the total strain rate.

The six hardening functions, given in Equation 2-4, are based on the concepts of "conservation of strength" and "migration towards isotropy" as the honeycomb cells are compressed.

If the strains are compressive:

$$\begin{aligned} TLP(e_{ll}) &= (1 - E_{STL} * e_{ll}) / (1 + e_{ll}) \\ TWP(e_{ww}) &= (1 - E_{STW} * e_{ww}) / (1 + e_{ww}) \\ LTP(e_{tt}) &= (1 - E_{SLT} * e_{tt}) / (1 + e_{tt}) \\ LWP(e_{ww}) &= (1 - E_{SLW} * e_{ww}) / (1 + e_{ww}) \\ WTP(e_{tt}) &= (1 - E_{SWT} * e_{tt}) / (1 + e_{tt}) \\ WLP(e_{ll}) &= (1 - E_{SWL} * e_{ll}) / (1 + e_{ll}) \end{aligned} \qquad \text{(Eq. 2-4)}$$

If the strains are tensile, all of the functions are set equal to unity, i.e., $TLP = TWP = LTP = LWP = WTP = WLP = 1$. This model is primarily designed for compressive loads and should not be used for large tensile-loaded zones.

The input parameters:

E_{stl}	scales the influence of L normal strain on T-direction strength,
E_{stw}	scales the influence of W normal strain on T-direction strength,
E_{slt}	scales the influence of T normal strain on L-direction strength,
E_{slw}	scales the influence of W normal strain on L-direction strength,
E_{swt}	scales the influence of T normal strain on W-direction strength, and
E_{swl}	scales the influence of L normal strain on W-direction strength.

The values (E_{stl}, E_{stw}, E_{slt}, E_{slw}, E_{swt}, and E_{swl}) are chosen based on equal biaxial crush tests. The "P" in TLP and the other terms ending with "P" implies that these are tabular or analytic functions. The engineering strains, e_{tt}, e_{ll}, and e_{ww}, relate to the honeycomb T, L, and W directions, respectively. The "conservation of strength" concept is based on the rationale that two columns will have the same load-bearing capability regardless of their spacing. Similarly, the aluminum sheets in the honeycomb tend to retain their load-bearing ability as they are compacted. The true stress increases but the engineering stress, load-divided by the original area, remains constant with compaction. "Conservation of strength" is implemented by the denominators in these functions. For example, the denominator in the TLP function expands the yield surface in the T direction based on the reducing cross-sectional area in the L direction due to compaction. This function is equivalent to one over the evolving cross-sectional area in the LW plane.

The numerators in these functions implement the concept that the material is migrating towards isotropy as it locks up. These parameters facilitate ramping the weaker crush strength (e.g., WS) up to the higher value (e.g., TS) to fit TW00 test data.

$TTP(e_{tt})$, $LLP(e_{ll})$, and $WWP(e_{ww})$ are tabular functions of engineering strain in the T, L, and W directions. These functions enable matching the nonlinear uniaxial stress-strain curves in each direction with test data.

Because of uncertainty about the shear behavior, the following hardening functions are defined by tables that modify the given initial strength as a function of shear strain.

$TTLP(e_{tl})$	=	tabular function that modifies the T strength based on the TL shear strain
$TTWP(e_{wt})$	=	tabular function that modifies the T strength based on the WT shear strain
$TLTLP(e_{tl})$	=	tabular function that modifies the TL shear strength based on the TL shear strain
$LWLWP(e_{lw})$	=	tabular function that modifies the LW shear strength based on the LW shear strain
$WTWTP(e_{wt})$	=	tabular function that modifies the WT shear strength based on the WT shear strain

These shear strain dependent functions were set to unity for the results presented in this paper. The shear yield functions, e.g., ψ_{TL}, have little influence on symmetric equal biaxial crush predictions. However, the shear yield functions strongly influence model predictions of non-symmetric equal biaxial and uniaxial off-axis crush. These functions will be quantified based on the off-axis uniaxial tests where shear effects are prevalent.

The HCM was implemented into the PRESTO finite element code [2] and is integrated through time using a closest-point projection algorithm for multi-surface plasticity developed by Simo and Hughes [7].

Material parameters for the new HCM are summarized in Table 2-2. The shear strength values given for TLS, TWS, and LWS are from the vendor, Hexcel Corporation [8], and are considered upper-bound values that will be assessed further during the calibration process.

Table 2-2. Material parameters for 38 pcf honeycomb.

Parameter	Value	Description
Young's Modulus (psi)	40.0×10^5	Young's modulus for isotropic compacted material
Poisson's Ratio	0.30	Poisson's ratio for isotropic compacted material
Modulus TTTT (psi)	24.77×10^5	Moduli for undeformed orthotropic honeycomb
Modulus TTLL (psi)	5.124×10^5	Moduli for undeformed orthotropic honeycomb
Modulus TTWW (psi)	0.617×10^5	Moduli for undeformed orthotropic honeycomb
Modulus LLLL (psi)	14.40×10^5	Moduli for undeformed orthotropic honeycomb
Modulus LLWW (psi)	1.160×10^5	Moduli for undeformed orthotropic honeycomb
Modulus WWWW (psi)	0.709×10^5	Moduli for undeformed orthotropic honeycomb
Modulus TLTL (psi)	14.52×10^5	Moduli for undeformed orthotropic honeycomb
Modulus LWLW (psi)	0.835×10^5	Moduli for undeformed orthotropic honeycomb
Modulus WTWT (psi)	2.622×10^5	Moduli for undeformed orthotropic honeycomb
TX, TY, TZ	i.e., 1,0,0	Orientation of undeformed honeycomb T axis
LX, LY, LZ	i.e., 0,1,1	Orientation of undeformed honeycomb L axis
A1, A2, A3	1.000, 0.000, 0.000	Coupling parameters for TT yield surface
B1, B2, B3	-.001, 1.000, 0.000	Coupling parameters for LL yield surface
C1, C2, C3	-.020, -.015, 1.000	Coupling parameters for WW yield surface
TS (psi)	5872	Initial strength parameter for TT yield surface
LS (psi)	947	Initial strength parameter for LL yield surface
WS (psi)	600	Initial strength parameter for WW yield surface
TLS (psi)	4300	Initial strength parameter for TL yield surface
LWS (psi)	2200	Initial strength parameter for LW yield surface
WTS (psi)	2200	Initial strength parameter for WT yield surface
ESTL	0.2	Hardening in T due to L strain
ESTW	0.0	Hardening in T due to W strain
ESLT	0.0	Hardening in L due to T strain
ESLW	0.0	Hardening in L due to W strain
ESWT	8.0	Hardening in W due to T strain
ESWL	-1.0	Hardening in W due to L strain
Modulus Function	Ftn. Name	Variation in moduli with compaction
Rate Function	Ftn. Name	Variation in strength with strain rate
(i) Function	Ftn. Name	Variation in (i) strength with compaction, where (i) = T,L,W,TL,LW, or WT

Table 2-2. Material parameters for 38 pcf honeycomb (continued).

Parameter	Value	Description
(ijP) Function	Ftn. Name	Variation in (i) strength with (j) strain, where (ij) = TT,LL, or WW
TLTLP Function	Ftn. Name	Variation in TL strength with TL strain
LWLWP Function	Ftn. Name	Variation in LW strength with LW strain
WTWTP Function	Ftn. Name	Variation in WT strength with WT strain
TTWP Function	Ftn. Name	Variation in T strength with TW strain
TTLP Function	Ftn. Name	Variation in T strength with TL strain

References

1. Whirley, R.G., B.E. Engelman, and J.O. Hallquist, "DYNA3D Users Manual," Lawrence Livermore National Laboratory, Livermore, CA, 1991.

2. Koteras, J.R., A.S. Gullerud, *PRESTO User's Guide Version 1.05*, SAND2003-1089. Sandia National Laboratories, Albuquerque, NM, April 2003.

3. Johnson, G.C., and D.J. Bammann, A Discussion of Stress Rates in Finite Deformation Bodies, *Intl. J. Solids and Structures*, Vol. 20, No. 8, pp. 725-737, 1984.

4. Flanagan, D.P., and L.M. Taylor, An Accurate Numerical Algorithm for Stress Integration with Finite Rotations, *Computer Methods in Applied Mechanics and Engineering*, Vol. 62, pp. 305-320, 1987.

5. Schreyer, J.L., and Q.H. Zuo, Anisotropic Yield Surfaces Based on Elastic Projection Operators," *J. Appl. Mech.*, Vol. 62, No. 3, pp. 780-785, 1995.

6. Klintworth, J.W., and W.J. Stronge, Elasto-Plastic Yield Limits and Deformation Laws for Transversely Crushed Honeycomb, Int. *J. Mech. Sci.*, Vol. 30, pp. 273-292, 1988.

7. Simo, J.C., and T.J.R. Hughes, *Computational Inelasticity*, Springer-Verlag, New York, NY, 1998.

8. *Mechanical Properties of Hexcel Honeycomb*, TSB-120, Hexcel Corporation, Dublin, CA, 1992.

CHAPTER 3. HONEYCOMB CHARACTERIZATION: ORTHOTROPIC LINEAR ELASTIC MODEL

Thomas G. Carne, Michael K. Neilsen, and Eric C. Stasiunas

Introduction

At Sandia National Laboratories honeycomb material is used to absorb energy during crush environments. (For information on the crush or plastic behavior of the honeycomb material, see Chapter 2.) However, we still require an understanding of and a modeling capability for the linear-elastic behavior of the material. In this chapter, we discuss the approach developed to characterize orthotropic elastic behavior of the honeycomb material. Due to its construction, the honeycomb should exhibit orthotropic behavior. Our derived constitutive model approximates the honeycomb as a homogeneous material rather than a structural assembly of shells.

The characterization of a constitutive model for an orthotropic material can be difficult due to the nine distinct parameters that must be determined (three each: Young's moduli, shear moduli, and Poisson's ratios). Furthermore, honeycomb is a difficult material to perform standard material tests on because it is not a homogeneous material but a structure; it can be difficult to apply loads without artificially constraining the material or damaging it; and large sample sizes are required for the homogeneous material assumption to be valid. Consequently, rather than using physical experiments and measured test data directly, estimates for the elastic constants for this material were obtained using virtual testing from cell-level computational simulations. In these simulations, a finite element model of a single unit cell was subjected to a variety of small deformations using periodic boundary conditions. The equivalent macroscopic stress and strain were then computed from the tractions applied to the boundary nodes and their deformed positions. These simulations showed that the honeycomb's elastic response was indeed orthotropic. These simulations also generated computational "test data," which were then used to determine the nine independent elastic constants for this material.

Physical tests were required to validate the elastic constants predicted from the cell-level simulations. These tests would need to fully exercise the orthotropic model and either validate or reject the adequacy of the model. Designing appropriate experimental tests is challenging because the honeycomb material must be exercised in a way that the influences of all nine elastic constants are observable within the resulting measured data.

Modal tests, which measure modal frequencies and the corresponding mode shapes of a vibrating structure, have the advantage of deforming structures in complex strain fields, thus exercising multiple aspects of the material model. For the honeycomb model validation, we designed several honeycomb test structures with replications and performed modal tests. The measurement of the numerous modal frequencies and mode shapes of the test structures has the advantage of providing redundant data for the validation of the analytical model. As part of the validation process, finite element analyses of the test structures were performed, using the elastic constants determined from the cell-level simulations to predict the modal frequencies and mode shapes. The sensitivities of the modal frequencies with respect to the elastic parameters were calculated using the analytical model. This calculation allows us to determine which parameters

would actually affect the measured data and to modify the design of the test structures until all the elastic parameters would affect the measured data. The adequacy of the computed elastic constants and the assumed orthotropic model was judged based on whether the model of the honeycomb structure predicted the observed experimental data and whether these data were sensitive to all the material parameters. An earlier report of this effort to validate the honeycomb model was reported in [1].

As part of the validation process, further cell-level computational simulations were performed to investigate uncertainties in the moduli caused by variations from the nominal honeycomb fabrication. Variations in the honeycomb fabrication geometry did indeed cause substantial changes in some of the computed moduli. By properly accounting for fabrication variability, the cell-level simulations accurately reproduced the moduli inferred from the experimental data.

Model Development

The orthotropic properties of aluminum honeycomb depend on cell geometry and on mechanical properties of the materials from which the honeycomb is constructed. The performance of constitutive experiments on honeycomb is complicated because honeycomb is a structure and is not a homogeneous material; thus, the experimental generation of a measurable and uniform stress or strain state is difficult. Due to these experimental limitations, a computational approach was used to determine the elastic properties of aluminum honeycomb. Examining Figure 3-1, three orthogonal directions are indicated: L, W, and T. These are the coordinates that will be used subsequently in referring to the various material properties and the orientation of the honeycomb.

The computational approach proceeded as follows. A finite element model of a spatially periodic unit-cell was developed (Figure 3-1). Note that this spatially periodic model can be replicated and joined with replicas of itself to represent the true geometry of the test specimen.

The components of the orthotropic elasticity tensor for 609 kg/m^3 (38 lb/ft^3) aluminum honeycomb were obtained from six independent simulations. In each simulation, one strain component was given a value of 1.0×10^{-4} and the remaining components were given values of zero. In the first simulation, for example, uniaxial strain in the W direction was applied by reducing the length of Vector LW only. These simulations were performed using JAS-3D [2], a quasi-static finite element code that was developed at Sandia. The mechanical properties used in these simulations for the isotropic constituent materials, 5052 aluminum alloy and adhesive, are given in Table 3-1.

The components of the orthotropic elasticity tensor for the honeycomb obtained from these simulations are given in Figure 3-2. Even though the constituent materials are isotropic, a honeycomb structure is very anisotropic because of its cell geometry. Also, note that the predicted off-diagonal terms in the elasticity matrix are nearly equal but not exactly equal due to small numerical error. This small numerical error was neglected, and the symmetric part of the elasticity tensor was then inverted to obtain components of the elastic compliance tensor (Figure 3-3) from which the corresponding elastic moduli and Poisson's ratios for the honeycomb (Table 3-2) were determined.

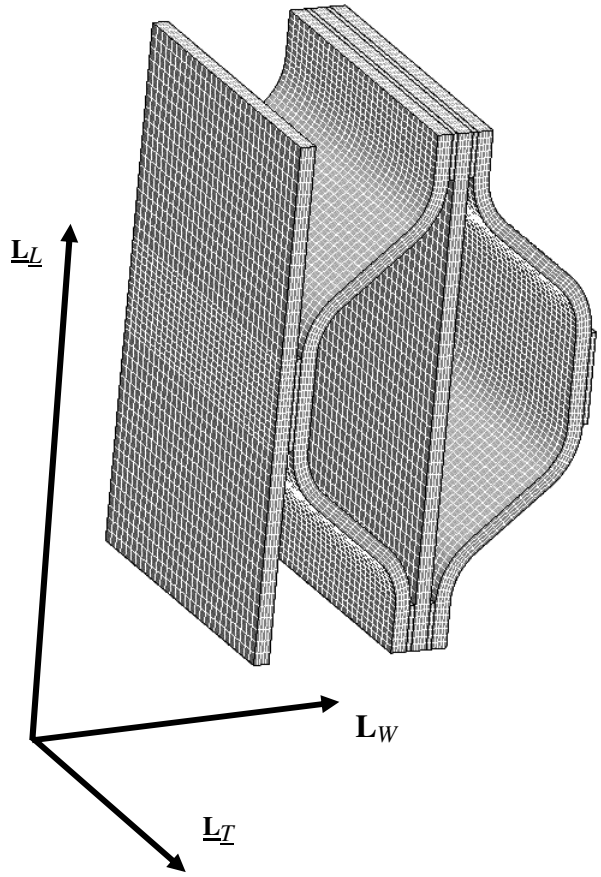

Figure 3-1. Finite element model of a unit-cell of 609 kg/m^3 (38 lb/ft^3) aluminum honeycomb. This honeycomb has a wall thickness of 0.1524 mm and a cell size of 3.175 mm.

Table 3-1. Mechanical properties for constituent materials.

Material	Young's Modulus (Mpa)	Poisson's Ratio
5052 Aluminum	69,655	0.33
Adhesive	2,207	0.35

$$\begin{Bmatrix} \sigma_{WW} \\ \sigma_{LL} \\ \sigma_{TT} \\ \sigma_{WL} \\ \sigma_{LT} \\ \sigma_{TW} \end{Bmatrix} = \begin{bmatrix} 300.8 & 515.8 & 278.7 & & & \\ 524.7 & 8691. & 3042. & & \text{zeros} & \\ 272.9 & 3043. & 15726. & & & \\ & & & 257.7 & & \\ & \text{zeros} & & & 4643. & \\ & & & & & 702.6 \end{bmatrix} \begin{Bmatrix} \varepsilon_{WW} \\ \varepsilon_{LL} \\ \varepsilon_{TT} \\ \gamma_{WL} \\ \gamma_{LT} \\ \gamma_{TW} \end{Bmatrix}$$

Figure 3-2. Components of the orthotropic elasticity tensor for 609 kg/m^3 (38 lb/ft^3) aluminum honeycomb predicted by the unit-cell simulations (units are MPa).

$$\begin{Bmatrix} \varepsilon_{WW} \\ \varepsilon_{LL} \\ \varepsilon_{TT} \\ \gamma_{WL} \\ \gamma_{LT} \\ \gamma_{TW} \end{Bmatrix} = \begin{bmatrix} \frac{1}{E_{WW}} & \frac{-\nu_{LW}}{E_{LL}} & \frac{-\nu_{TW}}{E_{TT}} & & & \\ \frac{-\nu_{WL}}{E_{WW}} & \frac{1}{E_{LL}} & \frac{-\nu_{TL}}{E_{TT}} & & \text{zeros} & \\ \frac{-\nu_{WT}}{E_{WW}} & \frac{-\nu_{LT}}{E_{LL}} & \frac{1}{E_{TT}} & & & \\ & & & \frac{1}{G_{WL}} & & \\ & \text{zeros} & & & \frac{1}{G_{LT}} & \\ & & & & & \frac{1}{G_{TW}} \end{bmatrix} \begin{Bmatrix} \sigma_{WW} \\ \sigma_{LL} \\ \sigma_{TT} \\ \sigma_{WL} \\ \sigma_{LT} \\ \sigma_{TW} \end{Bmatrix}$$

Figure 3-3. Components of the orthotropic compliance tensor.

Table 3-2. Elastic moduli and Poisson's ratios for a 38 lb/ft^3 aluminum honeycomb.

Elastic Moduli	Value (MPa)	Poisson's Ratio	Value
E_{WW}	269.1	ν_{LW}	1.5775
E_{LL}	7366.	ν_{TW}	0.3474
E_{TT}	14628.	ν_{WL}	0.0576
G_{WL}	257.7	ν_{TL}	0.3292
G_{LT}	4643.	ν_{WT}	0.0064
G_{TW}	702.6	ν_{LT}	0.1658

Note in Table 3-2 there are a total of 12 elastic constants listed; however, there are only nine distinct constants because of the three constraint equations that arise due to the assumed symmetry of the compliance tensor. For example, examining Figure 3-3, (ν_{TW} / E_{TT}) = (ν_{WT} / E_{WW}).

Validation Approach

The objective of this work was to validate the unit-cell model's prediction of the mechanical response of bulk honeycomb, when modeled as a continuum. This validation approach uses concepts from parameter estimation methods, including observability, to help define the procedure. As will be further developed in this section, an aspect or a parameter of a model cannot be validated unless it can be observed in the test data. Quantifying this observability is the central feature of the validation approach.

The orthotropic continuum model cannot be considered completely validated unless all the material parameters have been shown to be correctly determined. One could perform material tests on the honeycomb and attempt to directly measure the nine unique material properties, but there are difficulties in performing material tests on honeycomb material due to fixturing requirements, which impose constraints on the material. A model validation approach was used

rather than constitutive material testing. The validation technique exploits the global influence that the elastic constants will have on a structure's natural modes of vibration. In this technique, one or more test structures are designed and built that contain the honeycomb and other well-characterized materials (e.g., steel). We experimentally determine the test structures' mode shapes and modal frequencies and compare the modal quantities' predictions from a finite element analysis utilizing the proposed orthotropic material model. Both the modal frequencies and the mode shapes are influenced by the elastic constants. However, depending on the design of the test structure and the particular elastic constant, the modal frequencies are typically much more sensitive to the parameters than are the mode shapes. The modal frequencies can also be measured very precisely. Without even using the interpolation that modal parameter estimation provides, uncertainties less than 0.2 percent are easily achieved.

There are a number of advantages to using modal testing as an experimental validation procedure as compared to traditional material testing. For a particular test structure, a number of modes (five to 20) can be measured, thus producing more independent test data from a single test structure to validate the model. Further, the modes of vibration would typically be influenced by several of the elastic constants, thus providing overlapping validation paths for the elastic constants. Finally, with modal testing, the structure can be supported very softly with elastic cords, thus accurately simulating free boundary conditions. This is in contrast with material testing, for which the structure needs to be gripped with some fixture in order to apply loads creating some unknown or difficult to simulate boundary conditions. Of course, the modal tests do deform the honeycomb dynamically rather the statically; but the assumed model is linear orthotropic elastic and is not sensitive to variations in strain rate.

There is one difficulty in using modal test data for model validation, although this difficulty is a fundamental issue for any type of model validation. To validate an entire model so that the model will be predictive for any loading condition appropriate to the scope of the model, the model must be tested in such a way that all aspects of the model can be observed. If a material were isotropic elastic, for example, one would need to perform tests such that both the Young's modulus as well as the shear modulus affected the results. One cannot just validate the Young's modulus and assume that the model is valid. Obviously, with large, complicated structural models, exercising every aspect of the model is impossible. For the honeycomb, we would like to fully validate the orthotropic elastic model within its linear elastic scope; thus tests must be designed such that the experimental data are affected to some significant degree by all nine of the material parameters.

To ascertain whether the assumed model's modal data (frequencies or shapes) are affected significantly by a material parameter, one can use the finite element model to compute the sensitivities of the modal data with respect to the material parameters, that is, the partial derivatives of the data with respect to the parameters. Some finite element codes have standard routines to compute the sensitivities, such as NASTRAN and Salinas [3,4]; otherwise, one can use finite differences. Using the computed sensitivities, one can create a sensitivity matrix,

$$\boldsymbol{S}_{ij} = \partial \omega_i \big/ \partial p_j, \qquad \text{(Eq. 3-1)}$$

where ω represents the modal data and p is a material or geometric parameter of the model. This sensitivity matrix could include both frequency and mode shape data and could use data from multiple test structures. The parameters, p, are typically viewed as material parameters, but they can also be geometric or fabrication parameters of the honeycomb. For example, the thickness of the adhesive layer between the aluminum sheets may be uncertain, and the measured data could be sensitive to this parameter as well.

If we use the sensitivity matrix in a Taylor series expansion of the modal data as a function of the parameters, we obtain

$$\omega(p) = \omega(p_o) + \boldsymbol{S} * \Delta p + h.o.t., \qquad \text{(Eq. 3-2)}$$

where p is the vector of parameters, p_o is the nominal value of the parameter vector, $\boldsymbol{S}$ is the sensitivity matrix, Δp is the change in parameter vector, and *h.o.t.* refers to higher-order terms in ωp. The $\omega(p)$ can be taken as the experimental data and the $\omega(p_o)$ as the analysis data, computed at the assumed values of the parameters. Dropping the *h.o.t.*, one can rearrange (Eq. 3-2) to appear as

$$\boldsymbol{S} * \Delta p = \Delta\omega, \qquad \text{(Eq. 3-3)}$$

where $\Delta\omega$ is $(\omega(p) - \omega(p_o))$, the vector of experimental data minus the analysis data. Now if the model is perfectly validated by the test data, the $\Delta\omega$ will be zero or nearly zero. Obviously, there will be some errors due to uncertainty in the fabrication of the test structures and the estimation of the experimental modal frequencies. However, even if the right-hand side of Equation 3-3 is zero, one cannot assume that $\Delta p = 0$, uniquely, unless the S matrix is full rank, that is, not singular. If S were singular, then all of the components of Δp would not necessarily have to equal zero. Consequently, one would not have fully validated the complete parameter vector, even if $\Delta\omega = 0$.

For $\boldsymbol{S}$ to be full rank, the number of rows (data) needs to be at least equal to the number of columns (parameters). In fact, we would like to have more data than parameters so that Δp is over-determined with redundant data. The over-determined equations allow one to solve Equation 3-3 using a least-squares method (pseudo-inverse) that will reduce the effects of random errors in the measured data. Further, even if $\boldsymbol{S}$ is full rank, we actually require that the condition number of the matrix $\boldsymbol{S}$ must not be too large. If the condition number of $\boldsymbol{S}$ is too large, then even though all the parameters affect the frequencies, the effects of some of the parameters may be so small that they may not be observable given the uncertainties of the test data. Note that because the elastic moduli and the Poisson's ratio have such different numerical values, and the data can have much different values, one needs to keep the sensitivity matrix well scaled by normalizing the parameters and the data so that their nominal values are unity.

Now, assuming we have measured and computed more data than parameters, we can solve Equation 3-3 using the least squares method. The data on the right-hand side of Equation 3-3 will contain some random errors, due to measurement and fabrication errors. Assuming the errors in $\Delta\omega$ are independent and with mean error σ, then the covariance matrix associated with

the parameters, Δp, is $\sigma^2(S^TS)^{-1}$ [5]. The diagonal elements of this covariance matrix are the variances of the components of the parameter vector [5]. Thus, if a diagonal element of $(S^TS)^{-1}$ is large, we cannot have confidence in the computed value of the corresponding component of Δp.

Consequently, even if $\Delta\omega$ is very small or zero, unless each diagonal element of $(S^TS)^{-1}$ is reasonably sized (for example, less than a hundred), the parameters have not been validated, and the validation experiments are inadequate to fully validate the model. Thus, for the design of the validation test structures, one needs to obtain the sensitivities through finite element analysis to determine if the experiments exercise all the parameters sufficiently.

This is the approach followed in designing the test structures used to validate the model. After a number of proposed designs, we determined that we could not obtain good sensitivities using a single test structure, so we designed and fabricated three different structures to validate the computationally generated elastic moduli. These test structures consisted of a rectangular section of 50 mm × 50 mm × 200 mm aluminum honeycomb with 50 mm × 50 mm × 50 mm steel blocks bonded to each end with a very thin layer of epoxy as shown in Figure 3-4. The three designed structures are designated as the T, L, and W configurations—indicating the axial direction of the honeycomb material.

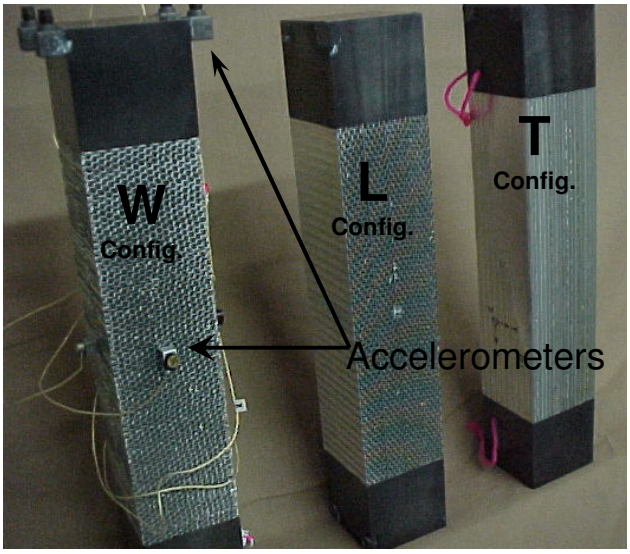

Figure 3-4. Test articles used for modal testing.

Using the finite element analysis as a guide, seven modal frequencies were selected for use as the experimental data. The modes selected were: a fundamental twisting mode, an axial mode, and five bending modes (two in the stiff direction and three in the softer direction). Figure 3-5 shows the mode shapes as computed from the analysis. There were seven modal frequencies for each of three structures for a total of 21 measured data. However, even with 21 measurements, the sensitivity matrix was very poorly conditioned because the Poisson's ratios were not well observed in the data. In order to observe the Poisson's ratios, mode shape data were required.

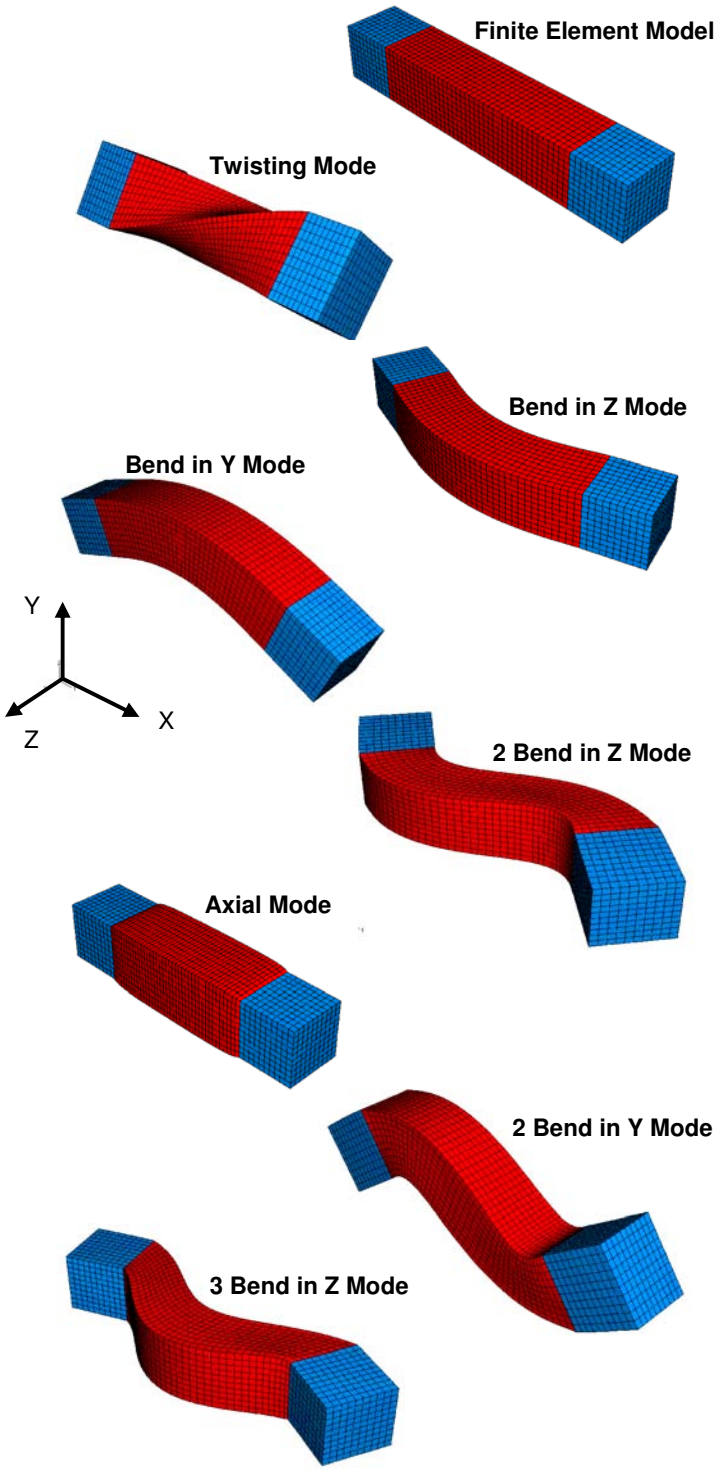

Figure 3-5. Finite element model and mode shapes associated with the seven lowest frequencies.

Rather than using an entire mode shape or a global measure of the mode shape such as Modal Assurance Criteria (MAC), specific components were identified as being very sensitive to the Poisson's ratios. Specifically, we used the two lateral displacements at the center of the honeycomb surface for only the axial mode. In Figure 3-4, one can see an accelerometer attached to the honeycomb surface for measuring that specific mode shape coefficient. We actually measured the lateral displacements on all four sides of the honeycomb and the axial displacement of both steel masses and computed the ratios of the lateral strains to axial strain. Consequently, we now had seven frequencies and two strain shape ratios for each structure for a total of 27 measured data to validate the nine unique material parameters.

The sensitivities of the measured data to the material parameters reveal clearly the importance of the various measured quantities. Table 3-3 is the sensitivity matrix for the T-configuration test structure. The sensitivities have been normalized with respect to both the measured data and the nominal value of the material parameter, then multiplied by 100 and rounded to the nearest integer to give a percent sensitivity. The material parameters vary across the columns while the measured mode shape data vary with the rows. The first seven rows are the modal frequencies with BZ and BY indicating bending modes in the two orthogonal directions. The last two rows are the ratios of the lateral strains to the axial strain for the axial mode (Figure 3-5) obtained from the mode shape coefficients.

Table 3-3. Sensitivity matrix for the T-configuration structure.

	E_T	E_w	E_L	V_{Tw}	V_{TL}	V_{wL}	G_{Tw}	G_{LT}	G_{wL}
Twist	4	0	0	0	0	0	30	14	0
1 BZ	43	0	0	0	0	0	6	0	0
1 BY	49	0	0	0	0	0	0	1	0
2 BZ	23	0	0	0	0	0	24	0	0
Axial	49	0	0	0	0	0	0	0	0
2 BY	40	0	0	0	1	0	0	8	0
3 BZ	15	0	0	0	1	0	32	0	0
L / T	-3	1	0	-1	103	-2	0	0	0
W/ T	9	-11	0	102	-1	-1	1	0	0

Examining Table 3-3, one can see that for this T-configuration test structure most of the data are very sensitive to E_T, with the exception of the twisting mode and the two strain ratios. However, the twisting mode is sensitive to two of the shear moduli, as expected. As an example, note that the axial mode has a sensitivity of 49 with respect to the E_T modulus. Thus, for a 10-percent change in the modulus, one would get a 4.9-percent change in the frequency. Furthermore, one can note that the axial mode frequency is basically not sensitive to any of the other parameters. Examining the two strain ratios, we see that they are each very sensitive to one of the Poisson's ratios. In fact, they are each approximately 100 percent sensitive to one of the Poisson's ratio, showing that these mode shape data are very revealing of the Poisson's ratios.

The sensitivity matrices for the other configurations, L and W, appear similar to that for the T configuration. The axial and bending modal frequencies are very sensitive to the Young's modulus aligned with the axis of the structure; the twisting modal frequency is sensitive to two of the shear Moduli; and the strain ratios again are approximately 100 percent sensitive to one of the Poisson's ratios. The only difference for these two configurations is that the strain ratios were also sensitive to the Young's moduli. Combining all three sensitivity matrices into one creates a very well-conditioned matrix with a condition of 14.0.

We can now examine the diagonal elements of the $(S^TS)^{-1}$ matrix, which reveals the relative uncertainty in the material parameters due to their observability in the measured data. The material parameters are in the same order as appears in Table 3-3. The vector of the diagonal elements is

$$\text{diag}(S^TS)^{-1} = [0.67, 0.61, 0.67, 0.65, 0.69, 0.69, 4.6, 3.7, 3.1].$$

We see that the first six components are all less than 1.0, so the Young's moduli and Poisson's ratios can be identified well from the data. The last three parameters, the shear moduli, are less well identified. These parameters were only sensitive to the frequencies of the twisting modes, so the shear moduli are less observable in the data. Conversely, the Poisson's ratios were very well observed even though only the strain ratios were significantly sensitive to them.

Experimental Measurements

As outlined in the Validation Approach section, seven modal frequencies were measured for each of the three structural configurations for a total of 21 frequencies. These frequencies ranged from 237 Hz to 4101 Hz. Based on the frequency resolution, the frequencies were measured precisely with uncertainties one part in five hundred. Three replicated articles were tested for each of the three configurations using a total of nine different assemblies. The data reported here are the mean of the data along with the 95 percent confidence limits on the mean (2 x (standard deviation)/$\sqrt{3}$) [6]. The uncertainty in the measured modal frequencies was dominated by the variation in the three replicates of the hardware.

In addition to the modal frequencies, particular mode shape coefficients were also measured for the axial mode for each of the three structural configurations. Four lateral mode shape coefficients were measured at the center of each of the honeycomb surfaces (see Figure 3-4) along with the axial shape coefficients for the steel masses. The opposite lateral coefficients were subtracted, and then divided by two to eliminate the small amount of bending that existed in the axial mode. This result was then divided by the axial coefficient to produce a mode shape ratio, and then multiplied by four (200 mm divided by 50 mm) to produce the strain ratio desired for comparison with the analysis results. The uncertainty in the strain ratio was much greater than for the modal frequency data. In fact, as will be shown later, the strain ratio data for the W-configuration contained very large uncertainty. As with the modal frequencies, the uncertainty in the mode shape ratios was dominated by variation in the test structures.

Other factors that contribute to uncertainty in modal testing data are the boundary conditions and the mass loading effects of the accelerometers and their attached cables. To address the boundary condition factor, all the testing was performed using very soft support conditions to simulate free boundary conditions. Figure 3-6 shows one of the test structures supported in the

free condition, using soft elastic cords. The highest "rigid body" mode of the free support condition was approximately 3 Hz, well below one-tenth of the lowest elastic modal frequency, thus not affecting the measured modal frequencies [7]. The mass loading effects of the soft support was evaluated by testing the structure with two supports, and then with only one support. A difference in the modal frequencies could not be detected, confirming that the mass of the supports had a negligible effect on the measured data.

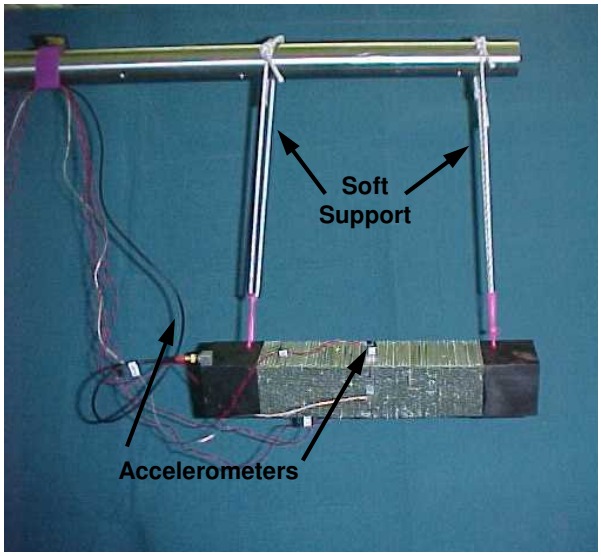

Figure 3-6. Testing configuration showing support conditions, accelerometers, and cables.

The mass of the accelerometers and their attached cables was a concern due to their relative mass compared with that of the test structure. Initial modal testing was performed with four tri-axial accelerometers (6.6 grams each) on each of the steel blocks with four lightweight uni-axial accelerometers (1.3 grams each) on the honeycomb surfaces. The total accelerometer and effective cable mass was 2.5 percent of the total structural mass. The seven mode shapes were identified using this fairly complete instrumentation, but final results were obtained using just a single tri-axial and the four uni-axial accelerometers, which created a mass loading of only 0.5 percent. The estimated effective mass of the cables was calculated by comparing the modal frequencies of the fully instrumented structure with those of the lightly instrumented structure. For this application, approximately two inches of the cable was mass loading the structure, which is not insignificant, compared to the mass of the accelerometer.

Geometric and mass uncertainty in the test structures was also a concern. As mentioned previously, three replicates of each of the three structural configurations were fabricated and tested. Also, the test structures were analytically modeled assuming nominal dimensions and densities. The geometric dimensions were tightly controlled and measured, resulting in dimensional uncertainly of less than 0.05 percent. The mass and resulting density of the honeycomb material varied significantly even though the honeycomb was machined from the same large block. For the nine honeycomb pieces, the average mass was 313 grams with individual masses varying from 307 grams to 320 grams. This variation in mass will obviously cause a variation in the structural material properties of the honeycomb. The steel blocks were very consistent with mass variations of one part in a thousand.

Table 3-4 lists the 27 measured modal frequencies along with the predictions from the original finite element model, using the initial material properties computed from the cell-level modeling. All of the measured frequencies have uncertainties shown in the table, which have been converted to a percent of their mean frequency. These uncertainties are almost entirely due to the variations in the hardware, as measurement uncertainty was small compared to hardware variation. The differences between the mean measured frequencies and the model predicted frequencies are listed in the last column. The measured frequency is higher in every case than the predicted frequency. For the T and L configurations, the differences are fairly small, particularly in view of the uncertainty in the measured frequencies, although there exists a clear bias error in the predictions. For the W configuration, the differences are much larger with the maximum difference of 24 percent for the axial mode. We know that the axial mode in the W configuration is very sensitive to E_{ww}, so it appears that the unit-cell model has not predicted some of the material parameters correctly. These results led us to re-examine some of the geometry or fabrication uncertainties in the unit-cell model.

Table 3-4. Comparison of the measured and predicted frequencies generated with original computational model.

HC Conf	Mode Shape	Measured Frequency	Model Frequency	Diff. (%)
T	Twisting	935 ± 3%	884.	5
T	Bend in Z	1379 ± 2%	1347.	2
T	Bend in Y	1456 ± 1%	1438.	1
T	2 Bend in Z	2843 ± 2%	2645.	7
T	Axial	3087 ± 1%	2989.	3
T	2 Bend in Y	3721 ± 2%	3639.	2
T	3 Bend in Z	4101 ± 2%	3846.	6
L	Twisting	647 ± 3%	622.	4
L	Bend in Z	984 ± 3%	933.	5
L	Bend in Y	1099 ± 2%	1041.	5
L	2 Bend in Z	1791 ± 3%	1721.	4
L	Axial	2326 ± 3%	2131.	8
L	3 Bend in Z	2543 ± 3%	2478.	3
L	2 Bend in Y	2909 ± 3%	2757.	5
W	Bend in Z	237 ± 6%	208.	12
W	Bend in Y	254 ± 6%	211.	17
W	Twisting	485 ± 1%	447.	8
W	Axial	538 ± 6%	407.	24
W	2 Bend in Z	664 ± 2%	556.	16
W	2 Bend in Y	729 ± 3%	572.	22
W	3 Bend in Z	1286 ± 2%	1147.	11

Fabrication Uncertainties

The finite element model shown in Figure 3-1, that was used to generate the initial predictions for the elastic moduli, is an idealized version of the actual honeycomb geometry. Photographs of typical cross-sections of the actual honeycomb are shown in Figure 3-7. These photographs show that the thickness of the adhesive used between the aluminum sheets can vary in thickness from 0.01 to 0.15 mm and that the length of the adhesive joint is also quite variable. The thickness of the aluminum sheets was also found to be thicker than the specified 0.15 mm (6 mils).

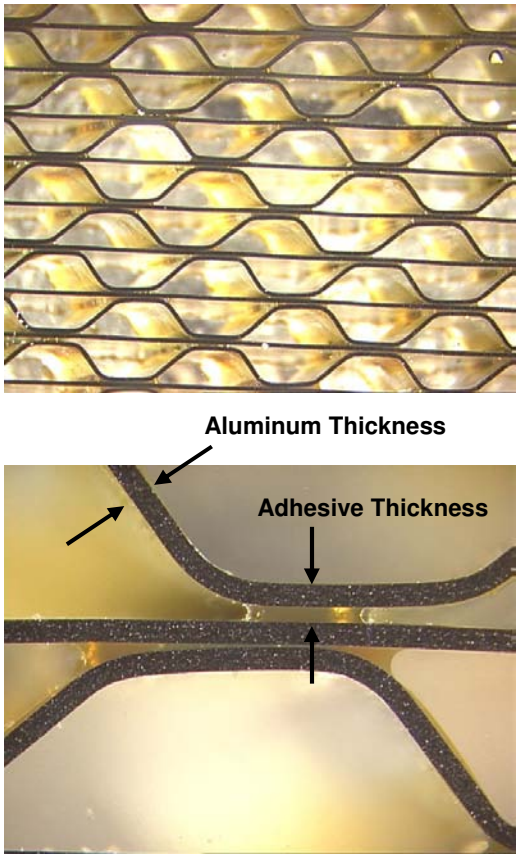

Figure 3-7. Cross-section images through the honeycomb.

To understand the effects that these geometric variables could have on the elastic properties of the honeycomb, a series of finite element analyses were performed using unit-cell models similar to the model shown in Figure 3-1 but with geometric variations.

In the first geometric-variation analysis, the aluminum honeycomb thickness was increased from 0.15 to 0.18 mm. Results from this simulation showed that all of the elastic moduli would increase substantially when the aluminum sheet thickness is increased (Table 3-5).

In the next geometric analyses, the aluminum honeycomb thickness was held constant at the specified 0.1524 mm but the adhesive thickness was reduced by 50 percent. Results from this simulation showed that some of the elastic moduli (E_{WW}, E_{LL}, and G_{TW}) will increase substantially when the adhesive thickness is decreased (Table 3-6). However, the G_{WL} shear

modulus does decrease when the adhesive thickness is decreased, and E_{TT} and G_{LT} will be essentially unaffected by this change.

Table 3-5. Effect of aluminum sheet thickness on the predicted elastic moduli and Poisson's ratios.

Material Parameter	Original Model	Increased Sheet Thickness
Aluminum Thickness	**0.1524 mm**	**0.1778 mm**
E_{WW} (MPa)	269.1	366.9
E_{LL} (MPa)	7366.	8588.
E_{TT} (MPa)	14628.	17053.
G_{WL} (MPa)	257.7	455.0
G_{LT} (MPa)	4643.	5434.
G_{TW} (MPa)	702.6	803.0
v_{LW}	1.5775	1.6054
v_{TW}	0.3474	0.3767
v_{WL}	0.0576	0.0686
v_{TL}	0.3292	0.3254
v_{WT}	0.0064	0.0081
v_{LT}	0.1658	0.1639

Table 3-6. Effect of adhesive thickness on the predicted elastic moduli and Poisson's ratios.

Material Parameter	Original Model	Increased Sheet Thickness
Aluminum Thickness	**0.0508 mm**	**0.0254 mm**
E_{WW} (MPa)	269.1	290.8
E_{LL} (MPa)	7366.	7481.
E_{TT} (MPa)	14628.	14627.
G_{WL} (MPa)	257.7	209.1
G_{LT} (MPa)	4643.	4639.
G_{TW} (MPa)	702.6	789.3
v_{LW}	1.5775	1.5435
v_{TW}	0.3474	0.3300
v_{WL}	0.0576	0.0600
v_{TL}	0.3292	0.3303
v_{WT}	0.0064	0.0066
v_{LT}	0.1658	0.1689

In the final geometric analyses, the length of the adhesive layer was increased from its nominal value of 0.9685 mm to 1.200 mm. Results from this simulation showed that the elastic moduli E_{WW}, E_{LL}, and G_{TW} are sensitive to this change but that the other elastic moduli are rather insensitive to this change (Table 3-7).

Table 3-7. Effect of adhesive length on the predicted elastic moduli and Poisson's ratios.

Material Parameter	Original Model	Increased Sheet Thickness
Aluminum Thickness	**0.9685 mm**	**1.200 mm**
E_{WW} (MPa)	269.1	462.0
E_{LL} (MPa)	7366.	7534.
E_{TT} (MPa)	14628.	14636.
G_{WL} (MPa)	257.7	262.3
G_{LT} (MPa)	4643.	4651.
G_{TW} (MPa)	702.6	807.4
ν_{LW}	1.5775	1.4399
ν_{TW}	0.3474	0.3521
ν_{WL}	0.0576	0.0883
ν_{TL}	0.3292	0.3277
ν_{WT}	0.0064	0.0111
ν_{LT}	0.1658	0.1687

These geometric-variation analyses clearly show that small changes in the geometry of the representative unit-cell can have a dramatic effect of the predicted material parameters for aluminum honeycomb. The images of the honeycomb cross sections shown in Figure 3-7 also show that there is significant uncertainty in exactly what geometric parameters should be chosen for a representative unit-cell.

Therefore, it was decided that the only way to generate accurate estimates for the honeycomb elastic moduli and to create a truly representative unit-cell model would be to perform sensitivity analyses with the unit-cell's geometric parameters as the independent variables. This sensitivity analysis required several steps. First, a variety of unit-cell models were generated with variations in one of the independent variables: aluminum thickness, adhesive thickness, or adhesive length. The elastic moduli were then computed for each of these unit-cell models. Next, an eigenanalysis of the three experimental structures was performed with each set of elastic moduli. Modal frequency results from these eigenanalyses were then used to construct a sensitivity matrix for the variation in frequency associated with a given variation in one of the independent geometric parameters. Using the least-squares process outlined in the previous section, the sensitivity matrix was then used to estimate the geometric parameters that would minimize the frequency error.

Results from this process indicated that the adhesive thickness for the model should be changed from 0.0508 mm to 0.02495 mm, the aluminum thickness should be changed from 0.1524 mm to 0.1644 mm, and the adhesive length should be increased from 0.9685 mm to 1.053 mm. A new unit-cell model was constructed using the geometric parameters obtained from the sensitivity study. This model was then used to generate a new estimate for the elastic moduli (Table 3-8). As one can see, these moduli are significantly different than the moduli generated using the original unit-cell model. Next, these new moduli were used to generate new modal frequency estimates in eigenanalyses of the three test structures. Results from these eigenanalyses, shown in Table 3-9, reveal that the differences in the frequencies are dramatically reduced. Comparison of Table 3-9 with Table 3-4 shows a tremendous improvement with reductions in the differences for every measured frequency. The largest difference has been reduced from 24 percent to 6 percent. Also shown in Table 3-9 are the comparisons of the strain ratios derived from the mode shape data. The strain data were not used in the sensitivity analysis, but the difference between the model and the measurements is small relative to the uncertainty in the measurement. This good correlation is particularly reassuring, because correlation with the strain ratios is required to have confidence in the Poisson's ratios. We know from the sensitivity analysis that the Poisson's ratio is not observed significantly in the frequencies alone.

Table 3-8. Effect of the new identified geometric parameters on the predicted elastic moduli and Poisson's ratios.

Material Parameter	**Original Model**	**Increased Sheet Thickness**
Aluminum Thickness	**0.1524 mm**	**0.1644 mm**
Adhesive Thickness	**0.0508 mm**	**0.02495 mm**
Adhesive Length	**0.9685 mm**	**1.053 mm**
E_{WW} (MPa)	269.1	423.1
E_{LL} (MPa)	7366.	8141.
E_{TT} (MPa)	14628.	15781.
G_{WL} (MPa)	257.7	288.0
G_{LT} (MPa)	4643.	5007.
G_{TW} (MPa)	702.6	904.2
v_{LW}	1.5775	1.4890
v_{TW}	0.3474	0.3307
v_{WL}	0.0576	0.0774
v_{TL}	0.3292	0.3291
v_{WT}	0.0064	0.0089
v_{LT}	0.1658	0.1698

Table 3-9. Comparison of the experimental and predicted frequencies generated with model constructed using the geometric parameters identified from the sensitivity study.

HC Conf	Mode Shape	Measured Frequency	Model Frequency	Diff. (%)
T	Twisting	935 ± 3%	966.	3
T	Bend in Z	1379 ± 2%	1381.	0
T	Bend in Y	1456 ± 1%	1461.	0
T	2 Bend in Z	2843 ± 2%	2850.	0
T	Axial	3087 ± 1%	3096.	0
T	2 Bend in Y	3721 ± 2%	3732.	0
T	3 Bend in Z	4101 ± 2%	4169.	2
T	L / T strain	0.34 ± 29%	0.33	3
T	W / T strain	0.41 ± 5%	0.38	7
L	Twisting	647 ± 3%	653.	1
L	Bend in Z	984 ± 3%	956.	3
L	Bend in Y	1099 ± 2%	1071.	3
L	2 Bend in Z	1791 ± 3%	1797.	0
L	Axial	2326 ± 2%	2235.	4
L	3 Bend in Z	2543 ± 3%	2576.	1
L	2 Bend in Y	2909 ± 3%	2862.	2
L	T / L strain	0.21 ± 10%	0.17	17
L	W / L strain	1.59 ± 9%	1.64	3
W	Bend in Z	237 ± 6%	251.	6
W	Bend in Y	254 ± 6%	254.	0
W	Twisting	485 ± 1%	483.	0
W	Axial	538 ± 6%	510.	5
W	2 Bend in Z	664 ± 2%	670.	1
W	2 Bend in Y	729 ± 3%	695.	5
W	3 Bend in Z	1286 ± 3%	1333.	4
W	T / W strain	0.02 ± 50%	0.009	55
W	L / W strain	0.09 ± 44%	0.08	11

This dramatic improvement in the correlation between all the measured and predicted data has come about only by adjusting three uncertain geometric parameters in the unit-cell model, adhesive thickness, adhesive length, and the aluminum thickness. The results shown in Table 3-9 clearly establish that the improved unit-cell model predicts the elastic moduli, which when used in the finite element model of the test structures produces the measured modal

frequencies and strain ratios. Also, the increased thickness of the aluminum causes an increase in the density of the honeycomb, which now agrees well with the measured density.

In spite of the fine agreement achieved between the measured and the predicted frequencies, we possibly could improve the estimation of the materials parameters further by performing sensitivity analysis directly with variations of the elastic moduli and Poisson's ratios, rather than the geometric parameters. We computed the sensitivity matrix for variations in both the frequencies and the stain ratios for changes in the nine unique material parameters listed in Table 3-3 and computed the changes in those parameters that would minimize the error in both frequencies and the axial strain ratio. Using those new parameters in eigenanalyses for the three configurations did produce a reduction in error. It reduced the rms error from 4.5 percent to 2.2 percent, mostly affecting the strain ratio data. However, these refinements in the material parameters have created such minor improvements in the predicted data, which are near the uncertainties of the measured data, that one can hardly justify the changes from a statistical view.

Conclusions

A unit-cell finite element model was created and subjected to a variety of strains in order to predict the structural response and determine the orthotropic material properties of a high-density aluminum honeycomb. The associated equivalent macroscopic stress for the structure was then computed and used to generate estimates for the orthotropic elastic moduli.

Concepts from estimation methods were incorporated into the model validation approach. In order to claim the model was validated, we required that uncertain aspects or parameters in the model were clearly observed in the experimental data. Using sensitivity analysis on the results of finite element analyses, the observability of the uncertain parameters could be quantified. Further, the same concepts were used to design three honeycomb test structures and the measurements required so that one could validate the entire orthotropic model of the honeycomb (nine parameters) using modal analysis data.

Three replicates of each of the three test structures were fabricated and tested to obtain the required modal frequencies and mode shapes. The means and the 95 percent confidence limits have been computed for the measured data. Using another sensitivity analysis based on changes in the modal frequencies due to small changes in uncertain geometric parameters of the unit-cell, we computed the variations in those parameters that would minimize the difference between the model predictions and the measurements. The refined unit-cell model produced both frequency and strain ratio data, which are very close to the measured data, in spite of not using the strain data in the sensitivity analysis. The unit-cell model is now a high-confidence model regarding the material parameters it produces. One can use the unit-cell model for improving the honeycomb design or for performing computational, virtual experiments including honeycomb crush.

References

1. Lopez, F.P., M.K. Neilsen, T.G. Carne, and C.C. O'Gorman, Development and Validation of an Orthotropic Constitutive Model for Aluminum Honeycomb, *Proceedings of the 2001 SEM Annual Conference*, Portland, OR, June 2001.

2. Blanford, M.L., JAS-3D, *A Multi-Strategy Iterative Code for Solid Mechanics Analysis, User's Instructions, Release 1.6*, Sandia National Laboratories, Albuquerque, NM, August 1998.

3. Bhardwaj, M., G. Reese, B. Driessen, K. Alvin, and D. Day, Salinas - An Implicit Finite Element Structural Dynamics Code Developed for Massively Parallel Platforms, *AIAA 2000-1651, 41st AIAA SDM Conference*, Atlanta, GA, April 3-6, 2000.

4. Alvin, Kennth F., Garth M. Reese, David M. Day, and Manoj K. Bhardwaj, Static, Transient, and Modal Sensitivity Analysis Using Advanced Solvers and Massively Parallel Computing, *AIAA 200-1652, 41st AIAA/ASME/ASCE/AHS/ASC SDM Conference*, Atlanta, GA, April 3-6, 2000.

5. Branham, Richard L., Jr., Scientific Data Analysis, An Introduction to Overdetermined Systems, Springer-Verlag Inc., New York, NY, 1990.

6. Coleman, Hugh W., and W. Glenn Steels, *Experimentation and Uncertainty Analysis for Engineers*, John Wiley & Sons, 1999.

7. Carne, Thomas G., and Clark R. Dohrmann, Support Conditions, Their Effect of Measure Modal Parameters, *Proceedings of the 16th International Modal Analysis Conference*, pp. 477-483, February 1998.

Intentionally Left Blank

CHAPTER 4. HONEYCOMB CHARACTERIZATION AND MODEL PARAMETER IDENTIFICATION: QUASI-STATIC CRUSH BEHAVIOR

Wei-Yang Lu and Terry Hinnerichs

This chapter will describe the quasi-static experimental procedures, present the test matrices and experimental data, and describe how the test data generated will be used for parameter identification or calibration of the new Honeycomb Crush Model (HCM).

Experimental Setup and Procedure

Uniaxial and biaxial crush experiments were performed on high-density aluminum honeycomb (38 lb/ft^3, Hexcel). Some of the uniaxial tests were performed in a totally confined chamber. These tests are described in Chapter 5.

The remaining uniaxial and biaxial experiments were conducted in the biaxial test rig shown in Figure 4-1a. The system provides in-plane loading in two perpendicular axes, i.e., East-West (EW) and North-South (NS) directions. There are four hydraulic actuators, two per each loading axis, and four control channels, which allow independent control of each actuator. A load cell is bolted to the end of each actuator. A biaxial compression fixture with a capacity of 40 kips is attached to each load cell through two bearing assemblies, which allow the fixture to move with the actuator in the loading direction while accommodating motion perpendicular to the loading direction in the loading plane. A sliding guide mechanism, mounted on each fixture plate, defines and adjusts relative position and motion between adjacent fixtures and enables flexible loading paths. A close-up view of a test setup is shown in Figure 4-1b where the test specimen is highlighted in red.

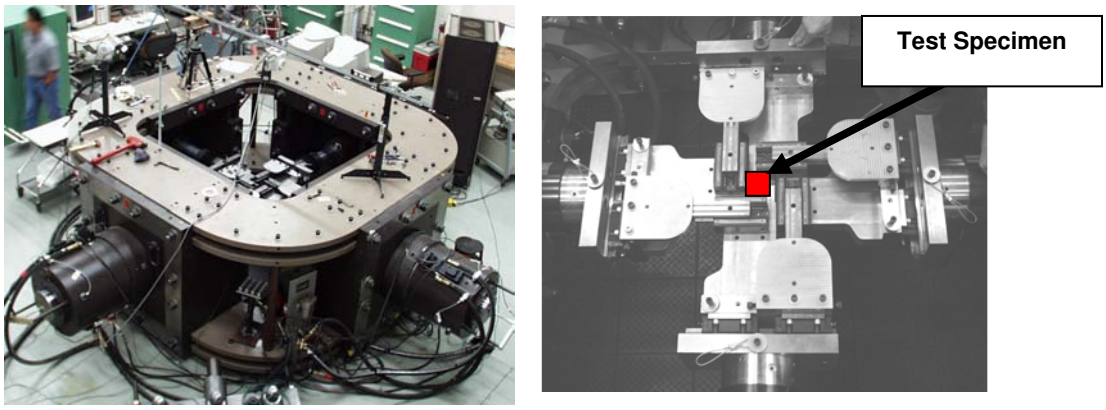

Figure 4-1. (a) In-plane biaxial system and (b) biaxial compression fixture at SNL/CA.

Figure 4-2a shows the system for defining the biaxial test sample configurations. They are designated as XYθ, where X (or Y) represents the principal axis (i.e., T, L, or W) of the honeycomb, the XY plane is parallel to the loading plane, and θ is the angle between the material axis (X or Y) and the loading axis (EW or NS). Figure 4-2b and 4-2c give specific examples of using this convention. In Figure 4-2b, θ is zero for the TL00 configuration, whereas in Figure 4-2c, θ is 45 degrees for the LW45 configuration.

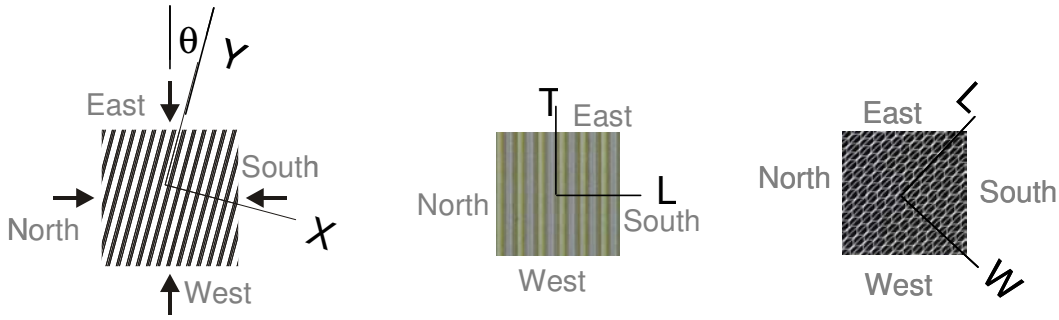

Figure 4-2. Examples of biaxial specimen configurations: (a) definition, (b) TL00, and (c) LW45.

The experimental program involved two types of loading: uniaxial crush and equal biaxial crush. They are illustrated in Figure 4-3. During uniaxial crush on the biaxial system, the East and West actuators move toward each other at a constant speed of 0.5 in. per minute, while the North and South actuators do not move and confine the deformation of honeycomb specimen. Both crush load and confined load were recorded. The remaining two faces that were normal to the loading plane were free. During equal biaxial crush, both EW and NS pairs of actuators moved toward each other at the same rate. All other conditions were similar to the uniaxial crush test.

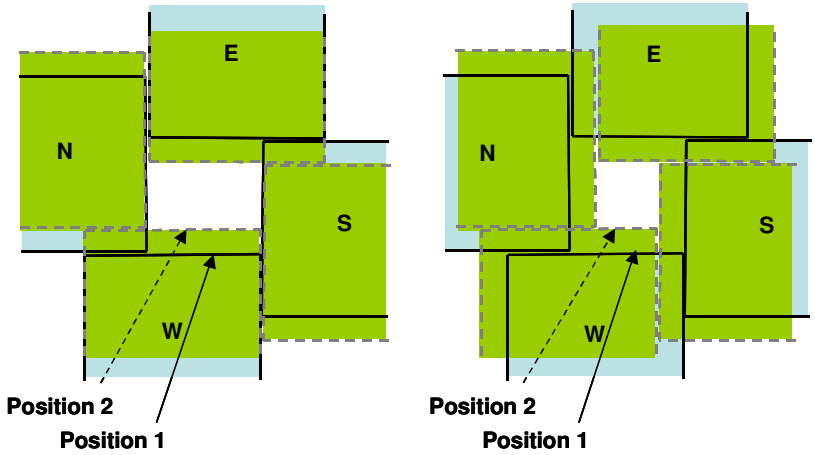

Figure 4-3. Uniaxial crush and equal biaxial crush on the biaxial test rig.

System Characterization and Uncertainty

Before biaxial honeycomb experiments were performed on the system, it was necessary to evaluate friction and cross talk between fixtures to quantify experimental uncertainties. With no specimen in place, each actuator moved in (compressive direction) and out (tensile direction) while the other three actuators were stationary. The displacement-time profile of each actuator was divided into eight segments. As shown in Figure 4-4, the North actuator, for example, was in motion in the first and second segments. It moved in 2 in. in the first segment, then backed out to its initial position at the end of the second segment. In the third to eighth segments, it stayed still. All four loads were monitored during the entire process. A typical waveform of North load cell is displayed in Figure 4-5.

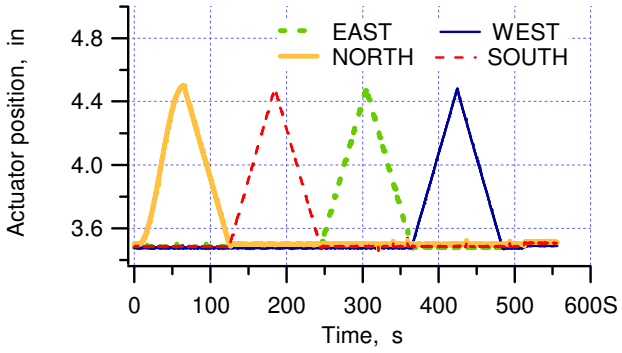

Figure 4-4. Recorded displacement-time history of system performance experiment.

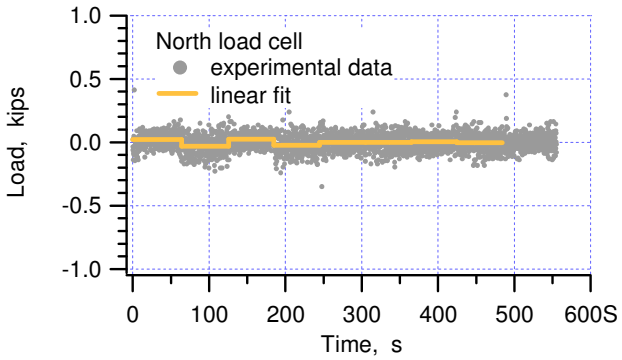

Figure 4-5. North load cell corresponding to motions of actuators without specimen.

Statistical results of all data are listed in Table 4-1. A positive number indicates compressive force. If there was no friction and no cross talk, the averaged load in each segment should be zero. When the North actuator moved in, North and South load cells read 22 and 10 lb, respectively, which was due to friction between fixtures. At the same time, East and West load cells read 2 lb and –7 lb, respectively, which was cross talk or bending due to friction. The results show the maximum friction for all cases is less than 50 lb, and the maximum cross talk between fixtures is less than 10 lb. The uncertainty of load measurement is within 100 lb. In a specimen with a 2-in. × 2-in. cross section, 100 lb corresponds to 25 psi, which is insignificant compared to the 6000 psi crush strength of high-density aluminum honeycomb.

Table 4-1. System characterization results.

#	Loading				Mean, lb				Standard Deviation, lb			
	N	S	E	W	N	S	E	W	N	S	E	W
1	C	–	–	–	22	10	2	-7	53	48	53	50
2	T	–	–	–	-32	-37	-3	3	74	51	67	63
3	–	C	–	–	24	34	-2	1	50	47	58	52
4	–	T	–	–	-22	-37	3	2	74	61	78	70
5	–	–	C	–	-1	0	47	27	63	56	56	66
6	–	–	T	–	-2	-2	-18	-3	70	57	75	68
7	–	–	–	C	3	-6	29	47	59	49	53	59
8	–	–	–	T	-3	1	0	-8	68	57	72	67

Calibration Test Matrix and Data

The complete test matrix is given in Table 4-2 for calibrating the HCM quasi-statically. Three replicas were done for each test condition. As shown in the "Temperature" column of Table 4-2, there will be some tests performed at ambient or room temperature and some at 165 °F. Model parameters will be chosen separately for each temperature since there is no temperature dependence built into the model.

Table 4-2. Calibration test matrix.

Test Rig	Type of Load	Orientation	Temperature	Model Parameter or Function Defined
biaxial system	uniaxial with inplane confinement	TL00	ambient & 165 F	TTP, H_T, TS, b_1
"	"	TW00	ambient	TTP, H_T, TS, c_1
"	"	LW00	"	LLP, H_L, LS, c_2
"	"	TW45	ambient & 165 F	WTWTP, TTWP, TWS
"	"	LW45	ambient	LWLWP, LWS
uniaxial chamber	uniaxial with full confinement	TL45	ambient & 165 F	TLTLP, TTLP, TLS
"	"	WT00	ambient & 165 F	WWP, WS, H_W
biaxial system	equal biaxial with inplane confinement	TL00	ambient	E_{stl}, E_{slt}
"	"	TW00	"	E_{stw}, E_{swt}
"	"	LW00	"	E_{slw}, E_{swl}

The column titled “Model Parameter of Function Defined” lists the various parameters or tabular functions of the HCM that will be defined by the associated test on the same line.

Model Parameter Identification

As described earlier in Chapter 3, the nine elastic orthotropic constants were determined by cell-level computational simulations and experimental modal analyses. A different approach was used for identifying the parameters governing the plastic deformation. Non-homogeneous deformation in the form of a crush-front propagating through the material occurs during the compaction tests on aluminum honeycomb. Consequently, each physical test configuration was modeled and simulated to quantify the model parameters that would minimize the differences between model predictions and test data.

Figure 4-6a shows the finite element model used to simulate the biaxial crush tests. The center square (red) mesh represents the honeycomb sample, and the surrounding rectangular meshed parts represent the platens of the biaxial test rig. A 20 × 20 × 1 mesh is used to model the 2-in. × 2-in. × 1.5-in. honeycomb sample as described above. The platens are modeled as rigid bodies that have contact surfaces with the honeycomb and a coefficient of friction of 0.05 between them and the honeycomb. The platens were lubricated and this friction value was estimated based on the force needed to push a crushed specimen out of the confinement chamber. For computational efficiency using a transient dynamics code, the platens were each given velocity components of 100 in./sec clockwise and inward to simulate the quasi-static biaxial crush experiments. Inertial effects for this PRESTO model are considered negligible at this rate. Contact forces calculated by the PRESTO code between the simulated platens and the honeycomb were collected, divided by the original area, and output for direct comparison with the experimental, engineering crush stresses. Figure 4-6b shows a partially crushed honeycomb model in the TW45 configuration, and the volumetric strain is color coded; red is low strain and blue is high.

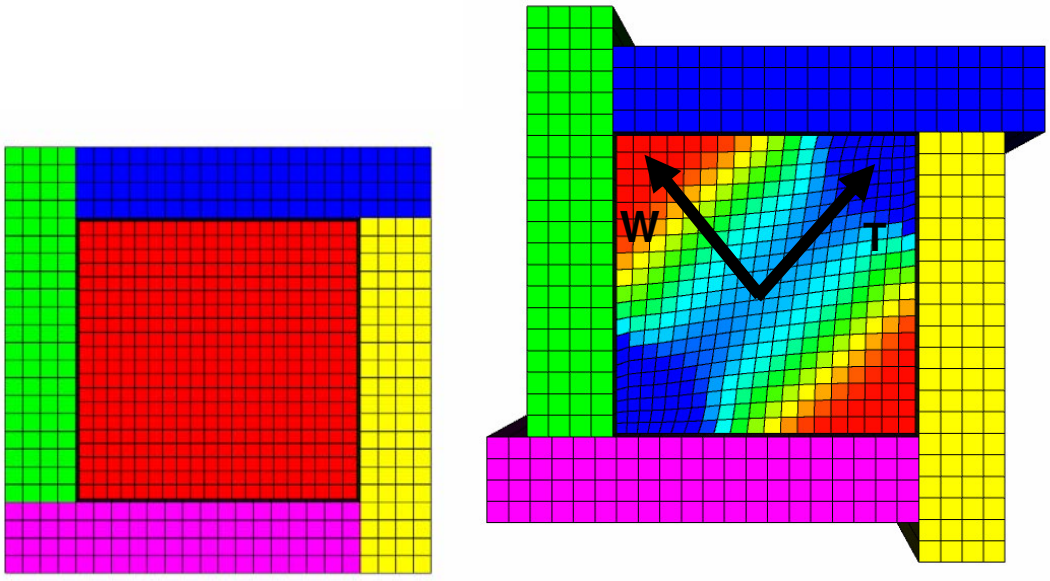

Figure 4-6. Finite element model for equal biaxial crush: (a) undeformed and (b) partially crushed TW45 configuration (volumetric strain is color coded).

Uniaxial Calibration Experiments in the Biaxial Test Rig at Ambient

As mentioned previously, during uniaxial crush on the biaxial system, the East and West actuators move toward each other at a constant speed of 0.5 in. per minute, while the North and South actuators do not move and confine the deformation of the honeycomb specimen. Both crush load and confined load were recorded. The remaining two faces that were normal to the loading plane were free.

Table 4-3 defines the specimen dimensions, mass, and density for each uniaxial test performed in the biaxial test rig at ambient or room temperature.

Table 4-3. Uniaxial experiments on the biaxial test rig for calibration.

Specimen	W(1) (in.)	W(2) (in.)	Height (in.)	Mass (g)	Density (pcf)	Rate (in/s)	σ_{crush} (ksi)
TL00_4*	1.971	1.993	1.525	60.68	38.59	1.67E-02	6.01
TL00_5*	1.951	2.009	1.531	61.09	38.78	1.67E-02	5.46
TL00_6*	1.968	2.014	1.520	61.90	39.14	1.67E-02	6.30
TW00_4	2.025	2.015	1.591	62.04	36.41	1.67E-02	5.54
TW00_5	1.993	1.987	1.542	61.12	38.13	1.67E-02	5.86
TW00_6	2.004	2.020	1.597	60.82	35.84	1.67E-02	6.06
LW00_4	2.022	2.026	1.551	63.77	38.23	1.67E-02	0.93
LW00_6	2.035	2.036	1.542	63.88	38.09	1.67E-02	0.95
LW00_7	2.023	2.042	1.532	62.97	37.91	1.67E-02	0.96
TW45_4	1.855	1.832	1.520	52.49	38.71	1.67E-02	-
TW45_5	1.840	1.880	1.505	50.13	36.68	1.67E-02	-
TW45_6	2.030	2.025	1.530	63.54	38.49	1.67E-02	-
LW45_4	2.000	2.021	1.519	63.42	39.35	1.67E-02	-
LW45_5	1.994	2.052	1.515	63.94	39.29	1.67E-02	-
LW45_6	1.995	2.038	1.516	64.01	39.56	1.67E-02	-
* σ_{crush} for TL00 tests is based on the first 30% strain							

Also, the loading rate and crush stress, σ_{crush}, are given in Table 3. The σ_{crush} value is defined as the average stress for the plateau starting just after the initial peak and ending at the upward hardening slope in the stress strain curve. This value is calculated only for uniaxial tests that are on-axis, e.g., TL00, TW00, or LW00. The σ_{crush} is used to quantify the TS, LS, and WS parameters in the HCM.

Figures 4-7 through 4-13 show the experimental data from the uniaxial tests conducted in the biaxial test rig. The red curves are test data and the blue curves are realizations from the PRESTO/HCM, which will be discussed in the final model validation report to be published next year.

Figure 4-7 shows the test results for the TL00 configuration. Figure 4-7a shows the plot of engineering stress in the loading or T direction versus engineering strain in the loading direction. The oscillations in the data correlate with the formation and collapse of localized buckles in the honeycomb. This phenomenon is a feature of cellular materials [1] and is prevalent in virtually

all of the test data shown in this report. In contrast, the test data have a general fall-off around 30 percent strain due to the expansion of the specimens in the unconfined or out-of-plane W direction as observed during the test. Consequently, the data for this test are considered invalid above 30 percent strain and were not used in the σ crush calculation as indicated in the Table 4-3 footnote.

Similarly, Figure 4-7b shows the engineering stress developed in the confinement or L direction versus strain in the loading direction. Again, the trend in the data changes significantly after 30 percent strain due to the specimen bulging out of plane. Only the data up to 30 percent strain are considered valid. The out-of-plane expansion also tends to delay or increase the strain where lockup begins at approximately 64 percent strain.

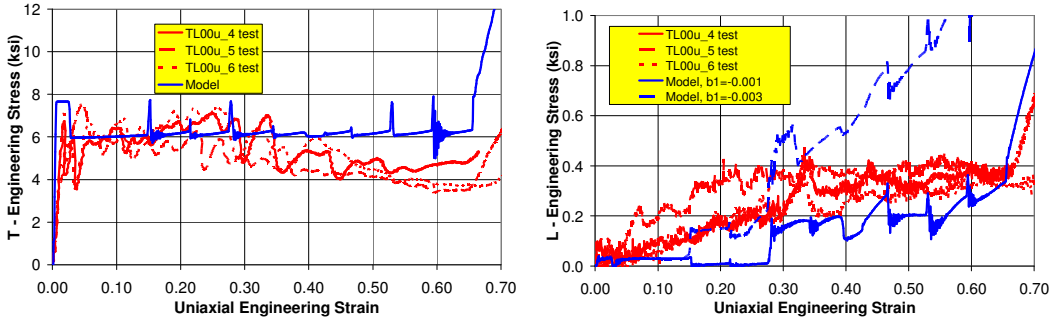

Figure 4-7. TL00 uniaxial test data: (a) T direction and (b) L direction.

Figure 4-8 shows the test results for the TW00 configuration. Figure 4-8a shows the plot of engineering stress in the loading or T direction versus engineering strain in the loading direction. In Figure 4-8b for the TW00 uniaxial test, notice how the stress in the W direction oscillates up to the nominal W crush strength of 0.6 ksi and then falls back to zero out to approximately 25 percent strain. The out-of-plane expansion is not significant for tests like TW00 in Figure 4-8 where the weak W direction is confined.

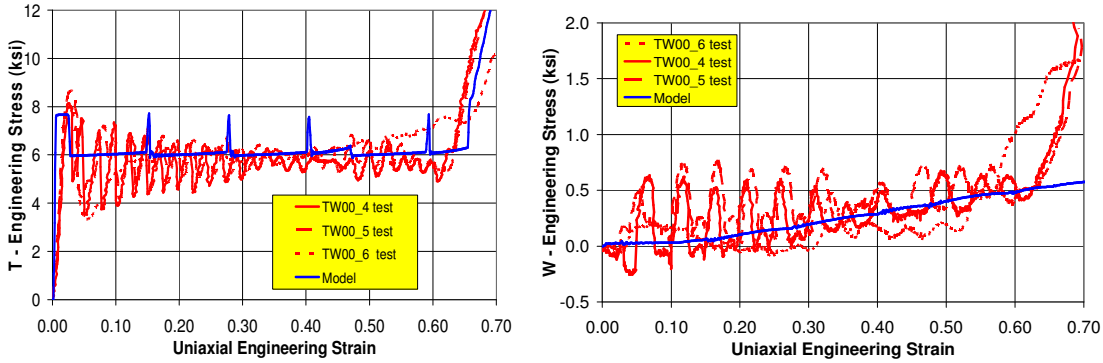

Figure 4-8. TW00 uniaxial test data: (a) T direction and (b) W direction.

Figure 4-9 shows the test results for the LW00 configuration. Figure 4-9a shows the plot of engineering stress in the loading or L direction versus engineering strain in the loading direction. Figure 4-9b shows the stress buildup in the confined direction.

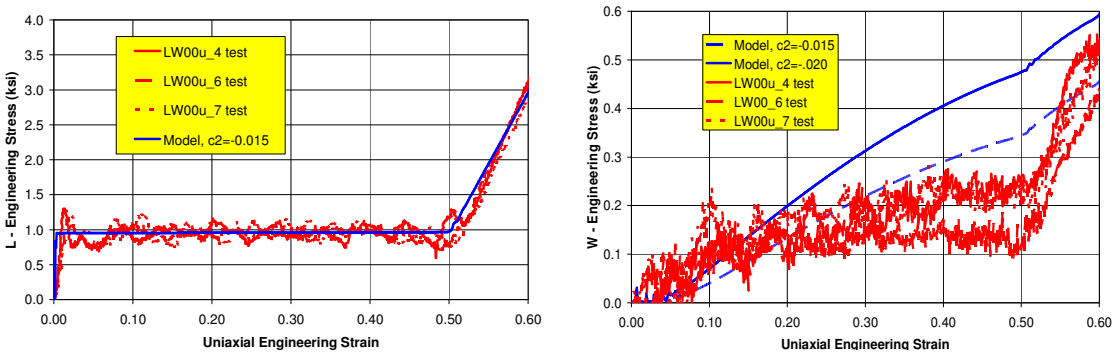

Figure 4-9. LW00 uniaxial test data: (a) L direction and (b) W direction.

Figure 4-10 shows the test results for the TW45 configuration. Figure 4-10a shows the plot of engineering stress in the loading or East direction versus engineering strain in the loading direction. Figure 4-10b shows the stress buildup in the confined or North direction.

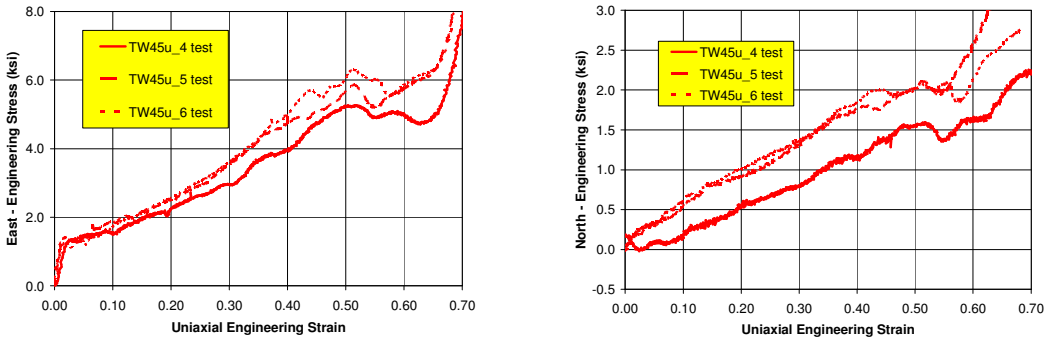

Figure 4-10. TW45 uniaxial test data: (a) loading direction and (b) confinement direction.

Figure 4-11 shows the test results for the LW45 configuration. Figure 4-11a shows the plot of engineering stress in the loading or East direction versus engineering strain in the loading direction. Figure 4-11b shows the stress buildup in the confined or North direction.

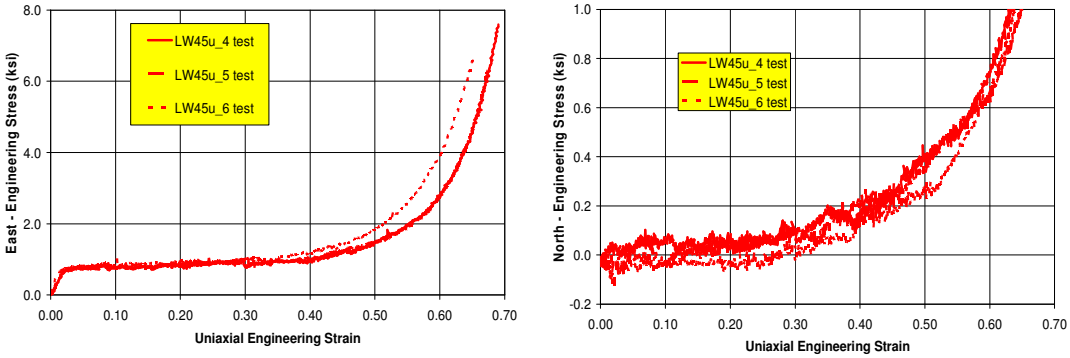

Figure 4-11. LW45 uniaxial test data: (a) loading direction and (b) confinement direction.

Uniaxial Calibration Experiments in the Biaxial Test Rig at 165 °F

Table 4-4 defines the specimen dimensions, mass, and density for each uniaxial test performed in the biaxial test rig at 165 °F. Again, for the on-axis tests, the average crush stress or σ_{crush} has been calculated from the results.

Table 4-4. Uniaxial experiments on the biaxial test rig for calibration at 165 °F.

Specimen		W(1)	W(2)	Height	Mass	Density	Temp.	σ_{crush}
Type	#	(in.)	(in.)	(in.)	(g)	(pcf)	(°F)	(ksi)
TW45	7	1.820	1.815	1.504	50.82	38.97	165	
TW45	8	2.055	2.005	1.522	63.34	38.48	165	
TW45	9	2.000	2.068	1.518	64.1	38.89	165	
TL00	7	1.973	1.990	1.513	60.62	38.87	165	5.65
TL00	8	1.988	1.988	1.507	60.58	38.75	165	5.76
TL00	9	1.971	1.997	1.517	61.2	39.05	165	5.85

Tests on the TL00 configuration were repeated at 165 °F; test data are shown in Figure 4-12. Figure 4-12a shows the engineering stress in the loading or T direction versus strain in the loading direction, and Figure 4-12b shows the stress buildup in the confined direction. These data will be used to quantify the influence of temperature on the crush strength. The average value of σ_{crush} at 165 °F is about 2.9% lower than at ambient based on this data.

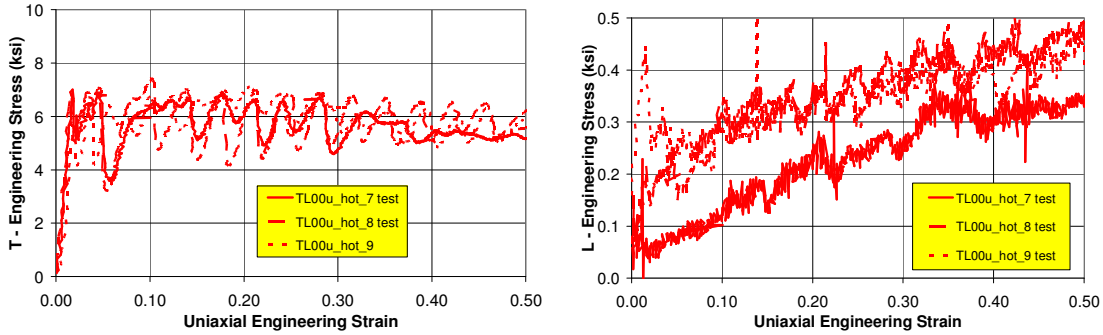

Figure 4-12. TL00 uniaxial test data at 165°F: (a) T direction and (b) L direction.

Tests on the TL45 configuration were repeated at 165 °F; test data are shown in Figure 4-13. Figure 4-13a shows the engineering stress in the loading or East direction versus strain in the loading direction and Figure 4-12b shows the stress buildup in the confined or North direction. These data will be used to quantify the influence of temperature on the off-axis crush strength.

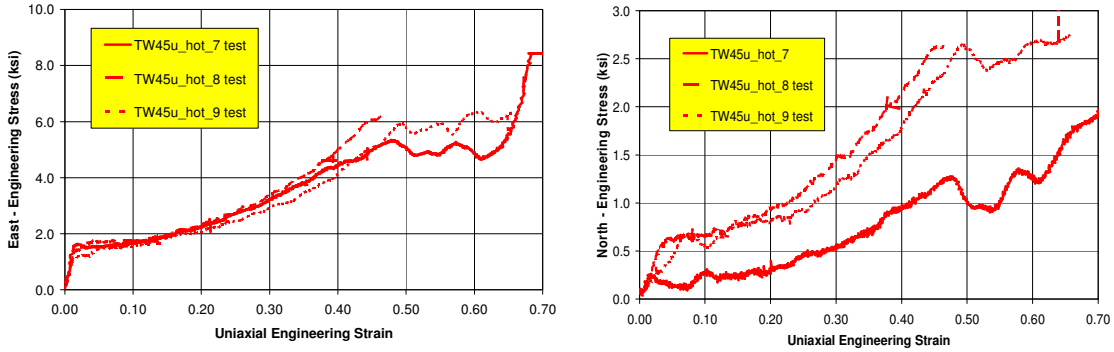

Figure 4-13. Plots of TW45 uniaxial test data at 165 °F: (a) loading direction and (b) confinement direction.

Uniaxial Calibration Experiments in the Confinement Chamber

During uniaxial crush in the confinement chamber only one actuator is loading the specimen in the axial direction at 0.0167 or 16.7 ft/sec. Only the crush load is measured in the axial direction. The remaining two faces that were normal to the loading plane are confined by the chamber walls.

Tables 4-5 and 4-6 define the specimen dimensions, mass, and density for each uniaxial test performed in the confinement chamber. The crush efficiency column is an estimate of where the curve departs from an approximate constant value plateau for the crush stress and begins the hardening phase to lockup. The tests in Table 4-5 are the only ones in this chapter performed at 16.7 ft/sec. All other tests in Table 4-6 were performed at quasi-static rates of .0167 ft/sec. The tests in Table 4-5 are all WT00 tests, which measure the weakest direction of the honeycomb and are judged to be good representations of quasi-static behavior since little rate effects have been observed in this material direction compared to the T direction.

Table 4-5. Uniaxial W direction crush experiments in the confinement chamber with crush velocity of 16.7 ft/sec.

Specimen	d_1, in	d_2, in	d_3, in	Weight, lb	Density, pcf	Crush Velocity, ft/sec	Crush Efficiency, %	Crush Strength, ksi (fit)
H38W01	1.201	1.195	1.514	0.0488	38.83	16.55	38.15	0.602
H38W02	1.189	1.191	1.520	0.0482	38.71	16.58	39.16	0.615
H38W03	1.192	1.190	1.513	0.0480	38.64	16.57	39.44	0.600
H38W04	1.194	1.191	1.512	0.0475	38.20	16.69	35.34	0.623
H38W05	1.191	1.191	1.510	0.0480	38.72	16.65	34.97	0.617
H38W06	1.194	1.192	1.514	0.0486	39.00	16.69	34.87	0.584
H38W07	1.191	1.195	1.506	0.0485	39.07	16.74	37.40	0.621
H38W08	1.201	1.191	1.520	0.0492	39.09	16.67	39.68	0.584
H38W09	1.195	1.195	1.515	0.0484	38.67	16.76	37.18	0.577
H38W10	1.191	1.195	1.507	0.0477	38.45	16.75	36.95	0.608
H38W11	1.195	1.194	1.509	0.0483	38.73	16.77	37.54	0.585
H38W12	1.196	1.194	1.505	0.0478	38.43	16.79	33.91	0.584
H38W13	1.194	1.195	1.509	0.0485	38.91	16.86	37.01	0.607
H38W14	1.200	1.193	1.514	0.0486	38.76	16.83	36.88	0.596
H38W15	1.193	1.195	1.505	0.0476	38.30	16.84	37.00	0.590
				Max	39.09	16.86	39.68	0.623
				Min	38.20	16.55	33.91	0.577
				Average	38.70	16.72	37.03	0.599
				Std deviation	0.27	0.10	1.70	0.015
				Median	38.72	16.74	37.01	0.600

Figure 4-14 shows the results for the uniaxial tests of the WT00 configuration loaded at the rates given in Table 4-5. This test provides an estimate for the WS parameter in the HCM.

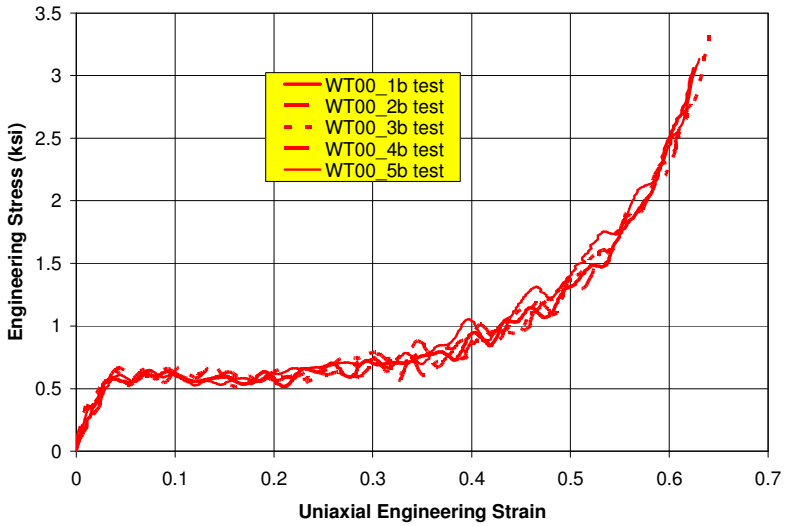

Figure 4-14. Plot of WT00 tests at ambient in confinement chamber.

Table 4-6 defines the specimen dimensions, mass, and density for each uniaxial test performed in the confinement chamber at quasi-static rates of .0167 ft/sec.

Table 4-6. Uniaxial off-axis crush experiments in the confinement chamber for calibration.

Specimen		W(1)	W(2)	Height	Mass	Density	Temp.	Rate
Type	#	(in.)	(in.)	(in.)	(g)	(pcf)	(°F)	(in./sec)
TL45	1	1.188	1.218	1.750	25.44	38.27	70	0.0167
TL45	2	1.212	1.211	1.751	25.92	38.42	70	0.0167
TL45	3	1.207	1.205	1.755	25.36	37.85	70	0.0167
TL45	4	1.202	1.214	1.754	25.35	37.73	165	0.0167
TL45	5	1.206	1.216	1.751	25.26	37.47	165	0.0167
TL45	6	1.198	1.203	1.755	25.69	38.69	165	0.0167

Figure 4-15 shows results for the uniaxial crush tests of the TL45 configuration. Figure 4-15a gives the results for ambient temperature, and Figure 4-15b for 165 °F. The difference between ambient and 165 °F data looks like only a few percent or even within the uncertainty of the data.

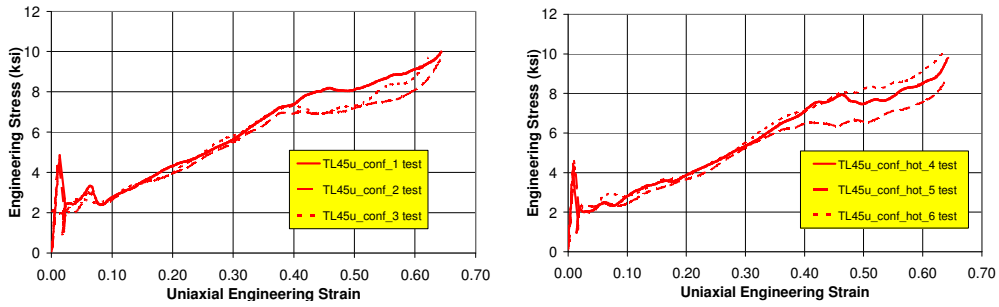

Figure 4-15. TL45 biaxial crush experiment data: (a) ambient and (b) 165 °F.

Equal Biaxial Experiments

In these tests, as mentioned earlier, both EW and NS pairs of actuators in the biaxial rig move toward each other loading the specimen in two orthogonal directions. The out-of-plane direction is traction free.

Table 4-7 lists the dimensions, mass, and density along with the testing rate for each specimen tested with equal biaxial loading.

Table 4-7. Equal biaxial crush experiments for calibration at ambient.

Specimen	W(1) (in.)	W(2) (in.)	Height (in.)	Mass (g)	Density (pcf)	Rate (in./sec)
TL00_1	1.835	1.825	1.504	51.37	38.85	1.67E-02
TL00_2	1.980	2.008	1.503	60.86	38.80	1.67E-02
TL00_3	2.005	2.013	1.522	63.61	39.45	1.67E-02
TW00_1	2.010	2.013	1.496	60.78	38.25	1.67E-02
TW00_2	2.020	1.989	1.515	60.30	37.74	1.67E-02
TW00_3	2.022	1.986	1.582	64.19	38.49	1.67E-02
LW00_1	2.071	2.018	1.527	63.41	37.85	1.67E-02
LW00_2	2.020	2.050	1.491	62.00	38.25	1.67E-02
LW00_3	2.058	2.020	1.476	61.37	38.10	1.67E-02

Figure 4-16 shows results for the TL00 equal biaxial crush test. Figure 4-16a gives the results for the T direction, and Figure 4-16b for the L direction.

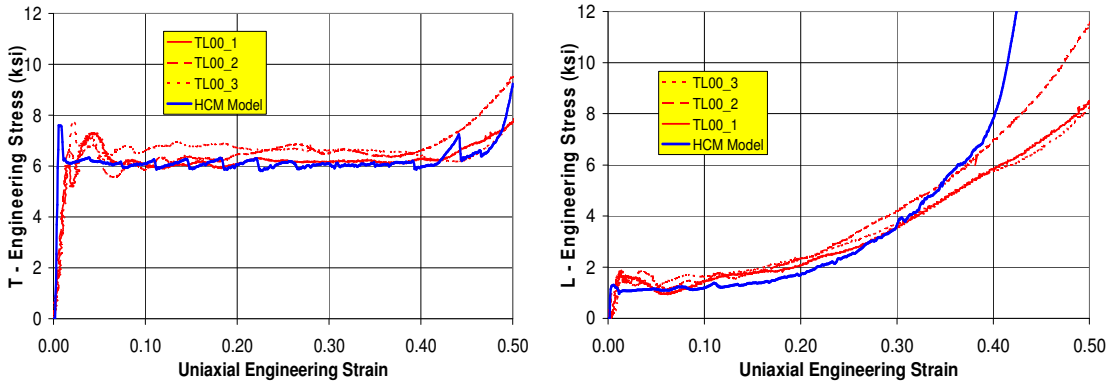

Figure 4-16. TL00 equal biaxial crush test data at ambient: (a) T direction and (b) L direction.

Figure 4-17 shows the results for the TW00 equal biaxial crush test results. Figure 4-17a gives the results in the T direction, and Figure 4-17b in the W direction.

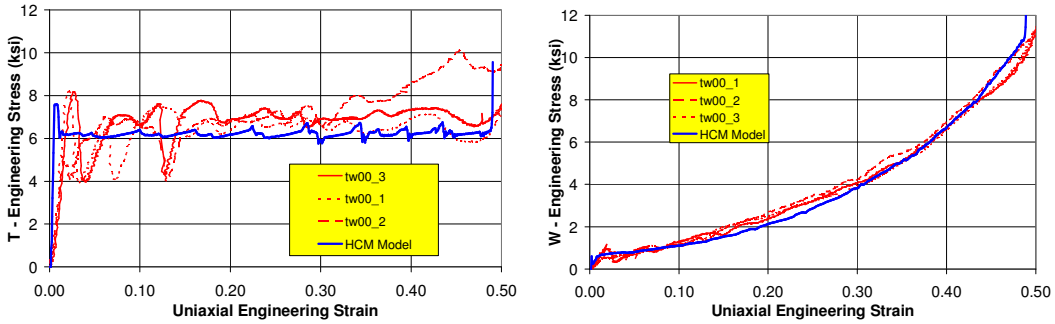

Figure 4-17. TW00 equal biaxial crush test data at ambient: (a) T direction and (b) W direction.

Figure 4-18 shows the results for the LW00 equal biaxial tests, which combine the two weakest directions. Figure 4-18a gives the results for the L direction, and Figure 4-18b for the W direction.

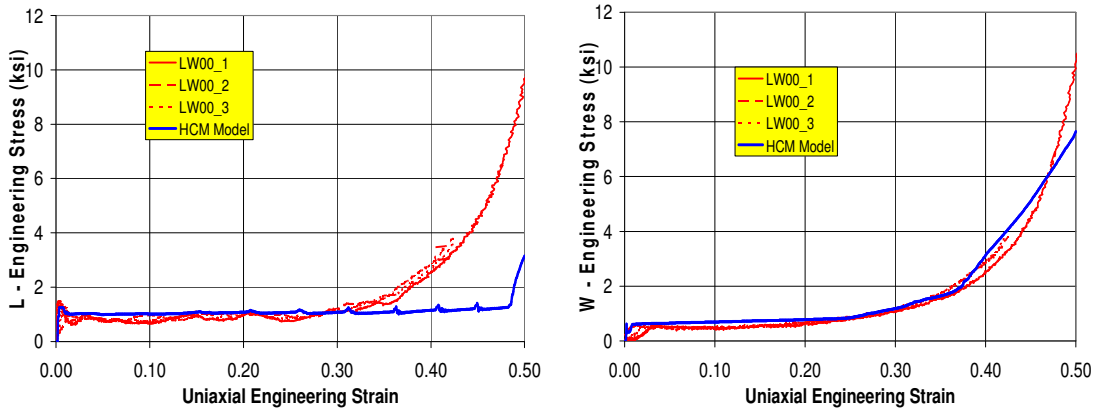

Figure 4-18. LW00 equal biaxial crush test data at ambient: (a) L direction and (b) W direction.

References

1. Gibson, L.J., and M.F. Ashby, *Cellular Solids: Structure and Properties, 2nd Edition*, Cambridge University Press, New York, NY, 1997.

CHAPTER 5. HONEYCOMB CHARACTERIZATION: STRAIN RATE EFFECTS

Thomas G. Carne and Wei-Yang Lu

Introduction

In this chapter, the measurement of the dynamic crush strength of honeycomb will be examined. The characterization of honeycomb for the quasi-static crush behavior has been discussed in Chapter 4 and the orthotropic linear-elastic (small strains) characterization in Chapter 3. When honeycomb material is used for energy absorption, it is most frequently in a dynamic crush environment. Because of the plastic hinges that are formed in the thin sheets of aluminum during crushing, incredibly high strain rates are experienced by the aluminum, as much as 10,000/sec strain rates. Bitzer in [1] shows that honeycomb materials do develop higher crush strengths during dynamic crushing with dynamic enhancements as high as 20 to 30 percent. These higher crush strengths are due in part to higher plastic yield stress arising at these large strain rates. Consequently, we need to characterize the dynamic crush behavior because it is certainly different from the quasi-static behavior, and the dynamic enhancement would be most important for designing energy absorption. For the constitutive model for the honeycomb, one would require that the dynamic crush strength be a function of the crush rate.

For this honeycomb application, we were interested in crush rates ranging from quasi-static to as high as 1800 in./sec. In order to obtain an adequate assessment of this difficult-to-measure quantity and to cover most of the range of the crush rate, three different experimental techniques were developed for the low and intermediate rates within this desired range. The three approaches were able to cover most of the range of crush rates except for the higher rates, and three approaches provided redundant data, thus increasing the confidence across the measured range of crush rates. Ideally, it would have been desirable to measure the crush strength at the highest crush rate, 1800 in./sec, but limitations in instrumentation and facilities excluded the highest rates.

The first technique was designed for the low crush rates, from quasi-static up to 160 in./sec; the honeycomb was crushed at a constant rate using a high-speed material test machine. This approach provided very high-quality measurements at low crush rates. The honeycomb was inserted into a test fixture, consisting of a cylinder for lateral confinement and a piston for applying the load to the honeycomb. The confinement chamber was connected to the hydraulic actuator through a shear-pin. The applied force was measured with a load cell connected to the piston, which was attached to the loading frame.

To measure the crush strength at the intermediate rates (0 to 600 in./sec), a transient dynamic test was designed. This test did have a disadvantage, however, of being a transient test, so the crush velocity varied during the test. Consequently, the crush force had to be related to the instantaneous crush rate. This second approach did produce results down to quasi-static rates, overlapping the range covered by the first approach. The results from the two techniques compared well, providing confidence in both approaches. The test fixture was similar to that used for the low rate testing, consisting of a cylinder and a piston. However, in this fixture the

load cell or force transducer was incorporated into the fixture, directly beneath the honeycomb, so that it sensed the force applied to the honeycomb. To create the transient crush force, the entire test fixture, consisting of the cylinder, piston, honeycomb sample, and integral force transducer, was mounted on the carriage of a standard drop table and accelerated to a speed of approximately 600 in./sec before impacting an inertial mass.

The third approach also measured the crush for the intermediate crush rates and utilized the Horizontal Actuator at Sandia's Area III as the test facility so that the high-impact speeds could be obtained. For this test, no constraining fixture was included with the honeycomb sample in order to reduce the test complications and the mass involved. Instead, a cylindrical section of honeycomb was radially confined by wrapping the cylinder with fiber-reinforced tape. This technique for confinement had been previously evaluated and shown to produce equivalent results to those of the cylinder-piston confining fixture [2]. This test, as with the above described second experimental technique, was a transient test with crush velocity varying thorough the test. These three different techniques and the resulting measured data will be described more fully in the following sections.

Figure 5-1 below shows a photograph of the high-density (38 lb/ft^3) aluminum honeycomb used in this study. In contrast to other honeycomb characterization measurements, all of the testing described here used samples from a single large manufactured block of honeycomb, thus eliminating the block-to-block variability. The aluminum plates are relatively thick (0.006 in.) and the honeycomb includes a flat plate between each row of corrugated plate, making the honeycomb higher density and higher strength. Note that there are three principal directions in the honeycomb, T, L, and W, with the T direction being the strongest and the W direction being the weakest. The strengths are significantly different, varying by more than a factor of ten. This feature can produce advantages in design, where one direction is much softer than another, but also creates a structure that is somewhat unstable. This instability can cause the honeycomb to buckle globally with significantly decreased energy absorption. Figure 5-2 shows a cross section of a honeycomb sample that has been crushed with numerous localized buckles, absorbing a great deal of energy. Ordinarily, honeycomb material is laterally confined both in design and material testing so that it deforms into the tight buckle configuration revealed in Figure 5-2. The crush rate testing discussed in this chapter is only for crushes in the T direction. The T direction is the most important for energy absorption, so the effort was concentrated for that direction.

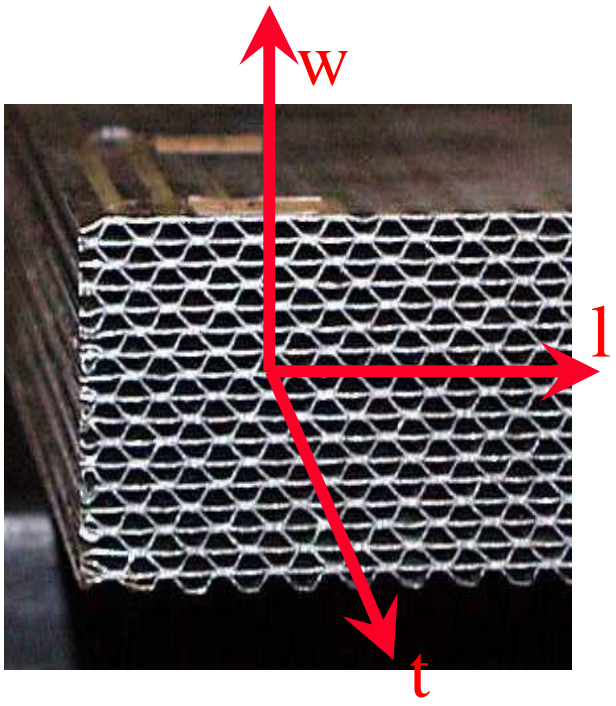

Figure 5-1. High-density aluminum honeycomb, showing the three principal directions.

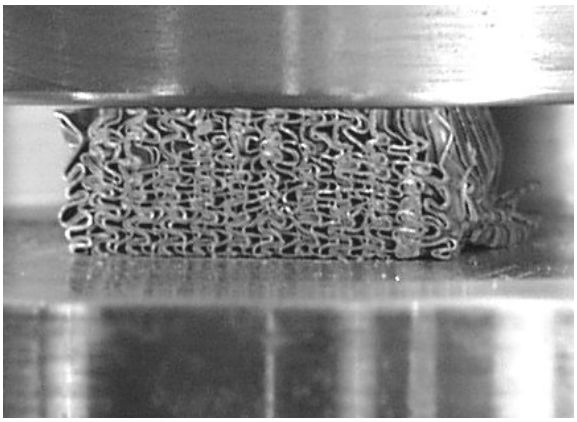

Figure 5-2. Sample of crushed honeycomb material with tight energy-absorbing plastic buckles.

Quasi-Static Testing to Measure the Crush Strength

Before attempting to measure the dynamic crush strength of the honeycomb, quasi-static testing was performed [3]. This testing produced an approximate zero crush rate yield stress that provided the basis for designing the dynamic tests. As mentioned earlier, there are very large differences in the crush strengths of the honeycomb in the three principal directions that can lead to unstable deformations when the honeycomb is loaded in the strongest direction; consequently some type of lateral confinement is usually required during material testing. To provide the lateral confinement for the honeycomb while crushing it in the strong T direction, a piston and cylinder test fixture was designed; the square cross-section cylinder would confine the honeycomb while the piston would exert the crushing force. During quasi-static testing, both the displacement of the honeycomb and the applied force were measured. Figure 5-3 shows the test fixture used for the quasi-static testing [3]. The photo on the left shows an opened cylinder, exposing the piston and the honeycomb sample, while the photo on the right reveals the closed cylinder, ready for testing. The honeycomb samples were 1.2 in. square by 1.5 in. tall. There was concern regarding the internal friction that might be generated as the honeycomb was crushed and expanded into the wall of cylinder. However, from independent measurements of the friction, we were able to determine that the existing friction force was small compared to the applied force [4], because the surface was lubricated. The coefficient of friction was measured to be 0.05 during a push-out test of a crushed honeycomb slug from the confinement chamber.

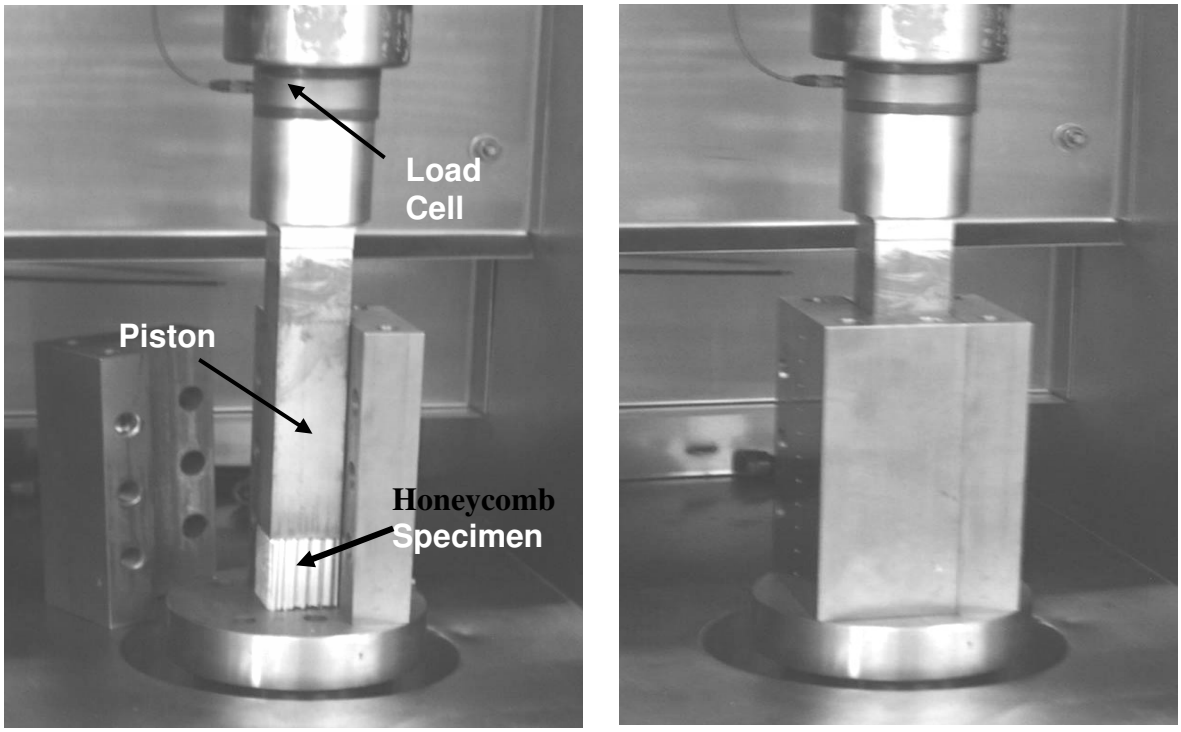

Figure 5-3. Test fixture for the quasi-static testing of the honeycomb, showing the piston and square cross-section cylinder.

The data in Figure 5-4 are representative of honeycomb quasi-static test results. The plot shows the applied stress (ksi) as a function of the strain (in./in.), and illustrates some interesting features. Examining Specimen T_01, for example, initially the stress increases very rapidly with deformation due to the elastic response of the honeycomb. Then at about 7000 psi (0.02 in./in.), the material plastically buckles with a rapid reduction in stress and an increase in deformation. The stress then increases again, then decreases due to another plastic buckle, and continues in this pattern a number of times until the material settles into a fairly constant stress state. At larger strains, the stress increases rapidly as the honeycomb approaches lock-up, the point at which the material density of the honeycomb approaches that of solid aluminum.

From a modeling standpoint, it is advantageous to approximate the honeycomb as an elastic-plastic material with a plateau yield stress, until the deformation approaches the lock-up condition. Except for the buckling behavior shown in Figure 5-4, this would appear to be a fairly good representation of the material behavior. However, in all the test data, the buckling of the individual cell layers and the resulting oscillations in the stress is very evident during crushing, making it difficult to extract the plateau yield stress. These stress oscillations tend to damp-out during quasi-static testing into a fairly constant stress level, but during the dynamic crushing of the honeycomb the oscillations persist during the entire crush event. This is observable in Figure 5-5 in which the strain rate was held at 0.75 in./in. For higher strain rates, the oscillations are larger and more persistent.

A typical material testing system allows precise closed-loop control up to 1 in./sec. Figure 5-5 shows the test results at 0.75 in./sec. In those tests, the loading was stopped before reaching lock-up. To obtain higher crush rates from a material test system, special procedures must be developed utilizing a shear pin; these will be discussed in the next section.

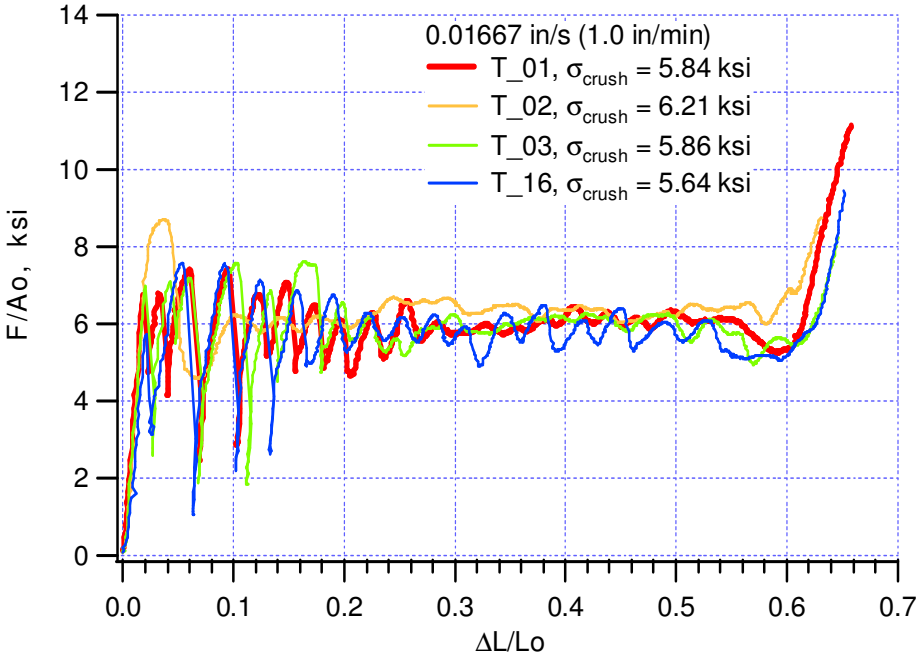

Figure 5-4. Representative test results from quasi-static testing, revealing plastic buckles and the plateau stress.

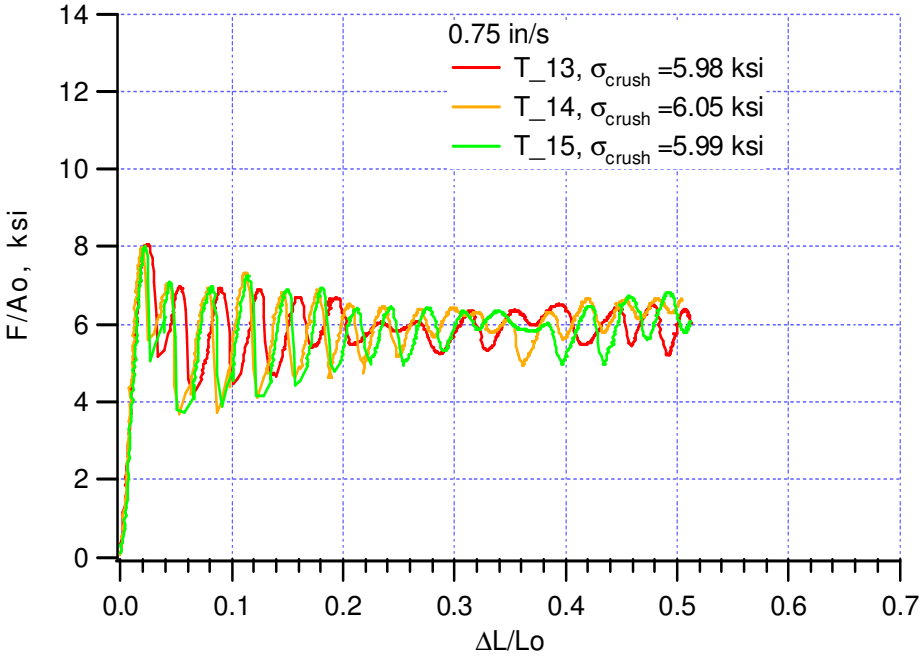

Figure 5-5. Test results of crushing honeycomb at 0.75 in./sec.

Measurement of the Dynamic Crush Strength

In this section, we will discuss each of the three test techniques separately along with their crush strength results, including the test apparatus, instrumentation, and signal processing for each of the three techniques. In the last section, the results from the three techniques will be consolidated into a single format, revealing the entire range of crush rates.

First Technique: Low Crush Rates Using an MTS Material Test Machine

When conducting the test at a rate greater than 1 in./sec, the MTS High Rate System was switched to open-loop control in order to obtain the very high velocities required. In order to protect the load cell and fixtures in the loading train, a shear-pin break-off mechanism was incorporated in the actuator, which releases the load when it exceeds the strength of the shear pin. Figure 5-6 shows a typical plot of the load and displacement data for testing at 160 in./sec. The dashed displacement curve shows that the period from -10 to -3 ms was the accelerating period, while the period from 10 to 19 ms was the braking period. The red load curve indicates the engagement of loading rod and specimen began at about 3.0 ms, where the displacement was about 3.5 in. The velocity remained nearly constant at 160 in./sec and decreased slightly during lock-up, where the load increased quickly. When the load reached approximately 23 kips, or at 11 ms, the shear pin broke and the load dropped to zero immediately. The actuator continued to move, but it was disengaged from the confined chamber and no longer loading the specimen.

In addition to the quasi-static tests, Figures 5-4 and 5-5, tests were performed at two different dynamic crush rates, approximately 17 in./sec and 160 in./sec. The results are plotted in Figures 5-7 and 5-8. The normalized load-displacement results for the testing at 160 in./sec have similar crush and densification features as those of lower rates, but at 160 in./sec the results display significant high-frequency content or stress oscillations. These oscillations may be due to the ringing in the loading system or more evidence of the honeycomb buckling that we have observed in slower crush testing. Since this high-frequency content does not affect the calculation of average crush strength or energy absorption rate, they have not been filtered out from the signal.

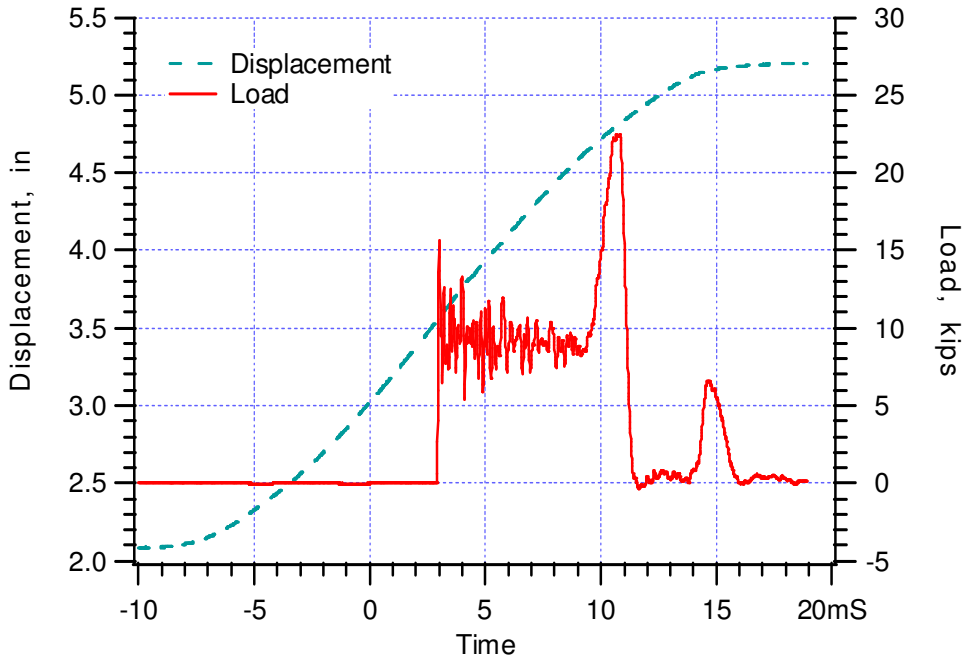

Figure 5-6. Typical load and displacement time data of intermediate rate, 15 ft/sec, compression of high-density aluminum honeycomb, Specimen T_04.

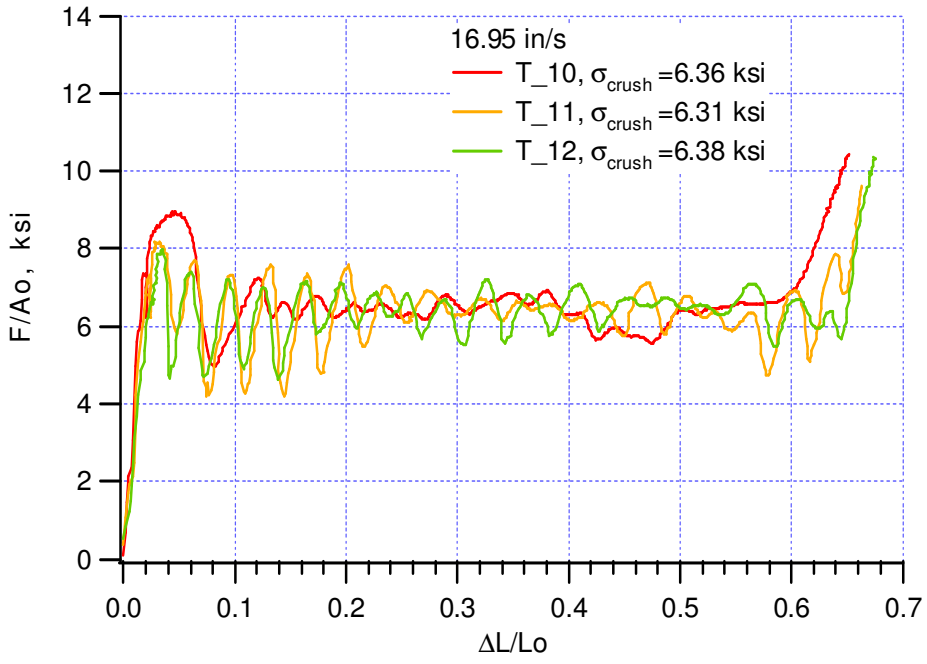

Figure 5-7. Test results of crushing honeycomb at approximately 17 in./sec.

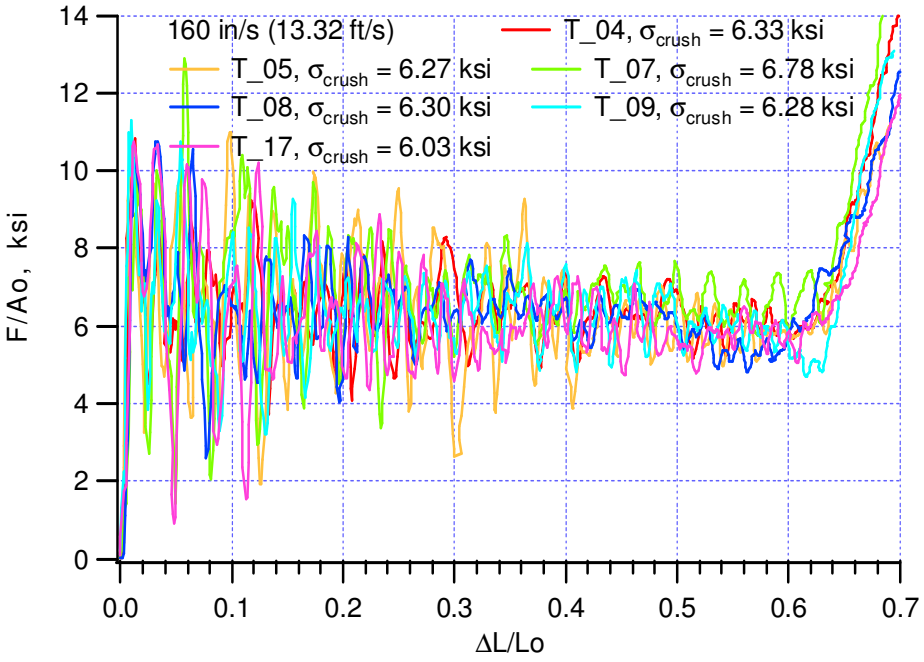

Figure 5-8. Test results of crushing honeycomb at approximately 160 in./sec.

Second Technique: Intermediate Crush Rates Using a Drop Table

In order to induce higher dynamic crush velocities or strain rates on the honeycomb, a transient dynamic test was designed, along with an adapted test fixture. This test was designed to crush the honeycomb much faster than was possible using a typical MTS load frame. However, it did have the disadvantage of being a transient test, in which the crush velocity varies during the test. Consequently, the crush force must be related to the instantaneous crush rate. The dynamic test fixture was very similar in concept to that used for the quasi-static testing except for two modifications. A force transducer with a load-bearing plate was added at the bottom of the confining cylinder beneath the honeycomb. Using this integral force transducer, the crush force could be measured directly, rather than using a force transducer external to the fixture. The other modification to the test fixture was a substantial increase in the mass (42 lb) of the loading piston, which would provide the inertial crush force to the honeycomb, as seen in Figure 5-9. In addition, four uni-axial accelerometers were attached to both the piston and the cylinder so that their accelerations, as well as the crush force, would be measured during the test. Velocities and displacements of the piston and cylinder were obtained by integrating the accelerometer signals.

To apply the transient crush force, the entire test fixture (the cylinder, piston, honeycomb sample, and integral force transducer) was mounted on the carriage of a drop table, and accelerated to an approximate velocity of 50 ft/sec. Both gravity and bungee cords were used to accelerate the carriage downward. The carriage would then impact a large stationary inertial mass, causing the carriage and test fixture to rapidly decelerate and rebound. The duration of the impact event was controlled with the impact speed and load profiling materials placed between the carriage and the large inertial mass. Typically the duration of the impact was 4 msec. Figure

5-9 shows two photographs of the dynamic test fixture, with the honeycomb loaded in the cylinder. In the close-up photo, one of the four sides of the square cross-sectional cylinder has been removed to expose the honeycomb sample. The photo on the left includes a sample of crushed honeycomb. The honeycomb samples used for all the transient tests were 2-in. cubes of the Hexcel 38 lb/ft^3.

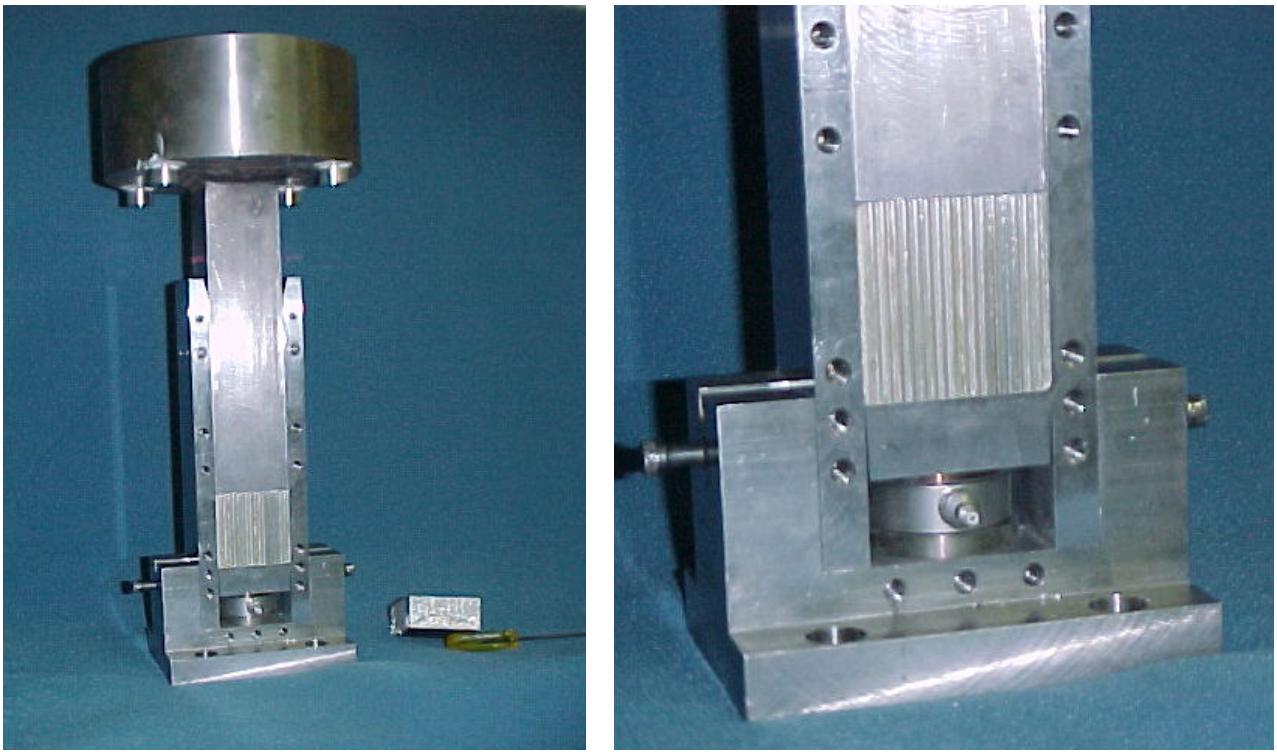

Figure 5-9. Fixture for dynamically crushing the honeycomb, and measuring both force and accelerations.

One feature of the test fixture needs to be particularly emphasized. This feature, if ignored, can significantly affect the validity of the measured force. Located above the force transducer, as shown in Figure 5-9, is a load spreader plate. This plate does not move relative to the cylinder because the force transducer is very stiff. However, the plate does experience the same deceleration as the cylinder during a test event. Consequently, the integral force transducer measures both the crush force applied to the honeycomb and the additional inertial force required to decelerate the load spreader plate. Ignoring this inertial force will invalidate the force measurement. In addition to the mass of the spreader plate, portions of the mass of both the force transducer and honeycomb sample were included with the load spreader plate to calculate the added inertial force experienced by the force transducer, but their masses were small when compared to the load spreader.

The crush force was obtained two different ways, providing redundant measurements of this most important quantity. The first method used the force transducer located at the bottom of the cylinder. This transducer provided a direct measurement of the crush force. The second method used the accelerometers located on the piston, which provided the piston's inertial force bearing

on the honeycomb. This second independent force measurement method added confidence to the directly measured crush force. However, because of friction between the crushed honeycomb and the cylinder, the piston inertial force was actually the sum of the frictional force and the honeycomb crush force. The measured inertial force should always be equal to or greater than the directly measured force due to the additional friction force. Subtracting the directly measured force from the inertial measured force produces an estimate of the frictional force. However, because both the accelerometers and the force transducer had uncertainties associated with their sensitivities and the friction force was small relative to the crush force, this computed friction force had a large uncertainty relative to its magnitude.

The true friction force will be zero at the very beginning of the crush event because the honeycomb has not yet expanded to bear against the walls of the cylinder. However, for most of the tests the calculated friction force was actually negative at the beginning of the crush and increased during the crush to a positive value. This calculated negative friction is completely due to the inaccuracies in the transducer sensitivities. Typically, at the beginning of the crush, the friction force was minus 6 percent of the directly measured force; at the end of the crush, the friction force was typically a positive 3 percent of the directly measured force. This shows that the friction increased during the crush event as more and more honeycomb material was compressed against the sides of the cylinder. The uncertainty in the accelerometer sensitivities was 8 percent and that of the force transducer was 3 percent, so one would expect that the difference between the two force measurements would have an uncertainty equal to 9 percent of the force measurement. Consequently, one cannot expect to be able to measure the small friction force with any certainty, although the trend of increasing friction force was repeated in all the tested samples. The friction force definitely increased during the crush event and had a peak (maximum-minimum) value of approximately 9 percent of the crush force at the end of the crush.

Measurement of the Dynamic Crush Stress

As mentioned previously, crushing the honeycomb specimen required attaching the test fixture onto the carriage of a drop table and then accelerating the carriage and test fixture downward toward the inertial mass. Typical impact speeds were 50 ft/sec. Actual impact velocities were measured independently, using a beam cutting velocity transducer. The force and eight acceleration channels (four located on the piston, four located on the cylinder) were recorded and digitized at 50,000 samples/sec. The resulting signals were subsequently digitally filtered at 4 kHz. Figure 5-10 shows a typical result, obtained from Test Sample #3. The entire crush event occurs in approximately 4 msec, with measured peak stresses of about 8 kpsi. The initial honeycomb buckles are again evident in the test data. The figure also shows some residual stress occurring after the event. This is due to the honeycomb compressing the load cell and being held in place by the friction against the cylinder wall. Fortunately, the honeycomb always initiated the crush at the top of the sample, and then propagated the tight buckle pattern downwards toward the load cell. This was observed numerous times in partially crushed samples and also with high-speed photography. The friction force does resist the piston, but the integral force transducer senses only the force on the bottom of the sample and the inertial force of the load spreader, which does not include the friction force.

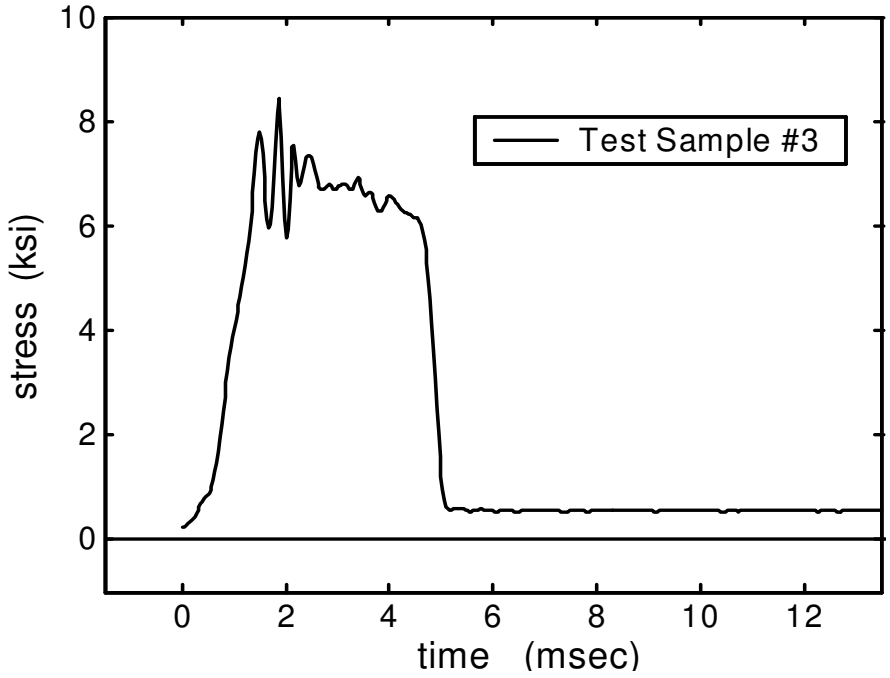

Figure 5-10. Measured stress on a typical honeycomb sample as a function of time during a dynamic crush test.

The motion of the cylinder and piston can be obtained by integrating the acceleration measurements twice, producing displacements as a function of time. In the integration process, there are two constants of integration that are established by setting the initial displacements (first contact with the inertial mass) of the cylinder and piston equal to zero and their initial velocities equal to the measured impact velocity. Zero time ($t = 0$) in the analysis is defined at first impact.

Figure 5-11 shows the transient behavior of this dynamic crush event for one of the ten test samples. Positive displacement is upwards, so the initial velocity (the slope of the displacement function) is negative, as shown in the plot. Examining the figure, one can see that initial impact occurs at zero time. Once this impact occurs, the carriage decelerates rapidly and reverses direction at approximately 2 msec. The piston bears upon and crushes the honeycomb as the piston is decelerated by the reaction of the crush force. The piston then eventually reverses directions at about 3.5 msec. The crush distance is just the difference between the carriage and the piston displacements, and is shown in the figure reaching its peak value at about 4.5 msec.

As mentioned above, the displacements were obtained by integrating the accelerometer signals. Because the crush distance is the difference of the carriage and piston displacements, a large uncertainty in the results could exist because of the uncertainties in the sensitivities of the accelerometers. However, these computed maximum crush distances were compared with physical measurements of the crushed honeycomb. For the ten crushed samples, the computed values were within 5 percent of the physical measurements. This small percentage lends credibility to the signal processing used for the experimental crush velocities and crush distances.

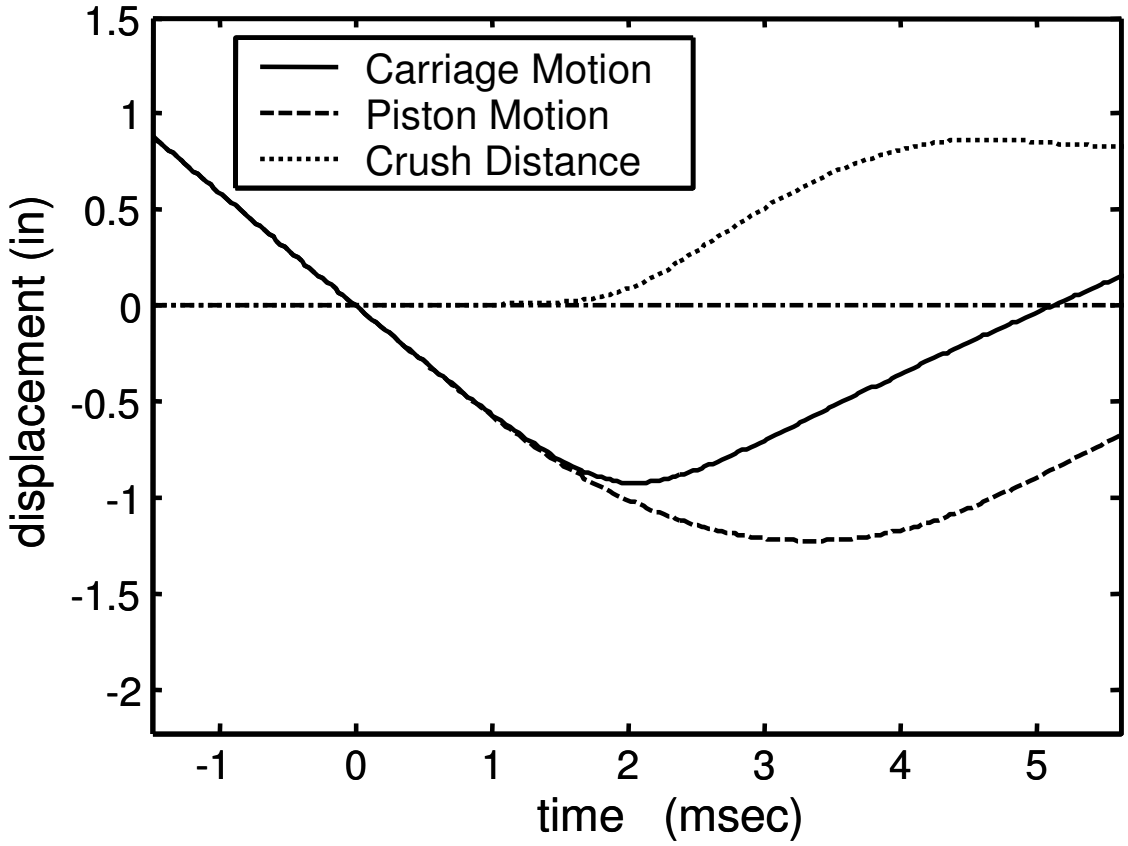

Figure 5-11. Carriage and piston motion and crush distance as a function of time during a typical crush test.

Knowing the crush distance, the crush velocity, and the crush stress as a function of time allows one to examine the experimental data in a number of different ways. For example, one can parametrically plot the crush stress versus the crush distance, using time as the parameter. Figure 5-12 shows an example of these data. Here again, one can see the initial buckles that occur in the early deformation of the honeycomb. The honeycomb does not develop a plateau stress until approximately 0.35 in. of crush. In order to determine the plateau crush stress of the honeycomb, these initial plastic buckles have not been included in the calculations performed for each of the ten samples. The stress data that occur after these initial buckles was used in the data analysis for computing the plateau crush stress and for computing the crush stress as a function of crush velocity.

The crush velocity can also be plotted versus the crush distance, as shown in Figure 5-13. As can be inferred from Figure 5-11, the crush velocity is actually zero at the beginning of the event. Upon impact, the crush velocity increases to a maximum, then decreases back to zero as the carriage and the piston eventually attain the same speed, thereby ending the crush. Also shown in Figure 5-13 is the range of data used for computing the variation of the crush stress with the crush velocity. Unfortunately, a significant portion of the data cannot be used due to the erratic stress resulting from the buckling behavior of the honeycomb.

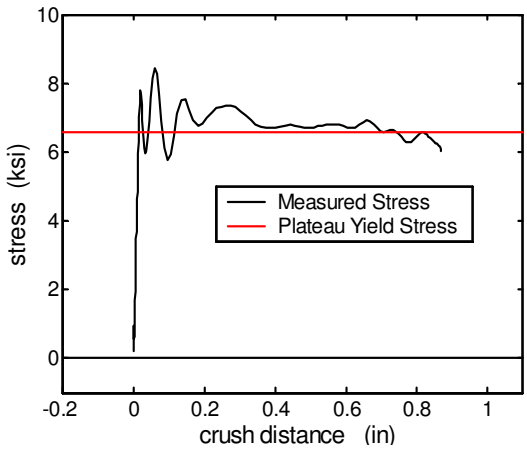

Figure 5-12. Crush stress versus crush distance.

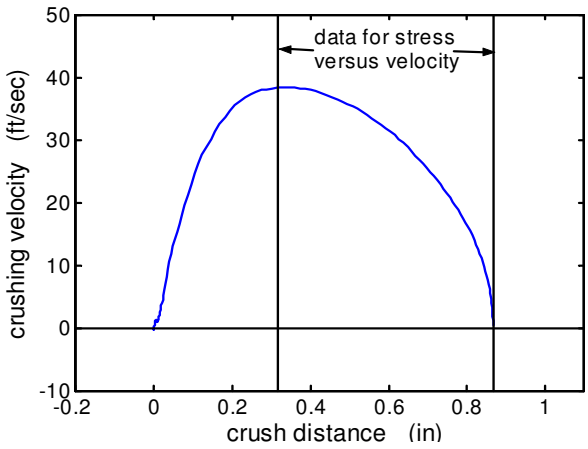

Figure 5-13. Crush velocity versus crush distance.

Because we know both the honeycomb stress and the crush velocity as a function of time, we can parametrically plot the stress versus the crush velocity. Because of the constantly changing velocity and the crush stress, the data are plotted as a series of points in Figure 5-14 for one of the honeycomb test samples. Each of the data points represents an instant in time where both the stress and the velocity have been measured. One can observe oscillations in the stress even though the presented data were measured after the major buckling occurred. These oscillations make a direct observation of the functional relationship between crush stress and crush velocity very difficult. However, it is quite clear from the figure that the crush stress as a general trend tends to increase with crush velocity.

For each of ten samples of honeycomb, similar data were measured as shown in Figures 5-11 through 5-14. Because there is variation in the honeycomb material for each of the samples, and some variation in the specifics of each test, including the impact speed, the data from the ten samples do show some scatter. Also, the buckling behavior of the honeycomb further enhances the observed scatter. The variations in crush stress versus crush velocity for the ten samples are shown in Figure 5-15 with dots indicating each set of measured data. Truncating the vertical axis has highlighted the apparent magnitude of the scatter, which is approximately plus or minus 6.5 percent about the mean. Even with this scatter, the trend of yield stress increasing with crush velocity is very apparent.

One last issue regarding the crush velocity needs to be discussed. Usually in the formulation of a constitutive model, one would want yield stress as a function of the strain rate, not the crush velocity. For the presented experiments, it was appropriate to report the crush or yield stress as a function of the crush velocity because the crush velocity was measured directly. However, measuring the local strain rate was very difficult. The average strain rate for the whole sample could be obtained by just dividing the crush velocity by the length of the sample, but that average would not be relevant because one would have different strain rates depending on the size of the sample for the same crush velocity.

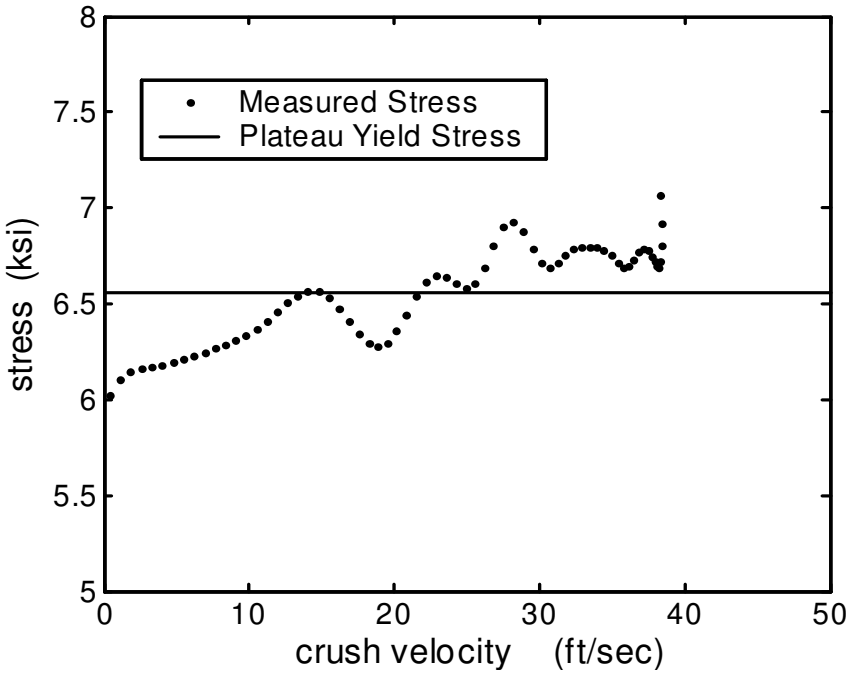

Figure 5-14. Crush stress versus the crush velocity for Sample #3, measured at series of instances in time.

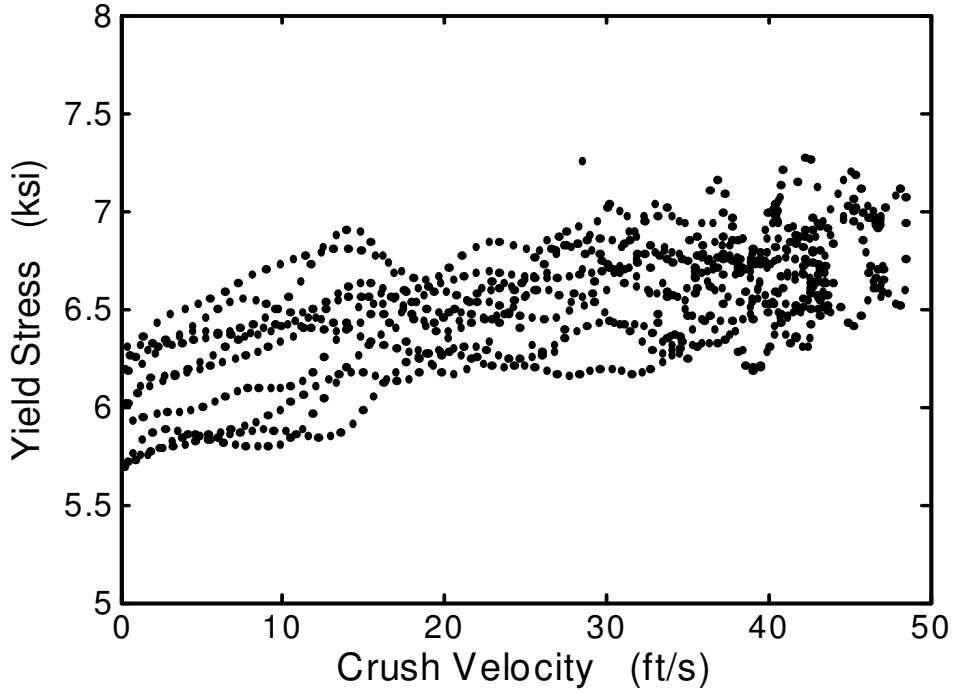

Figure 5-15. Yield stress versus crush velocity for all ten honeycomb samples.

We are attempting to treat the honeycomb as a homogeneous material, even though it does tend to crush one layer at a time. This crush pattern was observed during the quasi-static testing and from the use of high-speed photography during the dynamic crush testing. For this particular honeycomb, the undeformed layers are 0.125 in. thick. These layers experience strains of 0.65 in./in. during their initial crush, which has been observed and measured in previous experiments. Consequently, the local strain rate in a honeycomb layer being crushed is the crush velocity (in./sec) divided by the layer thickness. The honeycomb material strain rate in a honeycomb layer, $\dot{\varepsilon}$, can be calculated from

$$\dot{\varepsilon} = 96. * V_{crush}$$

where V_{crush} is measure in ft/sec, and the strain rate is in./in./sec. For example, for a crush velocity of 40.0 ft/sec, the local strain rate in a layer is approximately 40*12*(1 / 0.125) = 3840.0/sec. This is engineering strain, that is, change in length divided by undeformed length.

Third Technique: Intermediate Crush Rates Using the Sandia Horizontal Actuator

In order to induce higher dynamic crush velocities or strain rates on the honeycomb, another transient dynamic test was designed, using the 12-in. Horizontal Actuator in Area III. This testing was included as part of large series of Tier 2 validation testing using the actuator, discussed in Chapter 7. The test was designed to crush the honeycomb much faster than was possible using an MTS load frame or the dynamic technique using the drop table. However, because of limitations in the instrumentation system and constraints on the size of the impacting mass, only intermediate crush rates were obtained during this test sequence. Higher rates could have been obtained, but that would have required a different test design than that used for the Tier 2 validation testing. However, this additional intermediate crush rate data did provide supplementary data, which supported our earlier measurements and increased the confidence in the results. Like the second test technique, this procedure did have the disadvantage of being a transient test, in which the crush velocity varied during the test. Consequently, the crush force must be related to the instantaneous crush rate.

The actuator used for this material test is pictured in Figure 5-16. The pneumatic piston, when fired, propels the instrumented sled down the rails, where it impacts and crushes the honeycomb sample. The sample was mounted onto a force-transducer fixture that was connected to a large seismic mass (~ 8000 lb). The force transducer measures the applied force directly. As with the second technique, the measured force includes a component due to the inertial acceleration of the mounting fixture, and that was accounted for in the calculation for the crush force. Both the impact mass and the seismic mass were instrumented with four accelerometers each to record their accelerations, and the impact mass included a vertical accelerometer to measure any resulting acceleration normal the sled motion. Figure 5-17 shows a diagram of the complete test apparatus with the actuator, impact sled, honeycomb sample, and seismic mass. The force transducer, composed of four individual transducers sandwiched between two plates, is mounted between the honeycomb sample and the seismic mass as shown in Figure 5-18 with a honeycomb structure that was used for the validation testing.

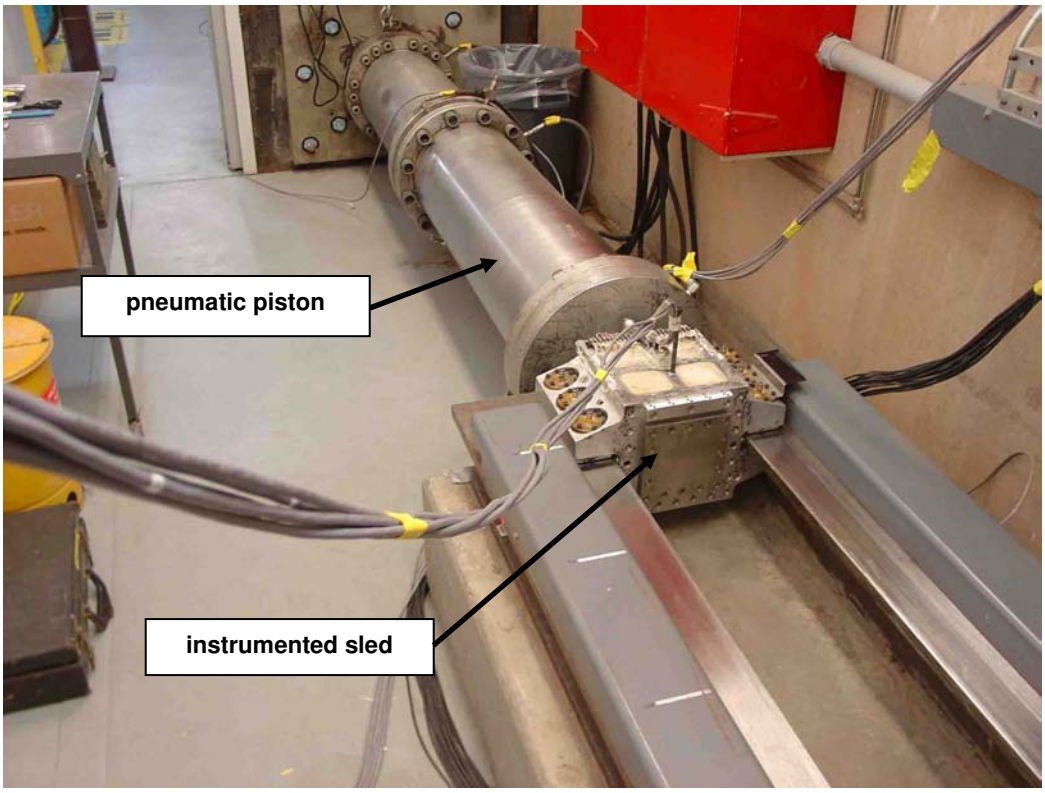

Figure 5-16. Pneumatic piston with instrumented sled.

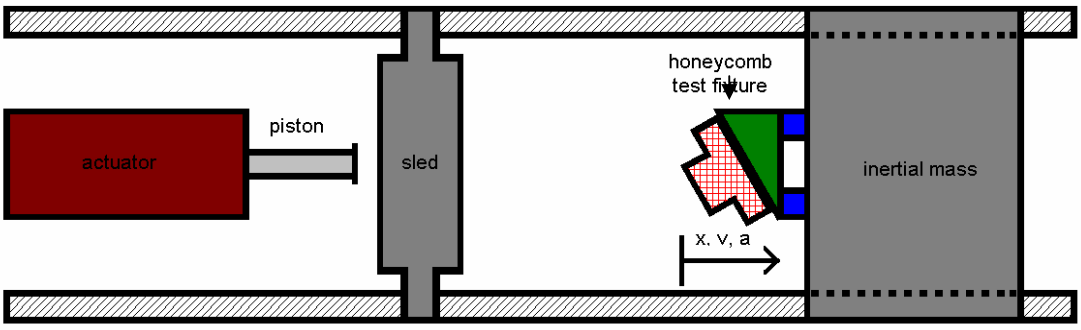

Figure 5-17. Diagram of experimental configuration for testing honeycomb samples on horizontal actuator.

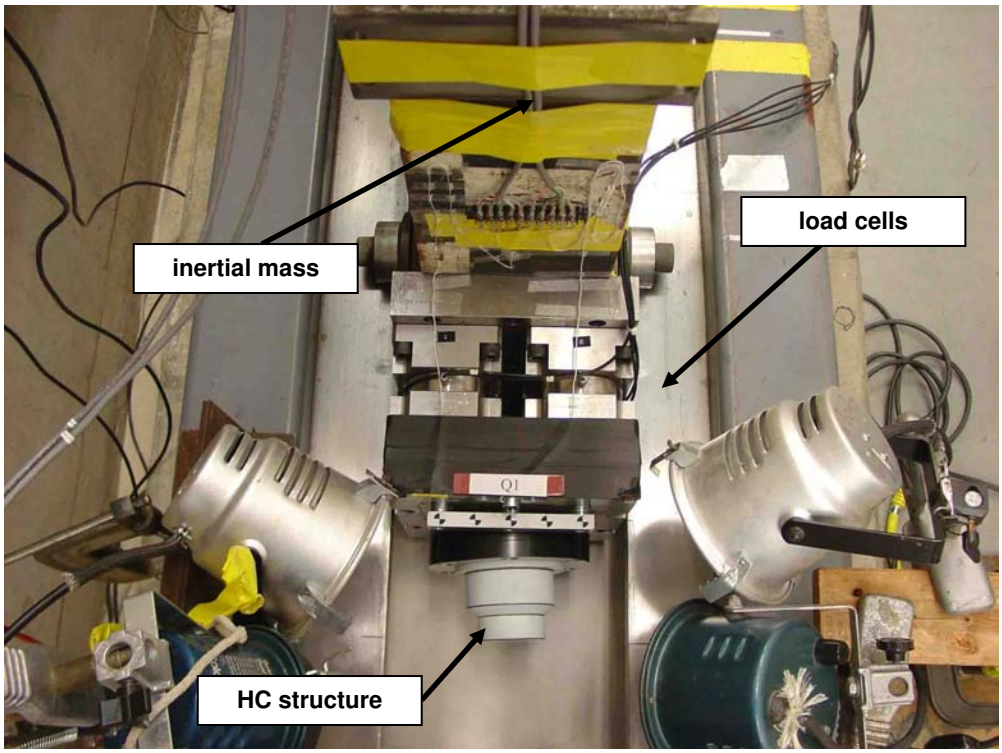

Figure 5-18. Inertial mass with assembled honeycomb test structure.

Four honeycomb samples were crushed for this test sequence; however, the first two samples overloaded the force transducer because of the very high peak dynamic forces, and those results had to be discarded. Testing with reduced impact speed and consequently reduced crush rate on the last two samples did not overload the force transducer and good measurements were taken. The two good samples are designated V4 and V5. They were cylindrical in shape, 4 in. in diameter by 2 in. thick, with the honeycomb T direction axial. They were machined from the same large honeycomb block as all samples used in this report. The constraint was provided by using four and a half wraps of 2-in.-wide fiber-reinforced tape around the circumference of the sample. This tape provides very effective radial constraint, but offers no resistance to the axial crush of the honeycomb. This confinement technique was evaluated and compared to the hard cylindrical confinement previously used for honeycomb testing in [2]. Reference [2] shows that the tape confinement produces the same results as hard cylinder confinement within the uncertainty of the measured crush stress.

As observed in the other dynamic crush tests of honeycomb, the crush stress had very large dynamic oscillations due to the buckling of the honeycomb. See Figures 5-8 and 5-10. These stress oscillations are particularly apparent in the measured data from these tests, as seen in Figure 5-19. The amplitude of the oscillations are about the same as that observed in the high strain rate testing on the MTS machines (Figure 5-8), but the period of oscillation is much longer for these tests. The fixture was thoroughly tested to ascertain if the observed frequency was due to any fixture dynamics, but the fixture frequencies were much higher than that observed. Consequently, it is believed that the oscillation are due to the dynamic plastic buckling of the

honeycomb, as we have observed in other test environments. Figure 5-19 shows the measured crush stress as a function of time for the Sample V4. Also plotted in this figure is the crush velocity, multiplied by a factor of 10, and the crush displacement, multiplied by a factor of 10,000. The initial impact speed was 801 in./sec, and the peak stress was approximately 11,000 psi.

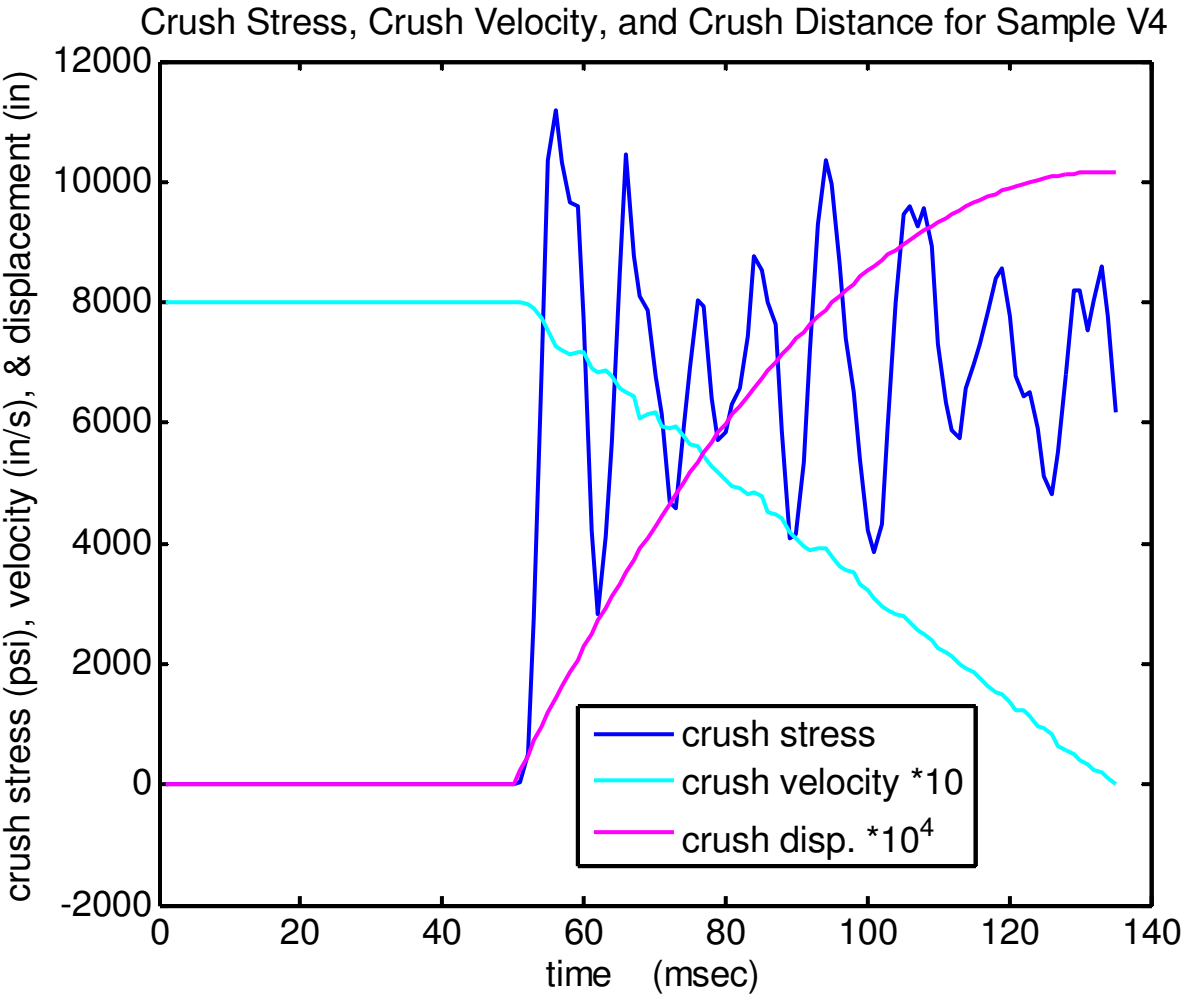

Figure 5-19. Measured data for honeycomb Sample V4, plotted versus time.

Figure 5-20 shows the corresponding measured data for Sample V5 with an initial impact speed of 877 in./sec and peak stress of 12,200 psi; both of these quantities are higher than for V4. The initial peak stress definitely increased with impact speed, which caused the overloading for the first two samples tested. The data measure for the two samples, V4 and V5, appears somewhat similar except the stress appears to diminish for Sample V5 at the higher crush displacements. Sample V5 did experience a larger total crush and was approaching lock-up at the end of the test. The stress reduction is probably due to the normal dip in stress that has been observed previously just before lock-up, and it exists for strains between 0.5 and 0.6 for Sample V5.

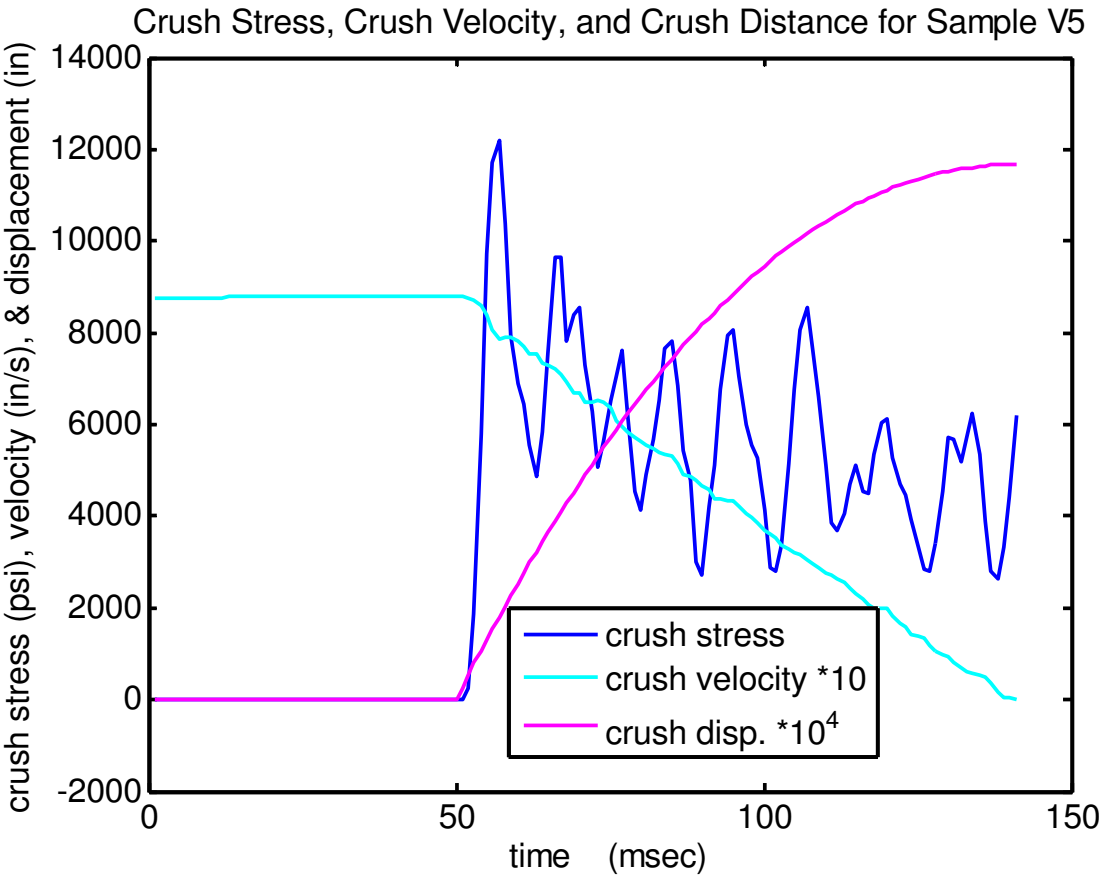

Figure 5-20. Measured data for honeycomb Sample V5, plotted versus time.

Figures 5-19 and 5-20 plot the measured data as a function of time, but the data can also be parametrically plotted as a function of the crush velocity using time as the parameter. Figures 5-21 and 5-22 show the crush stress for V4 and V5 plotted as a function of the crush velocity. In these figures the range of velocities used for the plots has been reduced, eliminating the first stress peak, as has been our practice for computing crush stress, and all the stresses for strains over 0.5, to avoid the stress dip just before lock-up. The two figures are qualitatively very similar with large stress oscillations with a fairly low frequency. Unfortunately, these large oscillations completely obscure any trend that the crush stress has with crush velocity, as had been observed from the data for Techniques One and Two. Consequently, because no significant trend can really be observed from this data, the value of these measurements is significantly reduced, except they do reveal a crush stress during a high strain rate event. The average crush stress can be computed along with the average crush velocity for these tests, and these averages are listed with the figures. On the figures, the quantity labeled mean velocity is the mean crush velocity for the data displayed in the figures. Clearly, these averages are very much the middle points for two widely varying quantities. Sample V5 does exhibit a higher average crush rate, but a lower average crush stress. The mean crush stress for V4 was 7129 psi and that for V5 was 6109 psi. The data from all three techniques will be compared and summarized in the final section of this chapter.

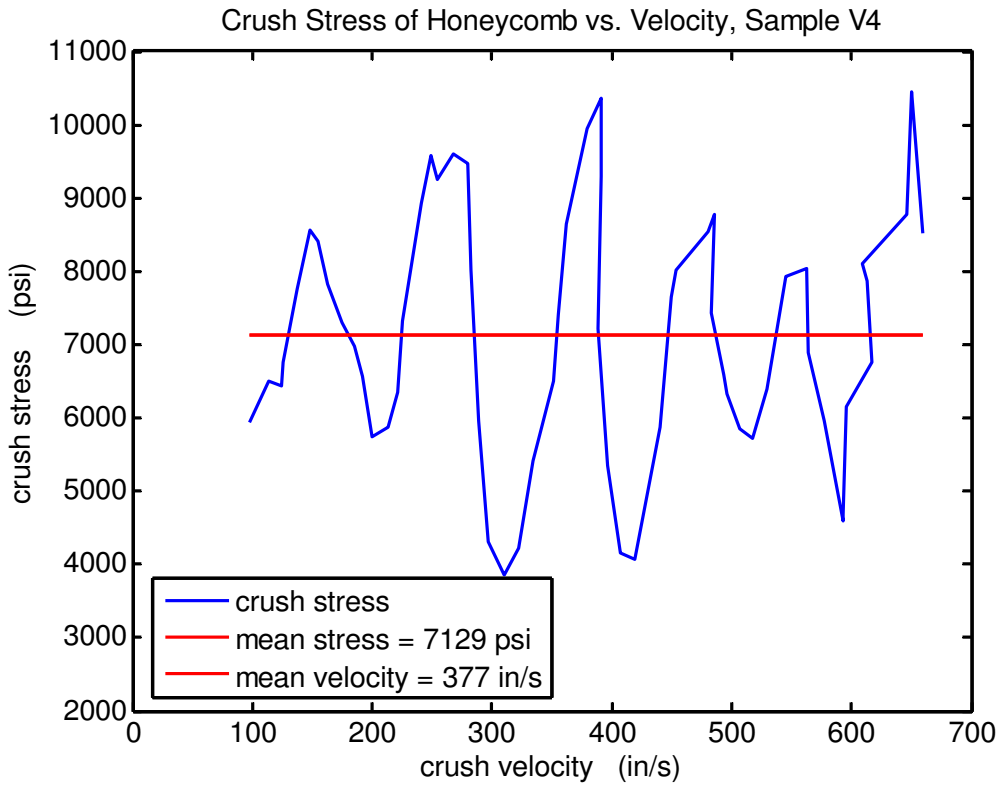

Figure 5-21. Measured crush stress for honeycomb Sample V4, plotted versus crush velocity.

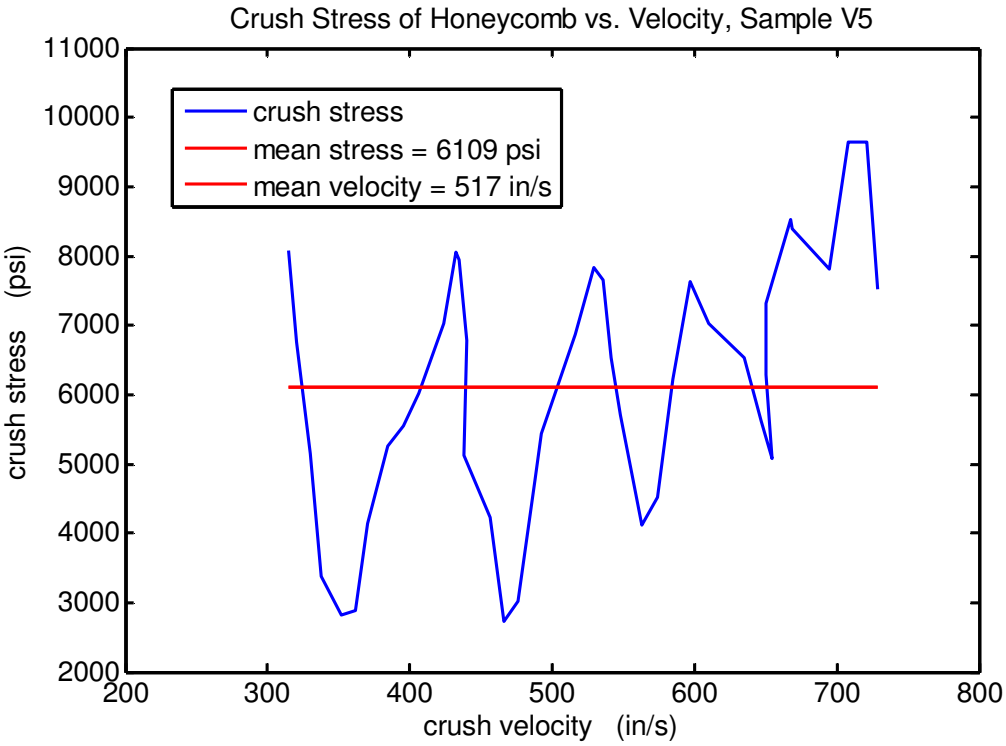

Figure 5-22. Measured crush stress for honeycomb Sample V5, plotted versus crush velocity.

Summary and Consolidation of Crush Stress Results from the Three Techniques

In this section the results for the three techniques will be consolidated and compared in order to reveal the underlying behavior of the crush stress as a function of the crush rate and to contrast the results from the three different techniques. Combining the first technique's dynamic testing results along with the quasi-static testing of the honeycomb, crush stresses were measured for four different rates for a number of honeycomb samples. (See Figures 5-4, 5-5, 5-7 and 5-8.) These results along with the 95 percent confidence limits on the mean values are listed in Table 5-1 below. These crush stress results reveal a very mild increase in stress with increasing crush rate although these crush rates are still fairly low compared to actual applications.

Table 5-1. Measured crush stresses for various crush rates using the MTS machine, Technique One.

MTS Material Test Machine, Technique One			
Crush Velocity (in./sec)	**Mean Crush Stress (ksi)**	**Number of Test Samples**	**95% Conf. Limits**
0.0167	5.9	4	4 %
0.75	6.0	3	2 %
16.95	6.4	3	2 %
160.	6.3	6	3 %

The second technique included ten test samples and measured crush stresses for crush rates of 0 to 50 ft/sec (600 in./sec). (See Figure 5-15.) This set of data does reveal some scatter of about 6.5 percent about the mean; however, the trend of increasing crush stress with increasing crush rate is quite apparent. A clear mathematical relationship cannot be inferred from this data, though, because of the scatter from the samples and the oscillatory nature of the measured stress during testing. However, one can fit a least-squares straight line to the data to determine some relationship between crush stress and crush rate, although this should not be used to extrapolate beyond the 600 in./sec. Figure 5-23 shows all the measured data as points for each stress/velocity measured pair along with the best-fit straight line through the data.

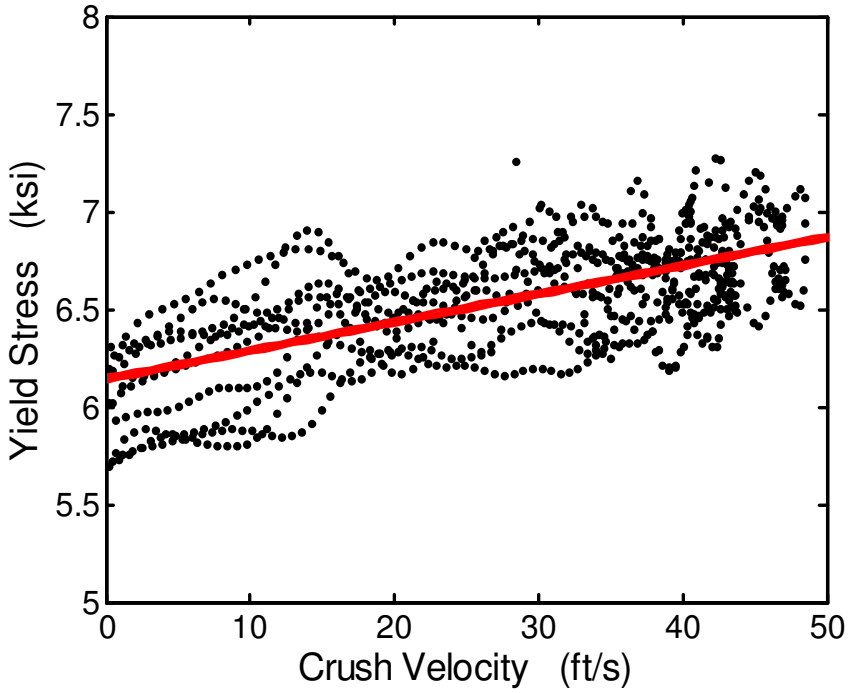

Figure 5-23. Measured crush stress from all ten honeycomb samples with the linear best-fit relationship.

The linear least-squares fit to the data produces the relationship

$$\sigma_{crush} = 6.1 + 1.21 * 10^{-3} (V_{crush}),$$

where the crush stress has units of ksi and the V_{crush} has units of in./sec. For this assumed least-squares fit, the constant term has an uncertainty of ±4 percent, while the slope term is ±1 percent. Of course, this is just the linear fit to the data; this does not imply there is a linear relationship between crush stress and crush rate, just that these data can be represented by a linear fit. Note that the linear relationship predicts an increase in crush stress of 725 psi over the quasi-static value for a 600 in./sec crush rate. This increase in crush stress represents about a 12-percent increase over the quasi-static value. The 6.1 ksi crush stress for quasi-static crush rate correlates extremely well with the data using Technique One, 5.9 ± 0.2 ksi, and the data in [2], which reported 6.3 ± 0.3 ksi.

For the third technique, there are really only two results for the crush stress and crush velocity because of the highly oscillatory stresses that resulted from this testing. These two results are merely the means of an entire set of measured data for Samples V4 and V5, so these results need to be viewed as with fairly high uncertainty. (See Figures 5-21 and 5-22.)

Table 5-2. Mean crush stresses and crush rates using the horizontal actuator, Technique Three.

Sandia Horizontal Actuator Testing, Technique Three		
Sample Name	**Mean Crush Rate (in./sec)**	**Mean Crush Stress (ksi)**
V4	377	7.1
V5	517	6.1

To consolidate and compare the data from all three test techniques, it is probably most revealing to display the results using a log scale for the crush rate because the measured crush rates span four and a half decades. Figure 5-24 shows a comparison of the individual results from Techniques One and Two with the large red squares indicating the individual measurement using the MTS machine (Technique One) and the smaller symbols representing the dynamic test data from the drop table (Technique Two). Using the log scale for the crush velocity does tend to pack most of the data points into the right-hand side of the plot, but it does reveal the behavior of crush stress with crush velocity. This figure shows all the individual test results without any averaging or estimation of the uncertainty, but one can see from this figure that the results from Techniques One and Two do blend into each other and reinforce the results for the crush stress. Note that the scatter in the data appears to be large due to the truncated vertical axis for the crush stress, but the scatter is actually only ± 6.5 percent about the mean.

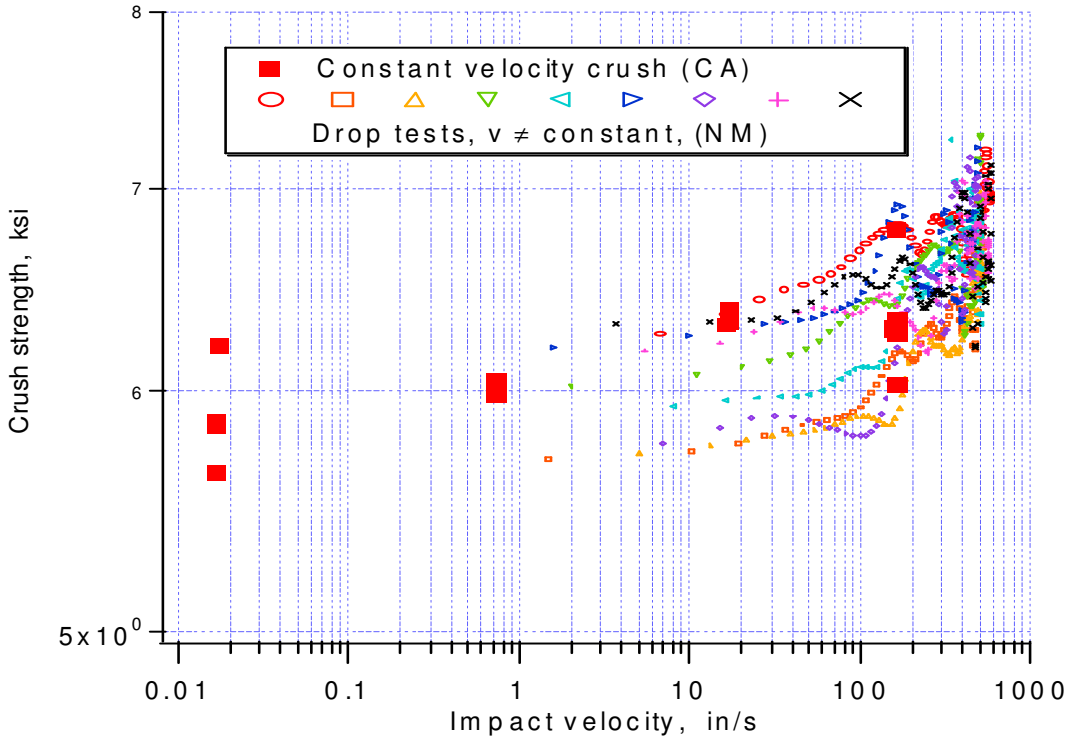

Figure 5-24. Crush stress versus crush velocity for Techniques One and Two.

The data from all three techniques can also be compared using the linear best-fit relationship derived from the data from Technique Two. Figure 5-25 shows the linear relationship, plotted in blue using a log scale for the crush rate, with the results from Techniques One and Three overlaid on the graph. Of course, the linear relation does not appear to be a straight line using log scale for the crush rate. Included with the blue linear relationship are two dash-dot curves showing the 95 percent confidence bounds for this estimation of the mean crush stress. The results from the first technique are represented by their mean values with vertical uncertainty bars at the four crush rates, rather than including all the individual sample data as in Figure 5-24. The results from Technique Three are indicated with asterisks, which have unknown large uncertainty. However, they do reinforce the measurements from Techniques One and Two in that they bound those results on the high and low sides.

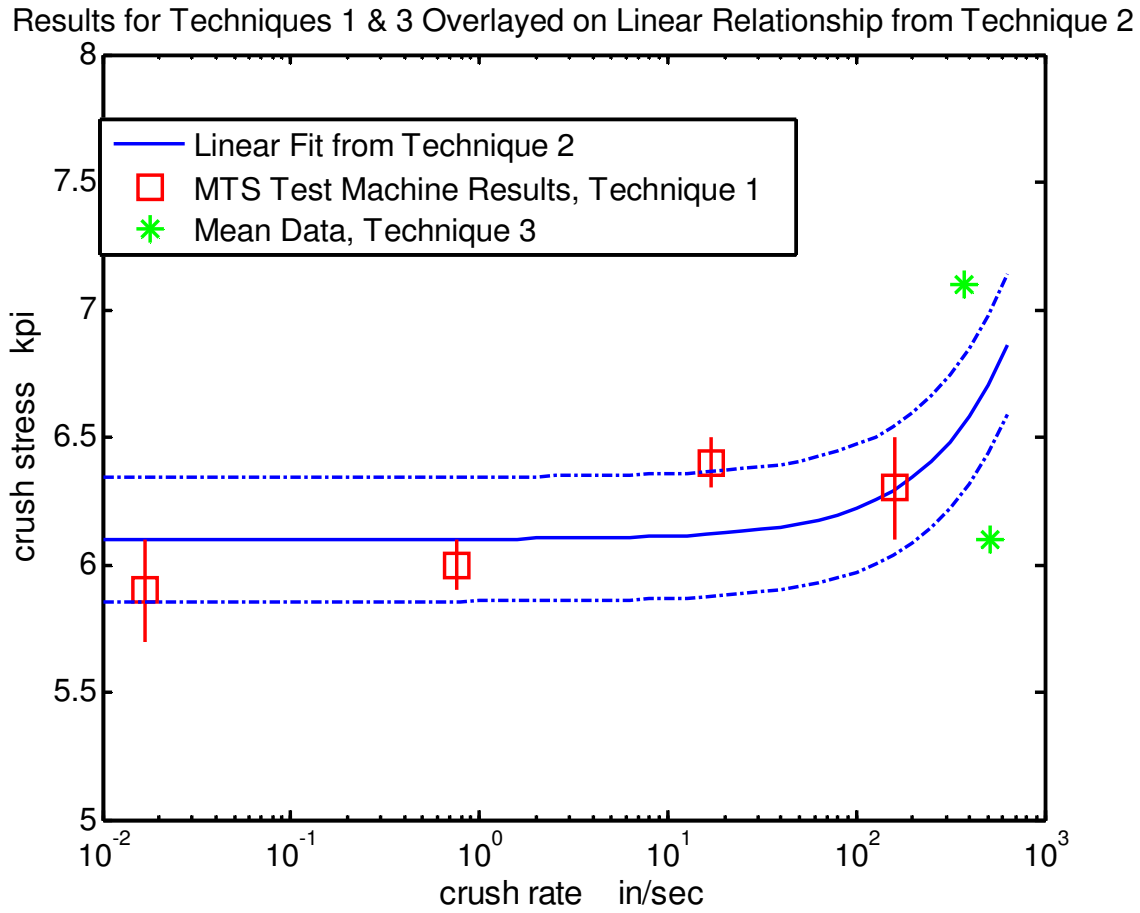

Figure 5-25. Crush stress results from all three techniques: Technique Two, linear fit; Technique One, mean plus uncertainty; and Technique Three, mean data.

Figure 5-25 presents a very clear picture of crush stress versus the crush rate. Displayed in the figure are three different techniques for measuring the crush stress using three different Sandia facilities at both California and New Mexico. The agreement between Techniques One and Two is most reassuring. Technique One involved tests at relatively low crush rates, but we can see

the crush stress increasing with crush rate. In contrast, Technique Two was a transient dynamic test involving crush rates from 0 to 600 in./sec. At the lower end of the crush rates, the agreement with Technique One is very good. Technique Three definitely has two outliner data points, but as discussed in the section on Technique Three, significant uncertainty exists with that data. From these results, the linear relationship between crush stress and crush rate should be used as part of the constitutive model up to crush rates of 600 in./sec. To extend to higher crush rate would be a real extrapolation of these current results.

Conclusions

Three different techniques, involving different facilities and different laboratories, have been developed and implemented to measure the dynamic crush strength of a high-density aluminum honeycomb. Crush velocities ranging between 0.0167 and 160 in./sec were obtained using an MTS material test machine, crushing the honeycomb at a constant rate. A test apparatus including a piston within a cylinder was use to confine and crush the honeycomb material. Crush velocities as high as 600 in./sec were obtained using a specially designed test fixture attached to the carriage of a standard drop table. Because the test was a transient dynamic test, the crush velocities varied throughout the crush event. Data processing was performed in order to associate a particular measured crush stress with a particular crush velocity. Using the measured data, there were numerous pairs of crush stress and crush velocity for each sample of material. A total of ten samples were tested, and all the data were used together to estimate a global, linear best-fit relationship between the crush stress and the crush velocity. The third technique involved using the 18-in. Horizontal Actuator in Area III to propel an impact mass into the honeycomb. Because of the tremendous oscillations in the crush stress, this technique did not yield as useful results and only was able to produce a broad average crush stress at two average crush rates.

In comparing and contrasting the results of the three techniques, the data from Technique One and Two blend together well between the low and high crush rates. Where the results from the two techniques overlap, the results match perfectly when the uncertainty of the measured data is included. The two results from Technique Three, which contain large but unquantified uncertainty, were on the low and high sides of the results from Technique Two. Overall, these various test data all support each other, and show the crush stress increasing with crush rate. At a crush rate of 600 in./sec the crush stress is 12 percent higher than that at a quasi-static rate.

References

[1] Bitzer, T., *Honeycomb Technology*, Chapman & Hall, London, UK, 1997.

[2] Stasiunas, Eric, Thomas Carne, and Brendan Rogillio, Axial Crush Strength of Tape-Confined and Segmented Honeycomb, Sandia National Laboratories internal memo, November 4, 2004.

[3] Lu, W.Y. and T.D. Hinnerichs, *Crush of High Density Aluminum Honeycombs*, IMECE/AMD-25453, November 2001.

[4] Hinnerichs, T.D., M.K. Neilsen, and W.Y. Lu, *A New Aluminum Honeycomb Constitutive Model for Impact Analyses*, IMECE2004-60751, November 2004.

Intentionally left blank

CHAPTER 6. TIER I VALIDATION: MATERIAL BEHAVIOR

Wei-Yang Lu and Terry Hinnerichs

Tier I is the simplest approach to calibrating a model, sometimes called "single-physics" validation. The single-physics expression implies that the experiments and modeling focus only on the honeycomb physics and not any associated structure around it. The Tier II validation in Chapter VII includes a confinement structure around the honeycomb. This chapter presents the test matrices and experimental data for validating the new Honeycomb Crush Model (HCM) in the Tier I mode along with a validation metric for measuring the accuracy of the model relative to test data.

After the new HCM model is calibrated, based on the preceding parameter identification process described in Chapter 4, it will be used to predict the behavior of experiments defined in the validation test matrix given in Table 6-1. The tests chosen for validation, in Table 6-1, are all off-axis tests. They were chosen to quantify the predictive accuracy of the HCM model where it is thought to be the least accurate and for a configuration that is important to the operational space of the B61. Also, note that the TW20 test configuration is listed both in the biaxial system and in the confined chamber parts of the test matrix. This was planned in order to quantify differences between the biaxial system with one free direction and the chamber with full confinement.

Table 6-1. Validation test matrix.

Test Rig	Type of Load	Orientation	Temperature
Biaxial system	Uniaxial with inplane confinement	TW20	Ambient
		LW20	
Uniaxial Chamber	Uniaxial with full confinement	TL20	Ambient
		TW20	
Biaxial System	Equal biaxial with inplane confinement	TL45	Ambient
		TW45	
		LW45	

Validation Metric

An important measure of quality/accuracy in a shock mitigation device model is how well it predicts the amount of energy absorbed by the device during an impact. For the reason of tracking energy absorption and to avoid tracking every oscillation on a time-history curve of force and displacement, the measurement, or metric, chosen for determining the quality of fit between model and test data will be based on energy as shown in Equation 6-1.

$$E_{metric} = \int_0^{\varepsilon_{\max}} \sigma * d\varepsilon \qquad \text{(Eq. 6-1)}$$

This energy-based metric is an integral method that will factor in the general shape and the area under the curves. It is based on matching energy absorbed in the model and the test data over three intervals, at the 1/3, 2/3, and full-energy points. The full-energy point will be chosen at the maximum strain level of the test or the strain level at which the test deviates from the intended loading; e.g., the strain level in the equal biaxial tests where out-of-plane swelling begins and invalidates the test data.

Figure 6-1 shows a comparison between the stress-strain curves predicted by the new HCM and the old Orthotropic Crush Model (OCM) for the TW00 equal biaxial test. In this case the OCM has been fit with the equivalent crush strength values in each orthogonal direction as the HCM. Notice how the engineering stress for the OCM decreases with strain and diverges from the test data. This observation motivated the addition of the TWP function (Equation 2-4), described in Chapter 4, to account for apparent "conservation of structural strength" as the cells are compressed. The OCM yields similarly poor results for the TL00 configuration.

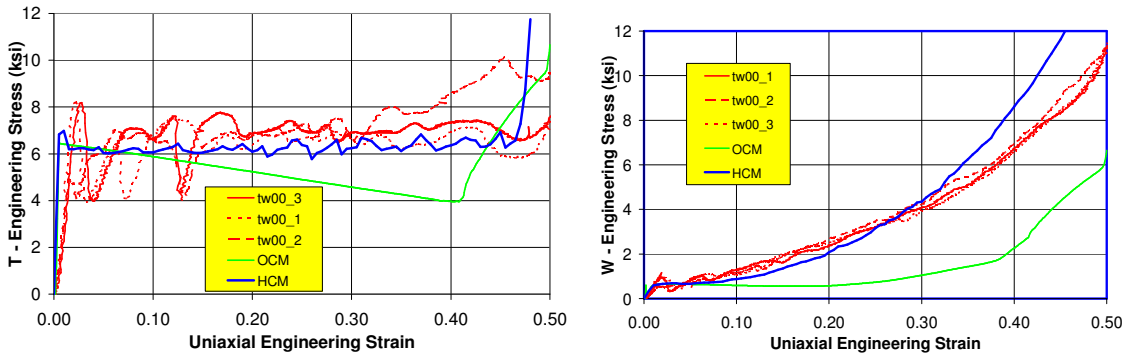

Figure 6-1. Comparison of HCM with OCM and test data for TW00 biaxial compression: (a) T direction and (b) W direction.

Figure 6-2 shows the application of the energy metric for three test data curves and for the HCM and OCM model predictions that were shown in Figure 6-1a. The curves were normalized by dividing by the integrated experimental strain energy at 0.5 strain in test TW00_1. A good metric should display trends similar to those observed in basic variables, such as is given in Figure 6-1a. The energy metric does this. The HCM metric curve agrees with the test metric curves out to max strain, whereas the OCM metric diverges after about 20 percent strain.

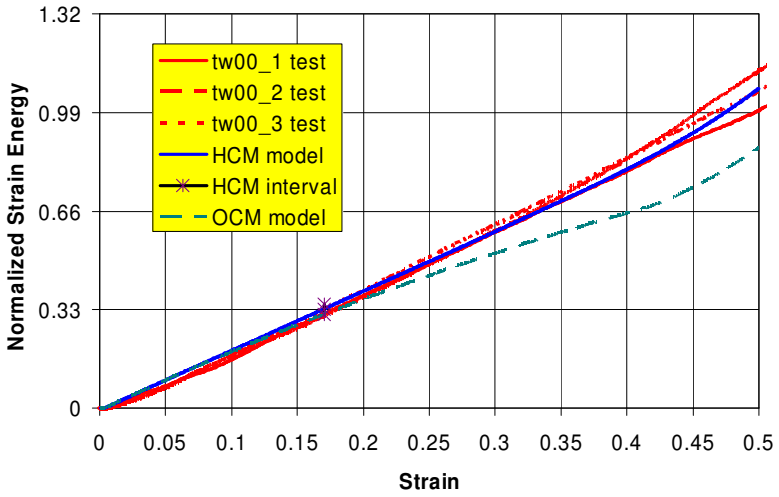

Figure 6-2. Energy metric application.

Figure 6-3 shows a close-up of the area around the 0.33 energy point shown in Figure 6-2. A confidence interval, e.g., 95 percent, is shown for the HCM model results as a vertical black line. For discussion purposes, consider the interval between the minimum and maximum test curves to be the confidence interval for the test data. For a model to be valid there should be overlap of the model and test intervals. The amount of overlap required for a model to be valid should not be so restrictive that a good model is rejected or so liberal that a poor model is accepted. The amount of overlap generally is a joint decision among experimentalists, analysts, and system designers or customers, and should be favorable to what looks like a good fit graphically, as shown in Figure 6-1 when comparing the HCM model with the test data. To complete the model validation assessment for these data, a similar quantification of the amount of overlap of model and number of test confidence intervals would be done at the 2/3 and full-energy dissipation points. Clearly, the overlap should be chosen so that the OCM would be rejected for strains greater than 20 percent, where it diverges substantially from the trend of the test data.

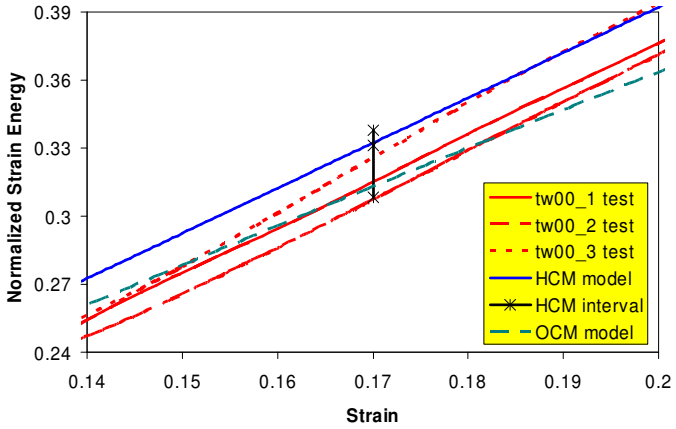

Figure 6-3. Close-up of energy metric at the 1/3 energy point.

The validation experiments will now be described. However, the application of this validation metric to all of the validation experiments will be shown in a later report.

Uniaxial Validation Experiments in the Biaxial Test Rig

As described earlier, during uniaxial crush on the biaxial system, the East and West actuators move toward each other at a constant speed of 0.5 in./min, while the North and South actuators do not move but confine the deformation of honeycomb specimen. Both crush load and confined load were recorded. The remaining two faces that were normal to the loading plane were traction free.

Table 6-2 describes the dimensions, mass, density, and loading rate corresponding to each specimen that was uniaxially crushed in the biaxial test rig.

Table 6-2. Uniaxial experiments on the biaxial system for validation.

	W(1)	W(2)	Height	Mass	Density	Rate
Specimen	**(in.)**	**(in.)**	**(in.)**	**(g)**	**(pcf)**	**(in./sec)**
LW20_1	2.012	1.975	1.518	62.21	39.29	1.67E-02
LW20_2	1.995	2.010	1.517	62.94	39.42	1.67E-02
LW20_3	1.990	2.004	1.516	62.57	39.43	1.67E-02
TW20_1	1.993	1.997	1.499	61.07	39.00	1.67E-02
TW20_2	1.992	2.003	1.488	61.00	39.14	1.67E-02
TW20_3	2.005	2.011	1.512	61.52	38.44	1.67E-02

Figure 6-44 shows the results of a uniaxial crush of the TW20 configuration. Figure 6-4a shows the load measured in the loading, or East, direction, and Figure 6-4b shows the load measured in the confined, or North, direction. There is a large amount of scatter between tests in the North direction.

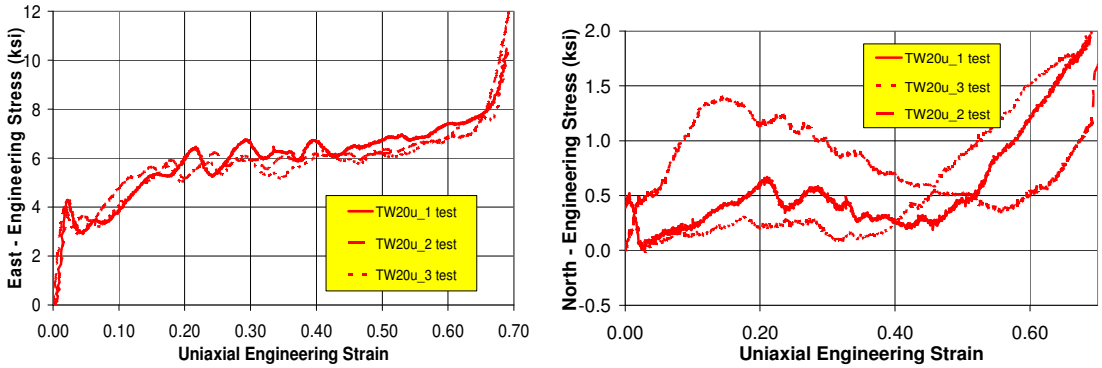

Figure 6-4. TW20 uniaxial test data at ambient: (a) loading direction and (b) confined direction.

Figure 6-5 shows the results of a uniaxial crush of the LW20 configuration. Figure 6-5a shows the load measured in the loading, or East, direction, and Figure 6-5b shows the load measured in the confined, or North, direction. The data are fairly repeatable.

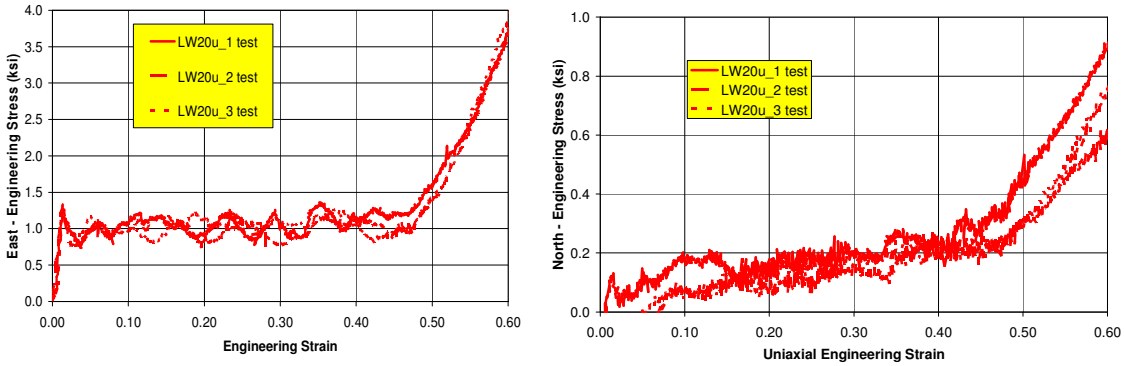

Figure 6-5. LW20 uniaxial test data: (a) loading direction and (b) confined direction.

Uniaxial Calibration Experiments in the Confinement Chamber

During uniaxial crush in the confinement chamber, only one actuator is loading the specimen in the axial direction at 0.0167 ft/sec. Only the crush load is measured in the axial direction. The remaining two faces that were normal to the loading plane are confined by the chamber walls.

Table 6-3 lists the dimensions, mass, density, temperature, and loading rate for each specimen tested in the confinement chamber for validation data.

Table 6-3. Uniaxial Experiments in the Confinement Chamber for Validation.

Specimen		W(1)	W(2)	Height	Mass	Density	Temp.	Rate
Type	#	(in.)	(in.)	(in.)	(g)	(pcf)	(°F)	(in./sec)
TL20	1	1.184	1.218	1.736	24.27	36.93	70	0.0167
TL20	2	1.218	1.200	1.754	25.79	38.32	70	0.0167
TL20	3	1.190	1.211	1.734	24.87	37.91	70	0.0167
TW20	1	1.210	1.220	1.746	26.23	38.77	70	0.0167
TW20	2	1.214	1.203	1.759	26.39	39.13	70	0.0167
TW20	3	1.214	1.220	1.762	26.54	38.74	70	0.0167

Figure 6-6 shows the results from a uniaxial crush of the TL20 configuration. The data have an approximate scatter range of 30 percent in places.

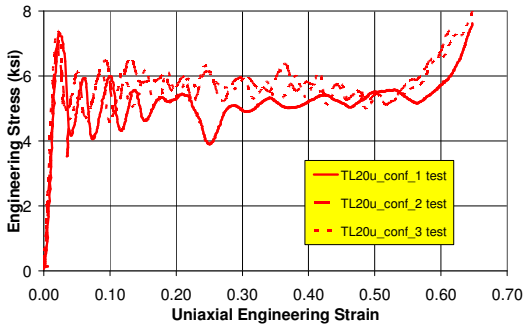

Figure 6-6. TL20 uniaxial validation test data from confinement chamber.

Figure 6-7 shows the results of a uniaxial crush of the TW20 configuration from both the confinement chamber and, for comparison, from the biaxial rig (Figure 6-4a). Similar results come from both tests, and the data look fairly repeatable.

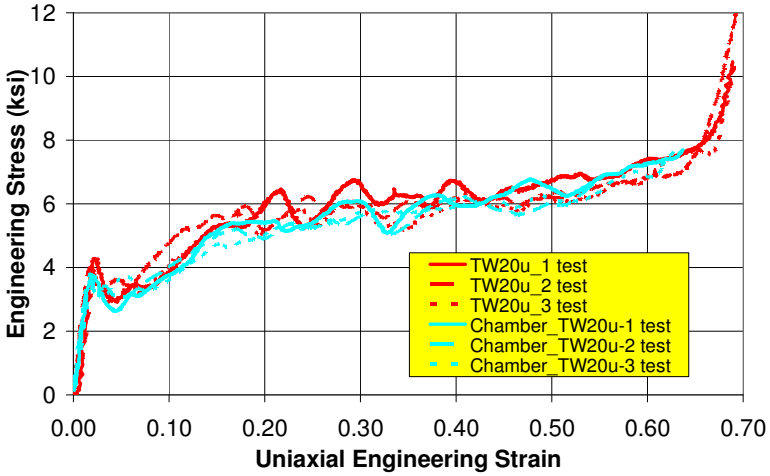

Figure 6-7. TW20 uniaxial validation test data from confinement chamber.

Equal Biaxial Validation Experiments

In these tests, as mentioned earlier, both East-West and North-South pairs of actuators in the biaxial rig move toward each other at the same rate, loading the specimen in two orthogonal directions. The out-of-plane direction is traction free. Table 6-4 lists the dimension, mass, density, and testing rate for each specimen tested with equal biaxial loading.

Table 6-4. Equal biaxial crush experiments for validation.

Specimen	W(1) (in.)	W(2) (in.)	Height (in.)	Mass (g)	Density (pcf)	Rate (in./sec)
TL45_1	1.188	1.218	1.750	25.44	38.27	1.67E-02
TL45_2	1.212	1.211	1.751	25.92	38.42	1.67E-02
TL45_3	1.207	1.205	1.755	25.36	37.85	1.67E-02
TW45_1	2.030	2.007	1.537	63.28	38.50	1.67E-02
TW45_2	2.010	2.040	1.515	63.10	38.70	1.67E-02
TW45_3	2.010	2.040	1.520	63.39	38.75	1.67E-02
LW45_1	1.991	2.048	1.516	63.91	39.39	1.67E-02
LW45_2	1.983	2.015	1.519	62.81	39.42	1.67E-02
LW45_3	2.011	2.005	1.522	63.81	39.61	1.67E-02

Figure 6-8a shows the results of the TL45 biaxial crush in the North direction, and Figure 6-8b shows the results in the East direction.

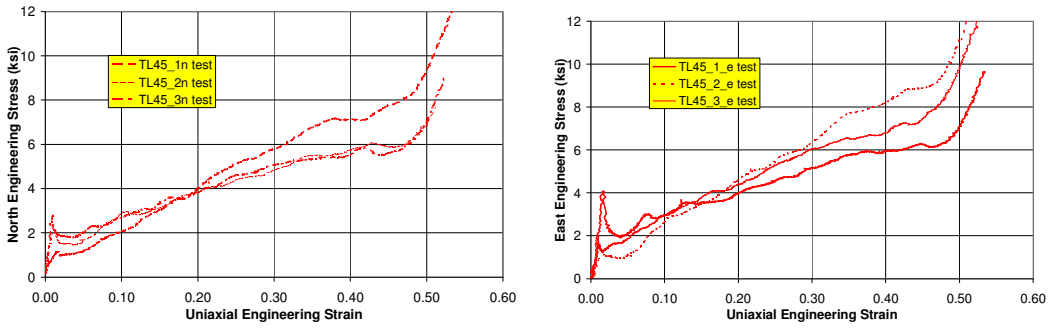

Figure 6-8. TL45 equal biaxial crush test data at ambient: (a) North-South direction and (b) East-West direction.

Theoretically, the crush stress should be the same in both directions for these 45-degree orientations. However, physically, the test articles have imperfections, are not aligned perfectly, and the friction of the platens causes asymmetries.

Figure 6-9a shows the results of the TW45 configuration in the North direction, and Figure 6-9b shows the results in the East direction. There is quite a bit of scatter in the data after 20 percent to 30 percent strain levels. Here, the honeycomb is forming different buckle patterns and is splitting.

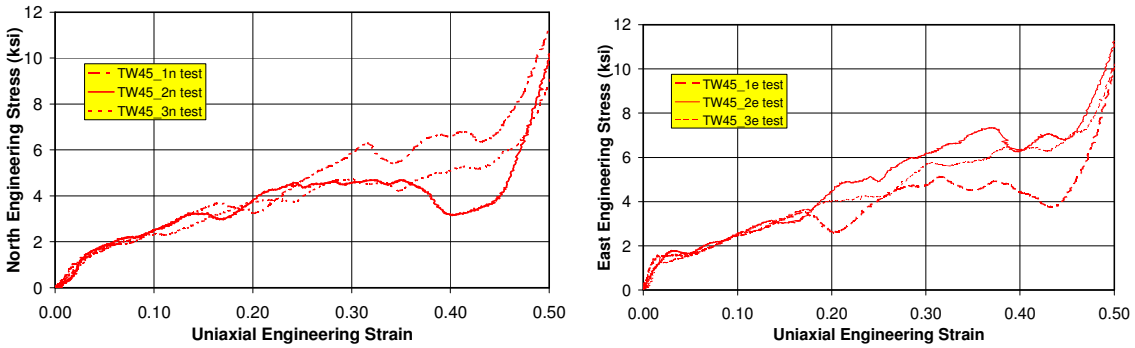

Figure 6-9. TW45 equal biaxial crush test data at ambient: (a) North-South direction and (b) East-West direction.

Figure 6-10 shows the LW45 configuration in which the two weakest material directions are interacting. In this case, North and East direction data were plotted on the same graph since they are similar.

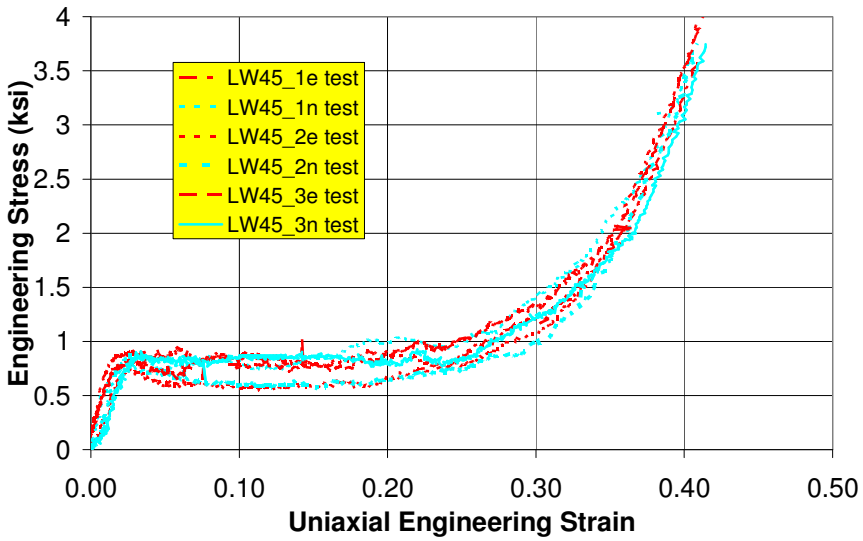

Figure 6-10. LW45 equal biaxial crush test data.

CHAPTER 7. TIER II VALIDATION: COMBINED PHYSICS

Eric C. Stasiunas, Thomas G. Carne, Terry D. Hinnerichs, and Brendan R. Rogillio

Abstract

In order to create an analytical model of a material or structure, two sets of experiments–calibration and validation–must be performed. Calibration experiments provide the analyst with the parameters from which to build a model that encompasses the behavior of the material. Once the model is calibrated, the new analytical results must be compared with a different, independent set of experiments, referred to as the validation experiments. This modeling procedure was performed on the B61 honeycomb material, with the validation experiments presented here. This report covers the design of the validation experiments, the analysis of the resulting data, and the metric used for model validation.

Introduction

The central goal of the validation experiments was to evaluate the energy absorption of high-density (38 lbf/ft^3) Hexcel Corporation aluminum honeycomb [1] in a way that much of the model's range of desired applicability would be evaluated. For experimentation, the honeycomb was implemented into a two-layer test structure, designed to measure the energy absorbing qualities of the material in its design application, which is defined in the stockpile-to-target sequence (STS) requirements [2, 3]. Experiments on the honeycomb test structure were performed from a defined validation space. The validation space included compliant structural confinement, elevated temperature, dynamic crushing strains, and off-axis loading. The quantification of uncertainty due to honeycomb material variability, part-to-part variability, and transducer uncertainty was addressed. Once honeycomb crush energy was obtained from test data, displacements at 1/3, 2/3, and 3/3 of the total absorbed energy and the corresponding 95 percent confidence intervals were calculated.

The honeycomb is modeled as an orthotropic material with three defined orthogonal directions—the T, L, and W directions as shown in Figure 7-1—used to fully describe the material parameters. From previous experimentation, the T direction has been proven to exhibit the highest yield strength, followed by the much lower yield strength L direction, followed by even weaker yield strength W direction. Honeycomb is typically oriented in the T direction for use in energy absorption applications [2].

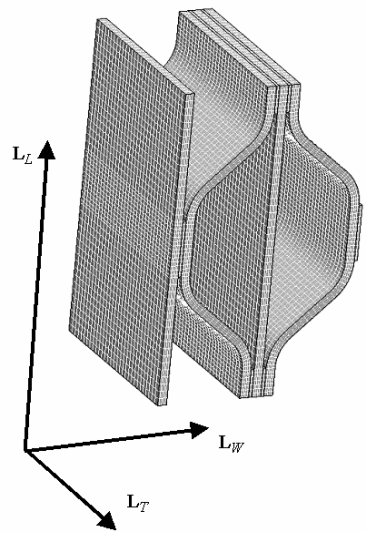

Figure 7-1. Orthogonal directions of honeycomb.

Validation Space

In order to validate the honeycomb model, a validation space was identified that would encompass all the environments of the honeycomb in its B61 design application. The validation space included: confinement of the honeycomb, segmented honeycomb orientation, angle of attack (AoA), impact angle, temperature, and velocity. The validation space diagram is shown in Figure 7-2. Colored areas on each validation axis represent parameters that were tested in the process of validating the honeycomb model. Each validation space axis is subsequently discussed in detail.

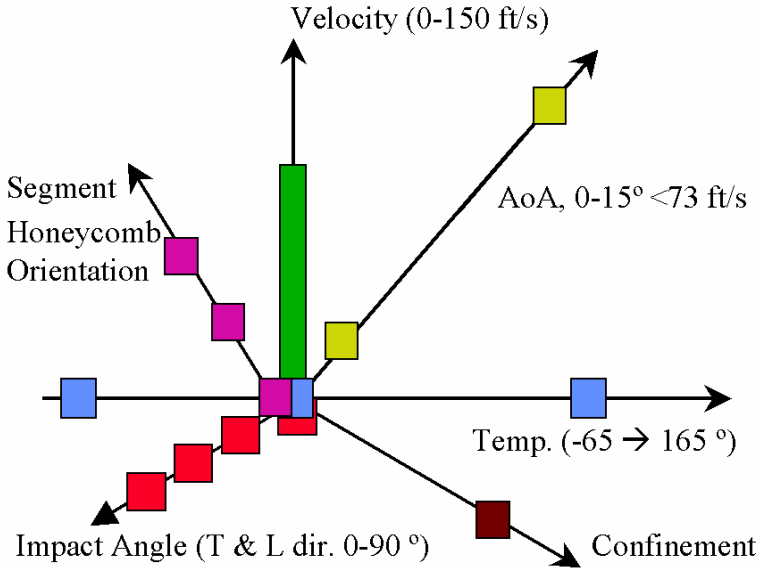

Figure 7-2. Validation space.

The confinement criterion of the validation space, required by the design application of the honeycomb, was exercised for all the Tier II validation experiments presented in this report. This requirement was satisfied by the design of a two-layer aluminum shell structure that contained the honeycomb. Details of this shell structure are discussed in a subsequent section of this report.

Segmented honeycomb is a design concept that creates a cylindrical section of honeycomb that exhibits approximately the same crush strength in any radial direction. Figure 7-3 shows an example of segmented honeycomb that has been cut into four 90° wedges and glued together so that the L direction is approximately aligned radially. For a lateral crushing impact on a cylindrical section of the segmented honeycomb, responses will differ depending on the exact orientation of the segmented honeycomb in relation to the impact. Therefore, the segmented honeycomb orientation was included in the validation space for testing and model prediction.

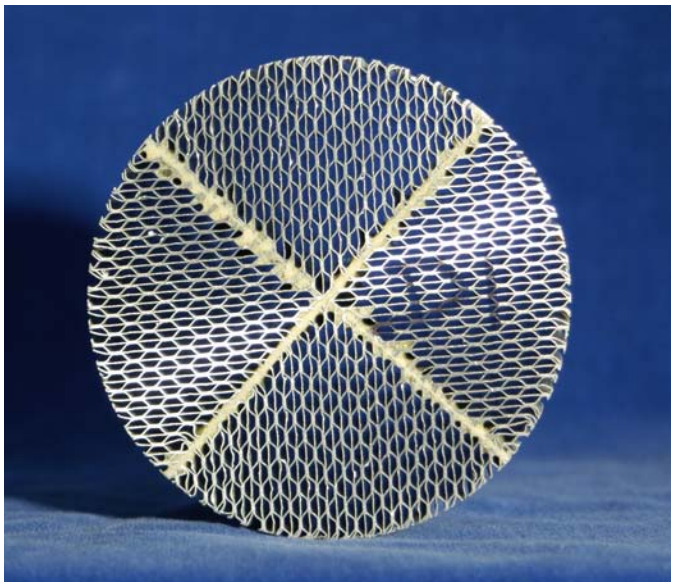

Figure 7-3. Segmented honeycomb.

The AoA was defined as the angle between the velocity vector of the structure and the axis of the structure itself, as shown in Figure 7-4. For validation experiments, two AoAs were applied to the honeycomb test structure—3° and 20°. Initially, a 0° AoA was desired, but not used for two experimental reasons: (1) an exact 0º AoA would be almost impossible to obtain due to the shift of the test structure that occurs during testing, and (2) the accelerometers could become overly excited with a 0° AoA, resulting in overloaded measurement signals. Therefore, a 3° AoA was deemed a reasonable compromise that would reduce the potential problems associated with a 0º AoA. The 20° AoA was chosen for experimentation because it slightly exceeds the impact condition of a B61.

The impact angle is defined as the angle between the axis of a structure and the target surface. Although this criterion is listed in the validation space diagram, impact angles of 87° and 70° were performed for the Tier II validation testing. Previous material model testing with various impact angles have already been performed and are discussed in [3] and [4]. The impact angle of the diagram in Figure 7-4 is the complement of the AoA.

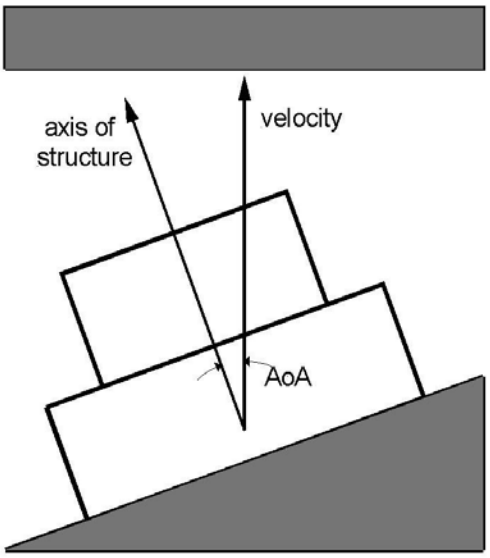

Figure 7-4. Angle of attack (AoA).

The temperature of the honeycomb material was varied for the validation experiments as specified in the validation space. Room temperature (77 °F) and 165 °F were the two values of temperature used. The larger of the two, 165 °F, was selected from the STS for the B61.

The last validation space criterion, velocity, is defined as the impact velocity, or crush velocity, experienced by the honeycomb. The crush velocities used for the presented validation experiments ranged from approximately 0 – 85 ft/sec. Quasi-static tests, performed in the lower range of the crush velocities (1 in./min), provided a way to obtain quality data of the honeycomb crush through precise instrumentation. Dynamic high-speed tests, with impact velocities reaching 85 ft/sec, were performed so that experimental data could be obtained near the maximum application velocity of the honeycomb, which was 150 ft/sec. Impact speeds above 85 ft/sec were unobtainable due to experimental facility limitations.

Validation and Uncertainty

While designing and performing the validation experiments, the issue of uncertainty quantification was addressed. Several factors of uncertainty were present during testing: sample variability, measurement uncertainty, and test condition variability. To quantify the amount of uncertainty, three repetitions of each test were performed.

Sample variability is the variability that occurs between individual samples of the honeycomb material. The material itself is manufactured from aluminum sheets and glue, presenting numerous chances for the material to differ locally. For example, the bonding area can vary greatly throughout a block of honeycomb as shown in Figure 7-5. Sample variability can result from machining the test samples from larger blocks of honeycomb as well, due to the cutting machine tolerance and the alignment of the honeycomb when cut.

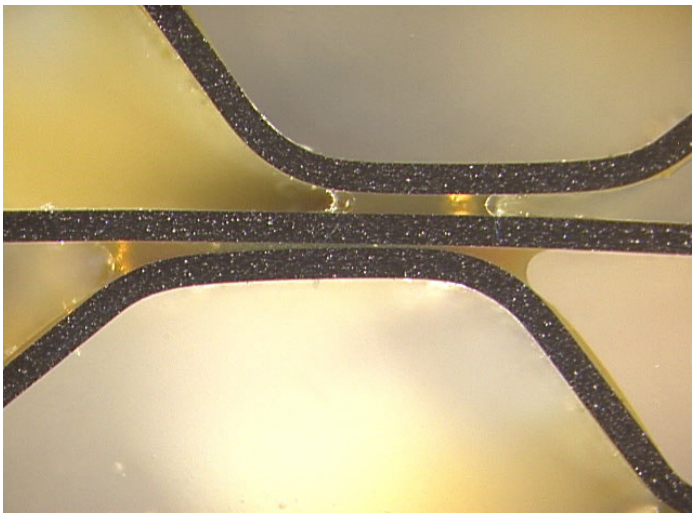

Figure 7-5. Variable bonding area in honeycomb sample.

Measurement uncertainties are a direct result of the sensitivities of the transducers and instrumentation used in the validation tests. These sensitivities need to be accounted for due to the many parameters being measured: force, acceleration, velocity, displacement, and temperature. Because the force and crush displacements were critical validation quantities, special attention was directed to obtaining these measurements. The crush force was measured with two different techniques using independent instrumentation: force transducers and inertial acceleration. The crush displacement was also measured with two unique technologies: integration of acceleration data and direct photographic analysis.

The final source of uncertainty is test condition variability. This variability results from the numerous conditions that can vary for the same test on the various samples. For example, the exact angle of impact in the dynamic validation tests is unknown and not measured directly. However, the maximum possible variability is known, and is accounted for in the data analysis.

Validation Metric

The metric used for validating the analytic honeycomb model was the energy absorbed during crush, or crush energy (in.-lbs). Energy was not measured directly for either the quasi-static or dynamic tests; it was calculated by the integration of the force as a function of the crush displacement. The crush energy metric was determined as the best metric for validation purposes since the ability to absorb energy is the critical design feature of the honeycomb material.

The first step in validating the honeycomb model involved defining a total crush displacement from the measured data, for each test configuration. Next, the total energy absorbed during this crush displacement was calculated from the force data. Finally, the honeycomb crush displacement values corresponding to the 1/3, 2/3, and 3/3 energy values were determined. These energy and displacement values will provide validation data for the analytical model and will determine if the model is acceptable. Figure 7-6 illustrates the energy validation metric.

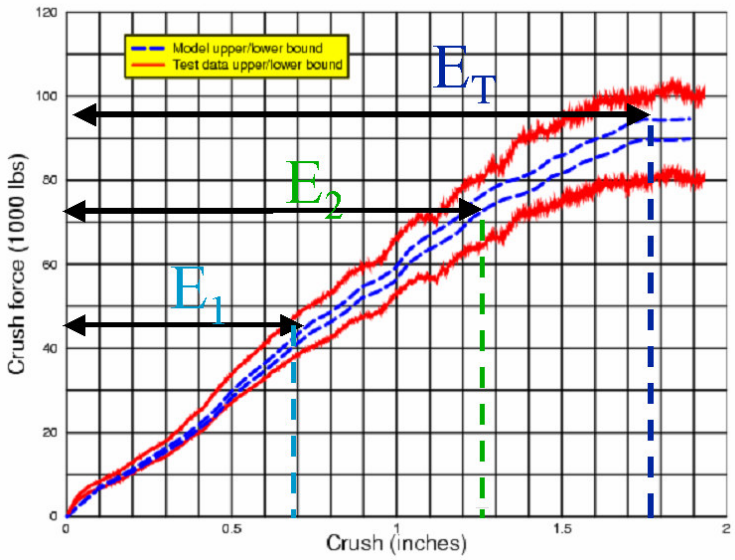

Figure 7-6. Energy validation metric.

Validation Experiments

The honeycomb validation test matrix, shown in Table 7-1, was designed from the previously discussed validation space. The "Series" column lists the names of the test series and samples. The "Configuration" column lists the configuration of the honeycomb material, which will be discussed in the subsequent paragraphs. The "Temp." column lists the temperature of the honeycomb material required for that particular test series. As indicated by the final column, "Units," three test samples, or units, were tested for each configuration.

The validation space criterion used for a majority of the testing was the confinement of the honeycomb material. In an effort to confine the honeycomb and represent the B61 forward mount configuration, a two-layer test structure, also referred to as a two-layer cake, was designed and is shown in Figure 7-7. The two-layer cake configuration consisted of placing two circular honeycomb samples of different diameters and orientations into an aluminum shell, one on top of the other. The topmost, smaller-diameter honeycomb was segmented; the bottom, larger-diameter honeycomb was uniform material, orientated axially in the L direction. Separating the honeycomb samples was a thin load spreader plate with a nominal thickness of 0.025 in.. The nominal wall thickness of the 6061-T6 aluminum shell was 0.035 in. and the diameters for the top and bottom were 3 in. and 4 in., respectively. Once assembled, the two-layer structure provided the required confinement to the honeycomb, with the characteristics of a B61 energy absorber.

Table 7-1. Validation test matrix.

Quasi-static Test Matrix ~ 0 ft/sec			
Series	**Configuration**	**Temp.**	**Units**
J	3° X on L	T_o	3
K	20° X on L	T_o	3
L	20° + on L	T_o	3
M	20° + on L	165° F	3
W	3° X on L	165° F	3
Dynamic Test Matrix ~ 6—85 ft/sec			
Series	**Configuration**	**Temp.**	**Units**
R	3° X on L	T_o	3
S	3° X on L	165° F	3
T	20° X on L	T_o	3
U	20° X on L	165° F	3

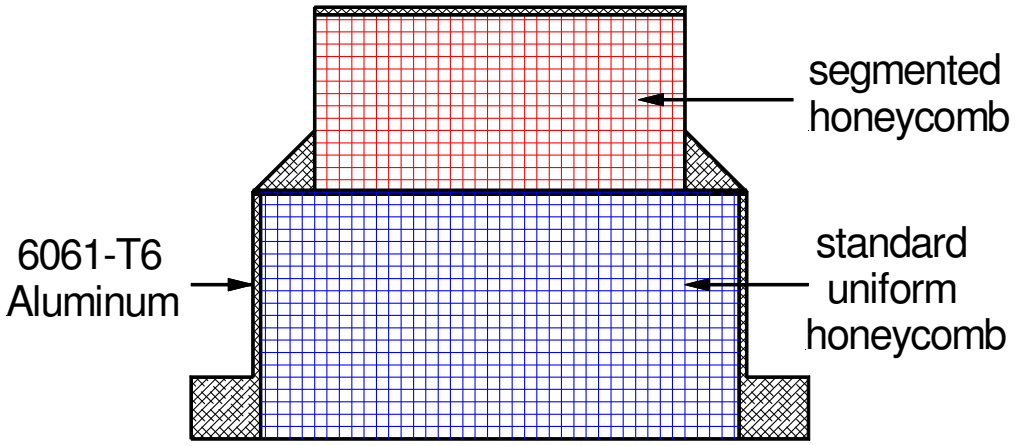

Figure 7-7. Two-layer honeycomb test structure (two-layer cake).

In its original state, the aluminum shell was very reflective, and would be difficult to discern how the structure deforms when examining post-test photographs. To eliminate the reflectivity, the shell was painted white, and to better discern the edges, black marker lines were drawn on the edges of the shell. The white color and black edge lines were very useful when performing data analysis from the test photographs.

The orientation of the segmented honeycomb in the top of the two-layer test structure was varied for the quasi-static tests and held constant for the dynamic tests. This orientation, defined as X or +, is determined by what point on the segmented honeycomb first comes into contact with the applied force. If the applied force contacts the honeycomb directly in between the glue joints, this is considered an X orientation. Alternately, if the applied force contacts the honeycomb at a glue joint, this is considered a + orientation. Figure 7-8 is a diagram illustrating the two orientations.

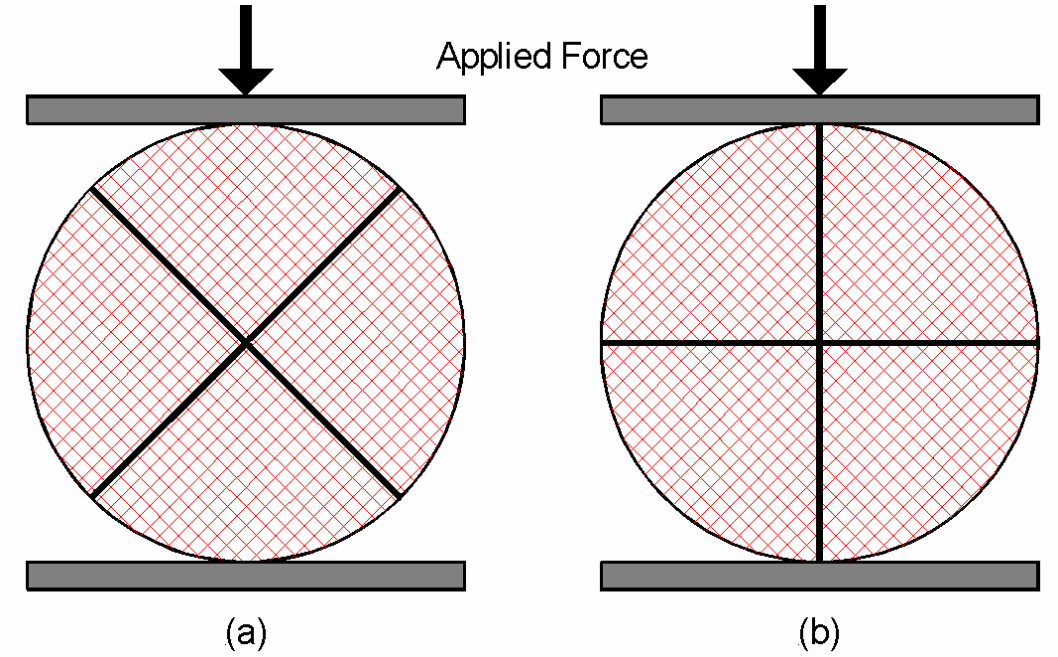

Figure 7-8. Segmented honeycomb: (a) X orientation (b) + orientation.

The next validation criterion to be addressed in the test design was the AoA. As mentioned previously, when applying the crush force to the two-layer cake, it was desired that this force be applied at the two angles, 3° and 20°. To accomplish this requirement, two AoA blocks were manufactured with these desired angles. These AoA blocks would position and secure the two-layer cake during the application of the crush force.

The final component of the test design was the implementation of the force transducers. Because every test required the honeycomb structures to experience crush force, four biaxial Kistler 9378BU force transducers, each with an axial force limit of 100 kN (22,480 lb) were installed parallel to each other, between two large plates. The top plate attached to the AoA block and the bottom plate attached to the load frame platen for quasi-static tests, or to the seismic mass for dynamic tests. The crush forces could then be measured through the summation of the four axial force outputs. A diagram of the validation test fixture, with the force transducers, AoA block, and the two-layer test structure, is in Figure 7-9.

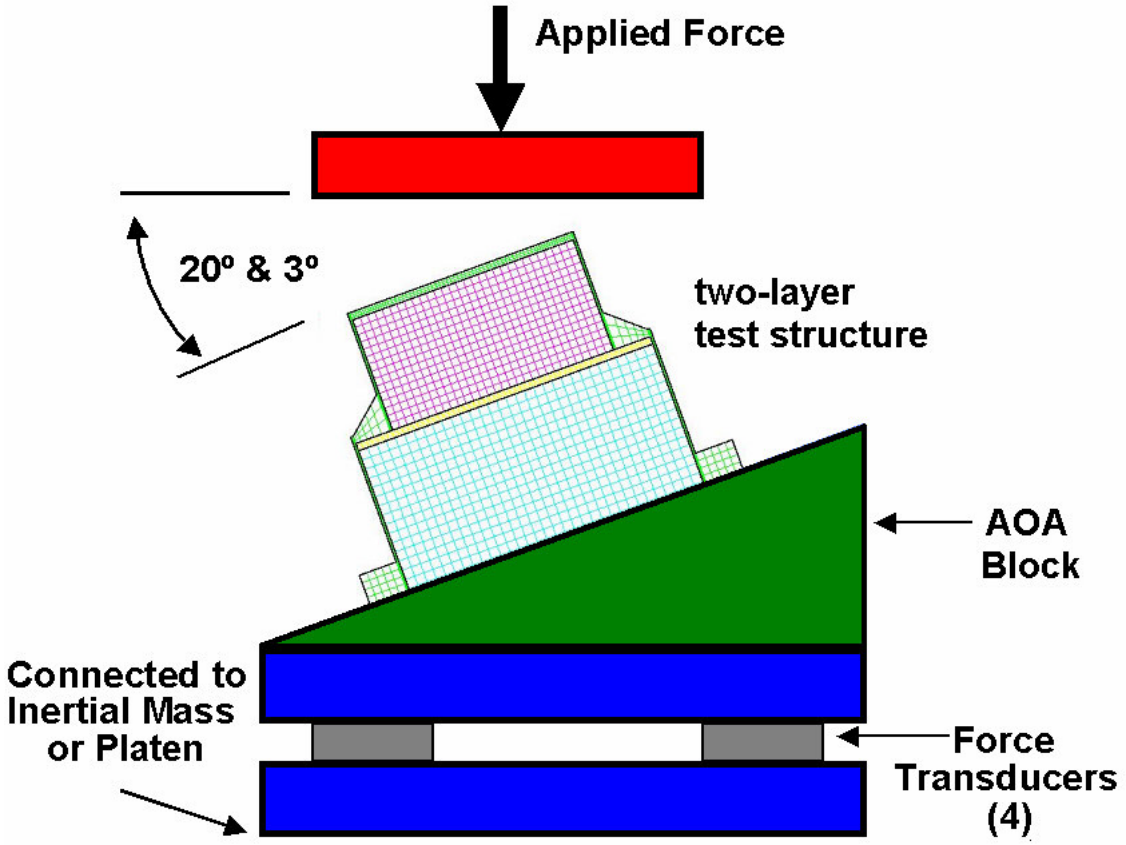

Figure 7-9. Validation test fixture (with two-layer test structure).

An oven was used to raise the temperature of the honeycomb material for the application space requirement of 165 °F. Performing these elevated temperature tests involved heating the honeycomb structure to a temperature above 165 °F, allowing for test setup time performed outside the oven. After test setup, thermocouples installed inside the structure were used to monitor the temperature. Once the temperature decreased to 165 °F, the test began.

The validation matrix required that the honeycomb material be crushed at various speeds. Therefore, crush velocities from 0 – 85 ft/sec were obtained using two different types of tests—quasi-static and dynamic tests. Both types of tests result in obtaining the energy metric used to validate the model. However, the two types of tests will be discussed separately due to their significant differences.

Quasi-static Testing

To satisfy the validation space at the very low (almost zero) crush velocity range, several configurations of honeycomb structures were tested quasi-statically. Quasi-static tests provided a way to obtain quality force and crush displacement data of the honeycomb test structure through precise instrumentation. The test plan for the quasi-static crush of honeycomb is reprinted in Table 7-2.

Table 7-2. Quasi-static test matrix.

Series	Configuration	Temp.	Units
J	3° X on L	T_o	3
K	20° X on L	T_o	3
L	20° + on L	T_o	3
M	20° + on L	165° F	3
W	3° X on L	165° F	3

A load frame from the Sandia Structures Laboratory was used to perform the quasi-static tests on the honeycomb structures. The nominal displacement rate of the load frame was 1.0 in./min. During the test, force and displacement was measured and a digital camera was used to capture images of the crush process every 5 seconds. Once the test fixture had been crushed sufficiently, usually 2 in. or less, the test was concluded. The quasi-static test setup for test Sample J1 (3° AoA) is shown in Figure 7-10.

The resulting force and deformation data measured from the quasi-static test for all three samples of Test Series J is shown in Figure 7-11. The units of force and deformation are pounds and inches, respectively. To accompany the data plot, images capturing the honeycomb crush event are shown in Figure 7-12. In the interest of space, of the 28 photos taken during testing, just a sample of six is shown to illustrate the nature of the honeycomb structure crush.

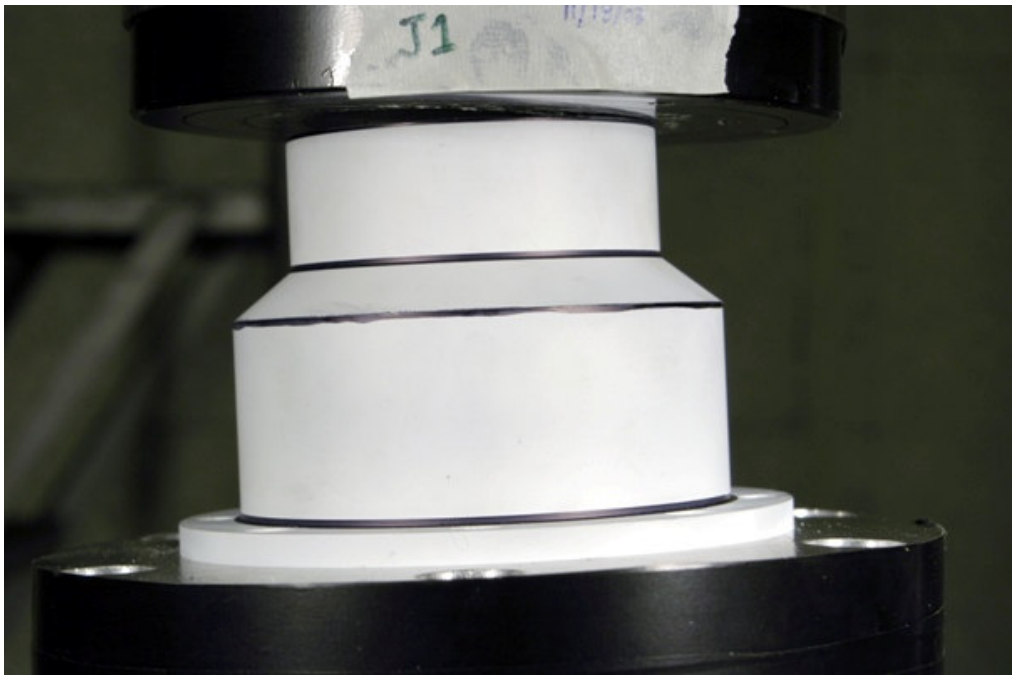

Figure 7-10. Quasi-static test setup (3° AoA).

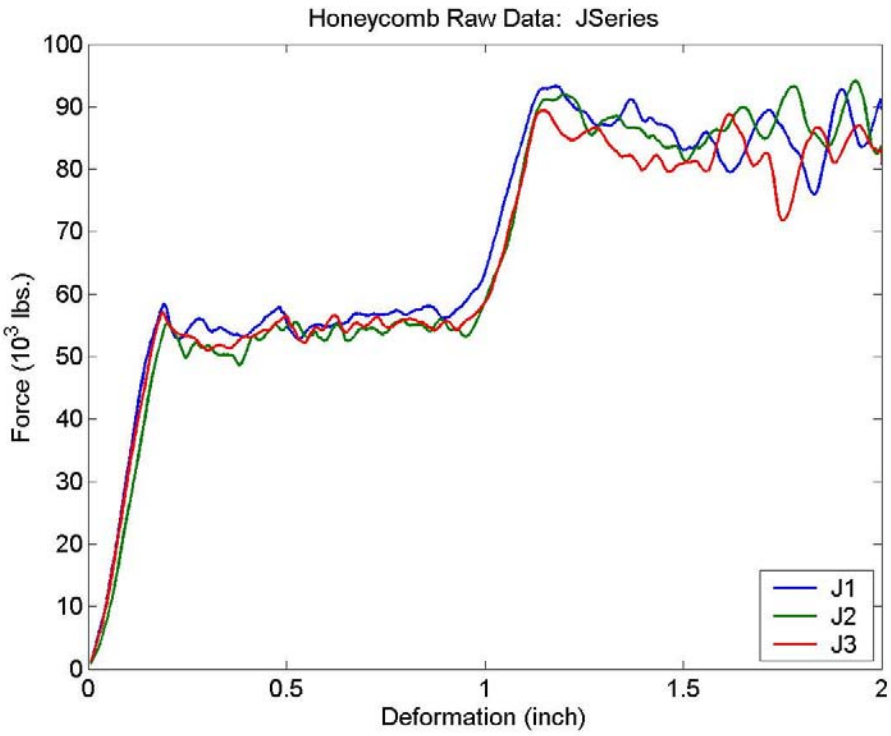

Figure 7-11. Crush force versus deformation (Series J).

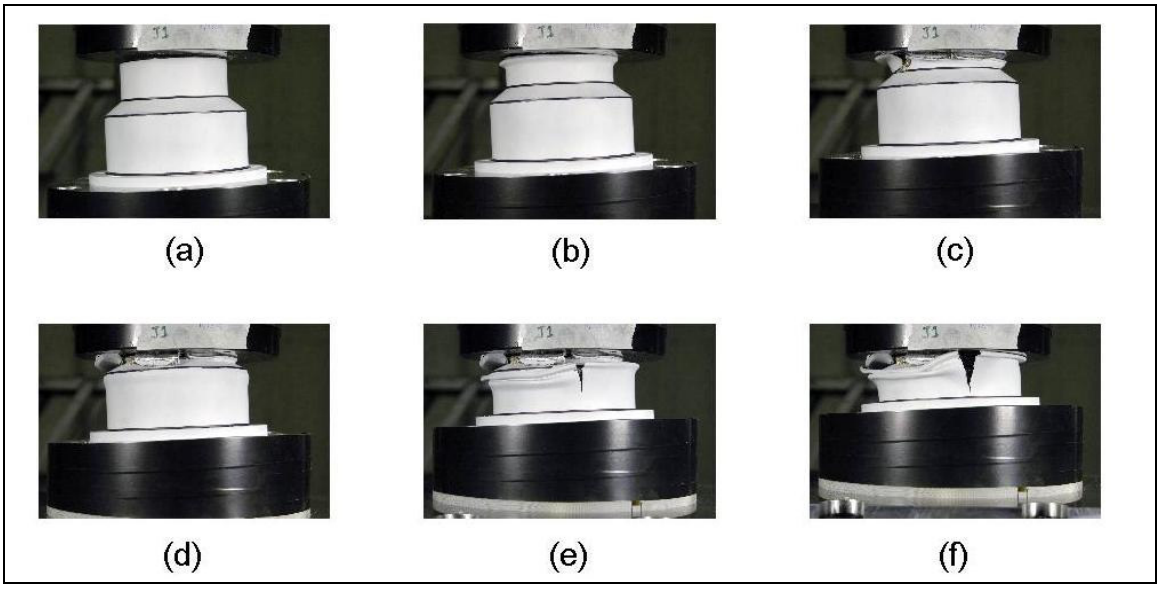

Figure 7-12. Quasi-static crush of two-layer test structure (Sample J1).

The force data in Figure 7-11 and test photos of Figure 7-12(a-f) can be used together to describe the process of how the honeycomb structure crushes under load. As deformation begins (a), the structure experiences a fairly linear load-up range, due to the combined elastic/partially plastic

properties of the segmented honeycomb disk and outer aluminum shell. Once the structure has been displaced approximately 0.2 in., the top layer of the test structure is totally engaged (b), reaches its yield strength, and begins to crush, as indicated by the first force plateau (c). At 1 in. of displacement, a second load-up range occurs (d). At this point, the upper honeycomb segment and shell have been crushed fully and can no longer yield. A second yield strength is reached at approximately 1.2 in. of displacement, indicating full engagement of the bottommost layers of the test structure (c). A second force plateau then occurs as this bottom layer is crushed (f). The jagged randomness of the two force plateaus is a result of the plastic buckling of both the honeycomb and the confining cylindrical shell. Once 2 in. of displacement were reached, the experiment was concluded.

The force versus deformation results for the Series J (3° AoA) quasi-static tests exhibit elastic-plastic ranges, yield strengths, and force plateaus—all indicating the process of honeycomb crush. When viewing the test data for a 20° AoA configuration, the same characteristics are present, but are not as well defined due to the increased angle of the applied force. In addition, the 20° AoA configurations were not tested to a full 2 in. of displacement, because at that displacement the top load frame platen would come into contact with the AoA block. This decreased maximum displacement prevents the second force plateaus from occurring in the 20° AoA configurations due to the bottom layer of honeycomb not approaching its ultimate yield strength. The force versus displacement data for test Series K (20° AoA) is shown in Figure 7-13 with the corresponding crush photos in Figure 7-14. The remaining configuration quasi-static test data are shown in the section titled Quasi-static Force and Energy.

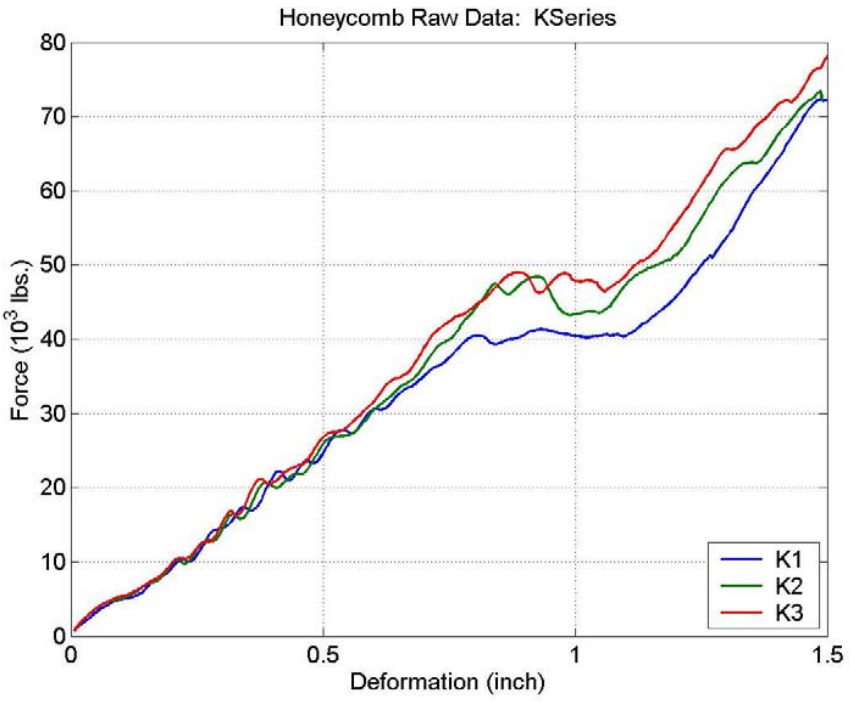

Figure 7-13. Crush force versus displacement (Series K).

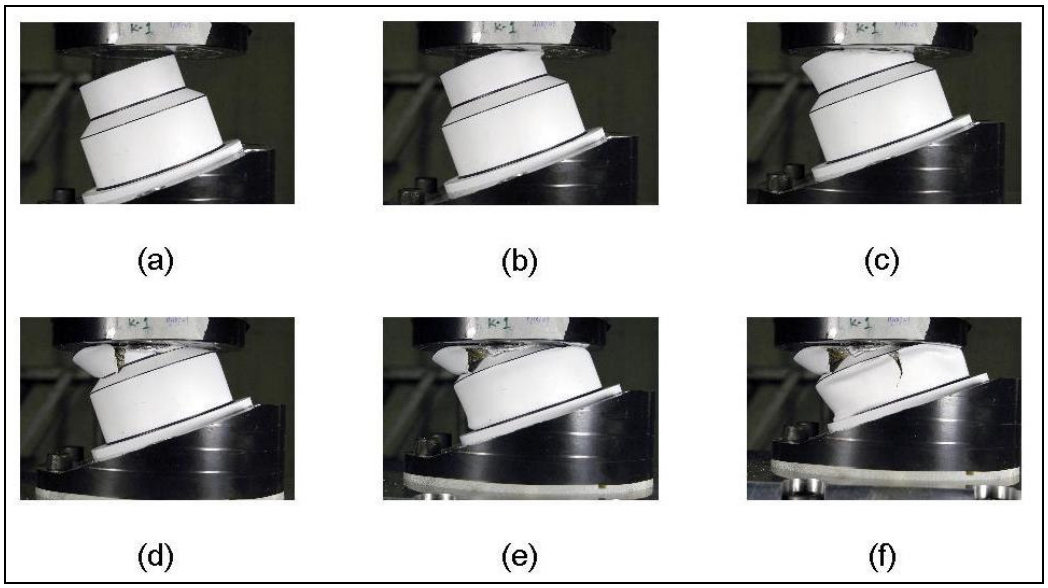

Figure 7-14. Quasi-static crush of two-layer test structure (Sample K1).

Again, using force data in Figure 7-13 in conjunction with the test photos in Figure 7-14(a-f) for a 20° AoA, the process of honeycomb structure crush can be described. At the very beginning of crush, from 0 in. of deformation to approximately 0.1 in., a load-up region exists due to the force being applied only at the point of contact with the honeycomb structure (a). Once full contact occurs (b,c), an almost linear elastic/partially plastic range exists until 0.8 in. of deformation. A very short force plateau exists for deformations up to approximately 1.1 in. (d). The bottom of the honeycomb structure is then crushed (e), as indicated by the second elastic/partially plastic range, until the deformation data concludes at 1.5 in. The applied force did not come into full contact with the bottom layer of the honeycomb structure before the test ended (f), resulting in no second force plateau.

Using the measured force versus deformation data, the amount of energy absorbed by the honeycomb structure during crush can be calculated to obtain the desired validation metrics. To calculate the energy, the force curve was integrated numerically, using Equation 7-1, where E is absorbed energy, F is the applied force, and x is the deformation. The energy calculated from the force data for all three test samples in Series J is shown in Figure 7-15. The units of energy are in.-lb.

$$E(x) = \int_0^x F(s)ds \cong \sum_{s_1=0}^{s-x} F(s)\Delta s \qquad \text{(Eq. 7-1)}$$

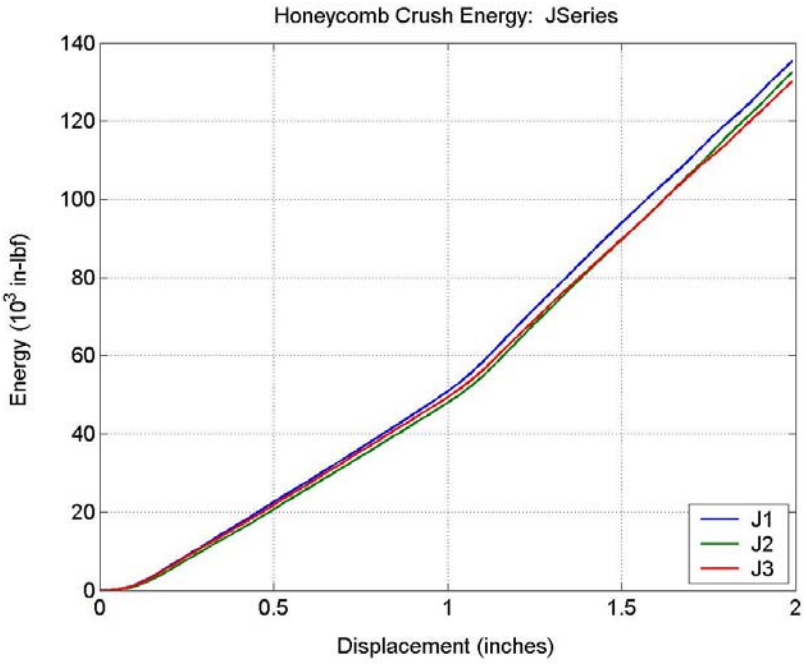

Figure 7-15. Energy versus displacement for Series J.

In examining the energy plot in Figure 7-15, two distinct slopes in the energy curves can be seen, reflecting the two force plateaus. The calculated energy data for each test sample displays less variability than the force data. In addition, the random buckling of the crushing honeycomb has been eliminated due to the integration procedure.

With the calculated energy data, the total amount of energy absorbed during the entire crush event was obtained. From this total energy, the 1/3 and 2/3 total energy values were calculated, along with their corresponding displacements. Finally, the 95 percent confidence intervals (CIs) were calculated for the energies at each displacement. This calculation accounts only for sample-to-sample variability.

The procedure for calculating the 95 percent CI for each test series first requires the assumption that the data from each series are from a normal population with unknown variance, σ. The sample mean, $\bar{x}$, and sample standard deviation, s, from three test samples (n=3) can then be calculated. For a 95 percent CI, an α-value of 0.05 is used with $t_{a/2}$ and (n-1) degrees-of-freedom to find the t-distribution value of 2.447. These values are combined in Equation 7-2 to find the estimated mean with 95 percent CI. Details for this procedure are in [5].

$$\bar{x} - t_{\frac{\alpha}{2}} \frac{s}{\sqrt{n}} < \mu < \bar{x} - t_{\frac{\alpha}{2}} \frac{s}{\sqrt{n}} \qquad \text{(Eq. 7-2)}$$

As mentioned previously, the 1/3, 2/3, and 3/3 energy values were selected for validation purposes. Validation energies with a 95 percent CI, accounting for sample-to-sample variability only, for the Series J configuration are shown in Figure 7-16. The dashed lines represent the

energy curves calculated from each test sample. The legend displays values of the 1/3, 2/3, and 3/3 energies (in.-lbs) and their corresponding displacements (in.).

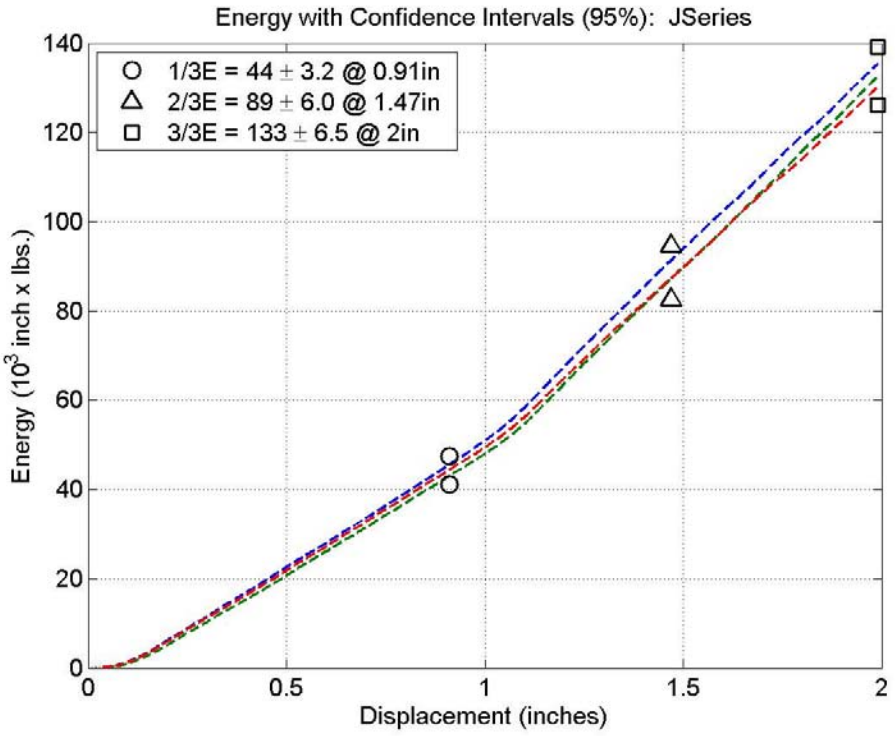

Figure 7-16. 1/3, 2/3, 3/3 energy levels with 95 percent CI (sample variability).

The energy plot in Figure 7-16 indicates that at 0.91 in. of deformation, the amount of energy absorbed by the honeycomb structure is $44 \times 10^3 \pm 3.2$ in.-lb (1/3 of total energy). At 1.47 in. of deformation, the amount of energy absorbed is 89.5 ± 6.0 in.-lbs (2/3 total energy), and at the maximum deformation of 2 in., 133 ± 6.5 in.-lb of energy (3/3 energy) has been absorbed. Again, these uncertainty values define the 95 percent CI due only to sample variability.

Next, the measurement uncertainty in the crush energies must be addressed. For the quasi-static tests, the measurement uncertainties of both the force and displacement transducers were 1 percent. To incorporate this measurement uncertainty into the crush energy calculation, it must be noted that energy is equal to the integral of force multiplied by displacement, with the force itself being a function of displacement (Equation 7-1). Consequently, when computing the crush energy for a specific crush displacement, there are uncertainties due to the measurement of both the force and the displacement. In addition, there is an additional uncertainty in the force because it is itself a function of the uncertain displacement. Therefore, there are three uncertainties present in calculating the crush energy. Combining these uncertainties requires the use of Equation 7-3, where U_T is the total uncertainty, and U_1 through U_3 are the uncertainties for the three sources [6]. For the quasi-static tests, $U_1 = 1$ percent for the force transducer, $U_2 = 1$ percent for the displacement transducer, and $U_3 = 1$ percent for the additional uncertainty due to

the force being a function of displacement. As a result, the total measurement uncertainty for the quasi-static test was 1.7 percent.

$$U_T = \sqrt{U_1^2 + U_2^2 + U_3^2} \qquad \text{(Eq. 7-3)}$$

The validation crush energies, E, and their corresponding deformations, δ, for all test configurations are shown in Table 7-3. The E_1, E_2, and E_3 columns are the energy values at 1/3, 2/3, and 3/3 of the total energy, and the ±E% columns are the total uncertainties associated with the energy calculations. The total uncertainty values combine the sample-to-sample variability and measurement uncertainty using Equation 7-3 with only U_1 and U_2.

Table 7-3. Quasi-static test energy results.

Series	Configuration	Energy (10^3 in*lb) with 95% CI at Deformation (inch)								
		E_1	±E_1%	δ_1	E_2	±E_2%	δ_2	E_3	±E_3%	δ_3
J	3° X on L	44.3	7%	0.91	88.7	7%	1.47	132.7	5%	2.00
K	20° X on L	18.1	9%	0.84	35.5	15%	1.22	52.1	15%	1.50
L	20° + on L	21.6	7%	0.89	42.6	7%	1.31	63.7	6%	1.60
M	20° + on L (165 °F)	20.6	2%	0.88	40.9	2%	1.30	61.3	1%	1.60
W	3° X on L (165 °F)	40.7	4%	0.85	80.8	3%	1.39	121.0	3%	1.90

The most noticeable characteristic of the energy results in Table 7-3 is how the 95 percent confidence intervals for the high-temperature tests, Series M and Series W, are consistently lower than that of the other honeycomb configurations. This lack of variability is most visible in the individual force measurements for Series M and Series W as shown in the section titled Quasi-static Force and Energy. Even though the increased temperature does not decrease the strength and energy absorption of the honeycomb, as will be shown, it does seem to reduce the sample-to-sample variability in the samples. This reduction of variability agrees with the results of heated honeycomb tested in [7].

Comparing the force and energy results for the different honeycomb structure configurations is best done graphically. Figures 7-17 through 7-20 compare the force and energy results between similar test configurations, i.e., J versus K, K versus L, L versus M, etc. For simplification purposes, only the mean force and mean energy values calculated from the three samples in each configuration will be plotted.

The first comparison is between Series J and Series K, shown in Figure 7-17. The difference between the two configurations was the AoA—3º AoA for Test J and 20º AoA for Test K. The force data from Series J display two well-defined force plateaus following elastic-plastic slopes. The Series K data contain elastic-plastic ranges that exist over a much longer displacement range, with a much shorter first force plateau, and no existing second force plateau. This second force plateau does not occur in Series K due to the test ending at 1.5 in. of deformation. From the data, it can be seen that the Series J configuration is able to absorb more energy than the

Series K configuration. The 3° AoA allows the honeycomb to absorb the energy along its strong t-axis without the shearing strains involved in the 20º AoA.

The next comparison performed is between Series K and Series L, shown in Figure 7-18. The orientation of the segmented honeycomb in the top of the two-layer test structure was X for Series K, and + for Series L. Both test series were performed with an AoA of 20°. From the plotted data, the force and the calculated energy data are shown to vary little over the measured deformation range, with Series L absorbing slightly more energy than Series K. However, the conclusion can be made that the energy absorption of the honeycomb structure is independent of the honeycomb orientation inside the aluminum shell.

The final comparison made will be the effect of increasing the honeycomb material temperature from room temperature (≅ 77 °F) to 165 °F. Series L and Series M, both of which had a 20° AoA and consisted of the X on L orientation, are shown in Figure 7-19. Series L honeycomb was at room temperature, and Series M was at 165 °F. In a similar comparison, Figure 7-20 consists of Series J and Series W, both of which had a 3° AoA with a honeycomb alignment of X on L. Series J honeycomb was at room temperature, and Series W was at 165 °F. Previous test data had shown that honeycomb at 165 °F was weaker then honeycomb at room temperature. However, from the temperature comparison plots in Figure 7-19 and Figure 7-20, increased temperature does not seem to have a large effect on the energy absorption properties of the two-layer honeycomb structure in a quasi-static test environment.

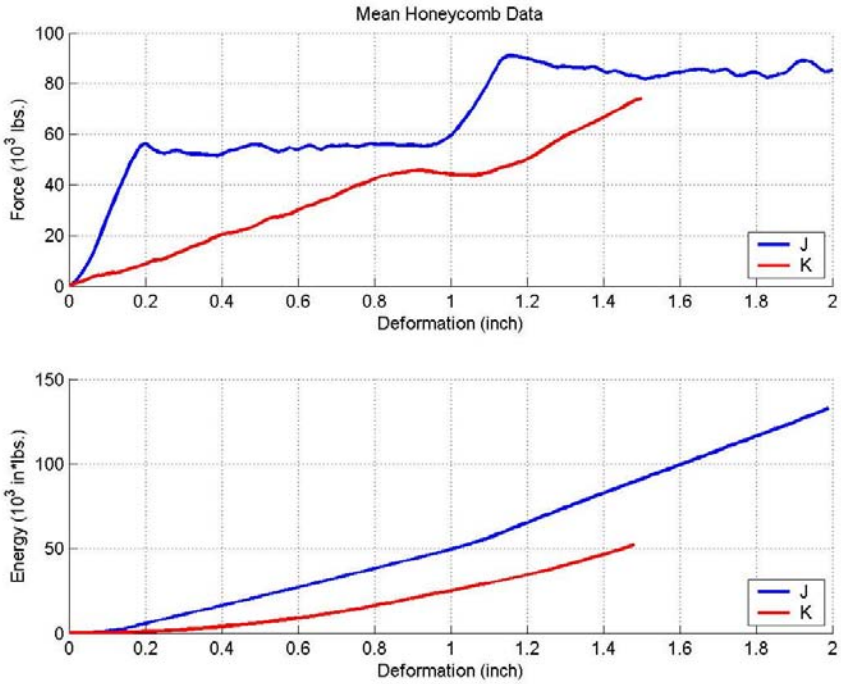

Figure 7-17. Series J (3º AoA) versus Series K (20º AoA).

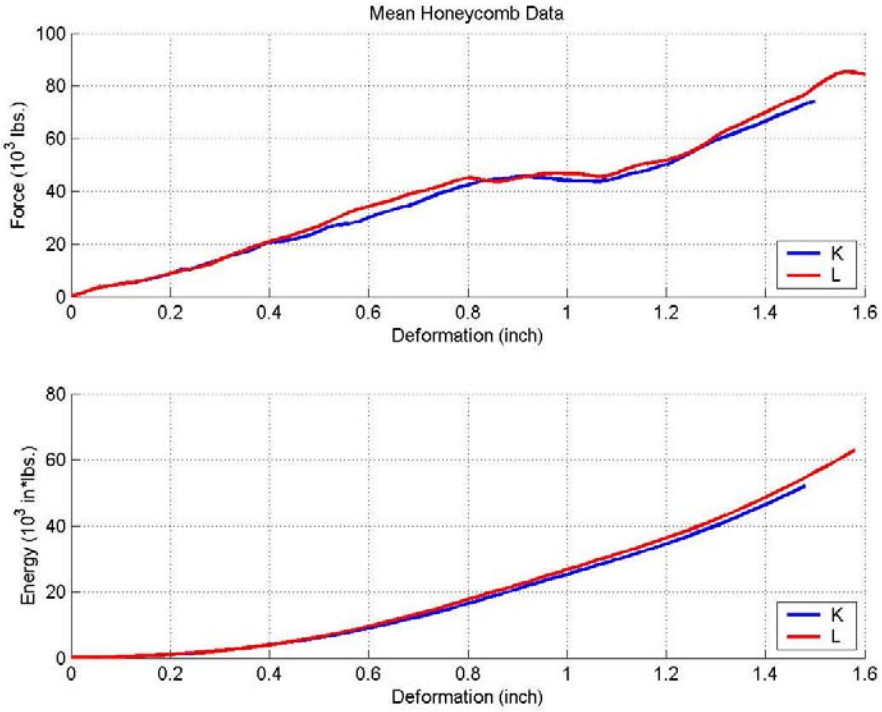

Figure 7-18. Series K (X on L) versus Series L (+ on L).

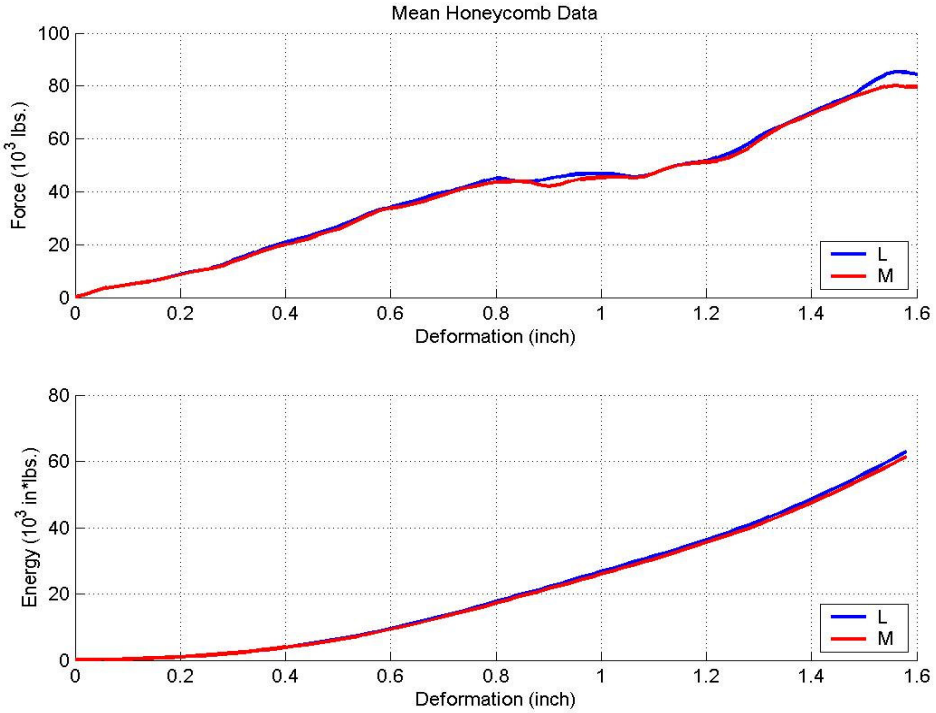

Figure 7-19. Series L (77 ºF) versus Series M (165 ºF).

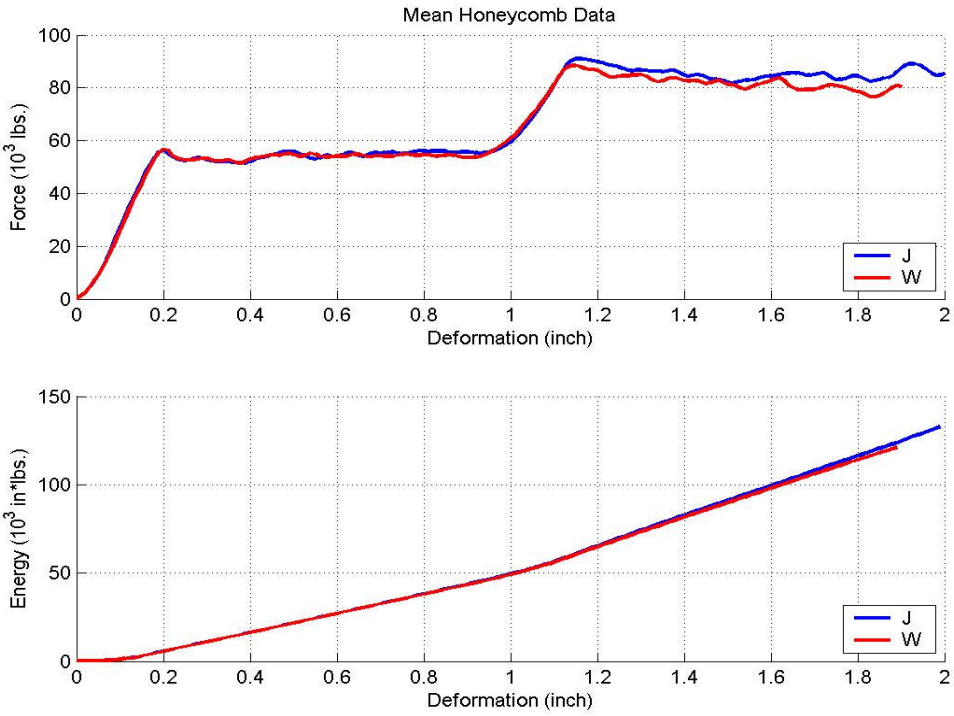

Figure 7-20. Series J (77 ºF) versus Series W (165 ºF).

The quasi-static tests performed on the various honeycomb structure configurations provided useful knowledge of the honeycomb deformations in the two-layer structure. The slow speed of the quasi-static tests allowed for accurate testing and data analysis of the honeycomb crush. However, to validate the model for dynamic strains, crushing the honeycomb at higher velocities was required.

Dynamic Testing

As with the static testing, the purpose of dynamically testing the honeycomb material was to measure force as a function of displacement for the two-layer test structure. However, as the name implies, dynamic testing requires much higher impact speeds than the quasi-static tests—speeds ranging from 60 – 85 ft/sec. These larger crush velocities, listed as a criterion in the validation space, would allow for a validation of the analytic model for dynamic strains. The dynamic test matrix used for validation is reprinted in Table 7-4.

Table 7-4. Dynamic test matrix.

Series	Configuration	Temp.	Units
R	3° X on L	T_o	3
S	3° X on L	165 °F	3
T	20° X on L	T_o	3
U	20° X on L	165 °F	3

Because a typical load-frame cannot reach the dynamic crush velocity required by the validation space, the use of a Sandia high-speed test facility, referred to as the horizontal actuator, was required. The horizontal actuator is a pneumatically actuated, high-speed, 12-in.-diameter piston that is used to propel sleds or test items along a 70-foot-long horizontal track. The piston is capable of producing up to 250,000 lb of force, resulting in sled speeds of up to 200 ft/sec [8].

To crush the honeycomb test structure on the horizontal actuator, an 8,000-lb inertial mass was situated near the end of the track. The honeycomb test structure, secured into the load-cell fixture, was attached vertically onto the inertial mass and between the rails of the track. When the piston fired, an instrumented sled weighing 107 lb glided down the track and collided into the honeycomb test structure at a measured impact velocity. The impacting sled crushed the honeycomb and then rebounded. A diagram of the horizontal actuator (as seen from above) with the assigned coordinate system is in Figure 7-21.

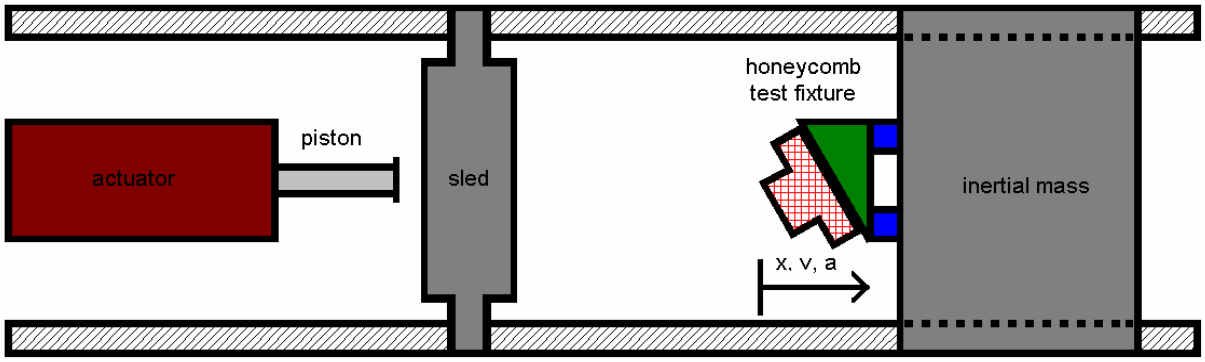

Figure 7-21. Diagram of horizontal actuator/sled track (top view).

The major instrumentation of the horizontal actuator consisted of load cells and accelerometers. The load cells used to measure the crush force were already implemented into the test fixture that secured the AoA block and honeycomb structure. Endevco 7270A accelerometers were attached to the inertial mass and sled — two on the mass and five on the sled. Both sled accelerometers and four of the seismic mass accelerometers were aligned with the X direction of the track in order to measure the axial accelerations of the honeycomb crush. The remaining seismic mass accelerometer was aligned orthogonal to the X direction in order to measure lateral acceleration of the honeycomb crush. The instrumented sled with the pneumatic piston is shown in Figure 7-22, and the top view of the inertial mass with an attached honeycomb structure is shown in Figure 7-23.

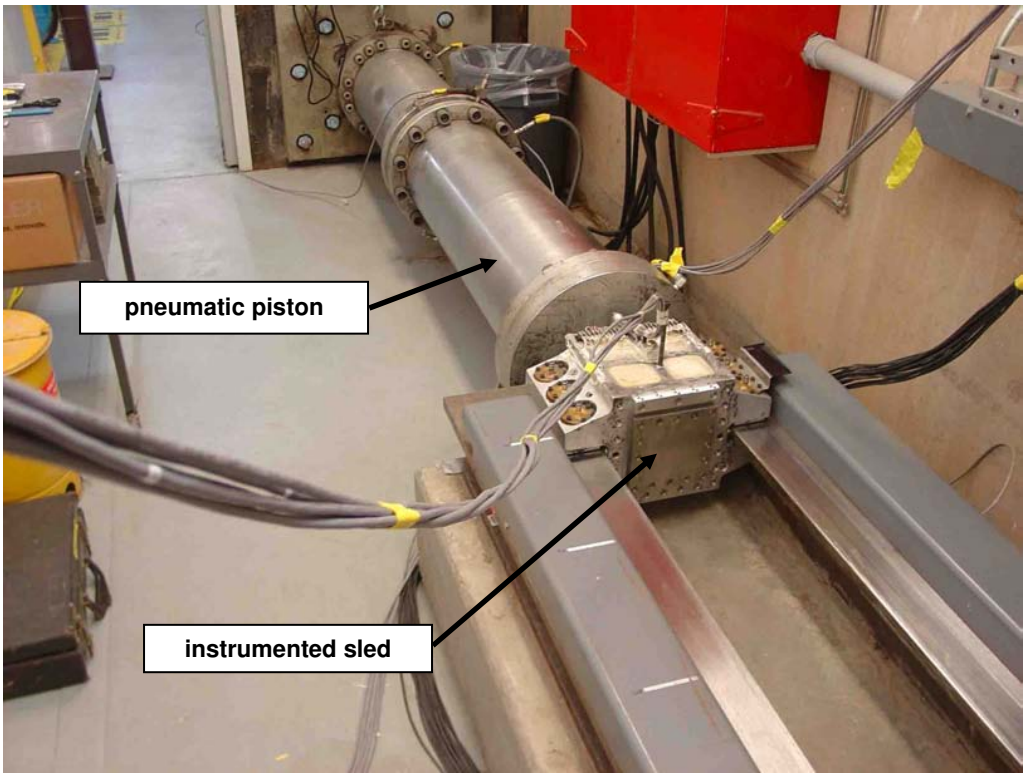

Figure 7-22. Pneumatic piston with instrumented sled.

Collection of the force and acceleration data was performed using two separate data acquisition systems. Because of the limited number of honeycomb test samples and the importance of the data, this redundancy was desired. The main data acquisition system was a PC-based system, and was referred to as the IDEAS system. The backup data acquisition system, referred to as the MIDAS system, was provided by Sandia Tech Area III personnel. The IDEAS and MIDAS acquired data at 32,768 samples/second and 500,000 samples/second, respectively.

In order to obtain an independent measurement of the crush event, a photometric system was included as part of the test instrumentation. This system comprised of a CCD (charge-coupled device) camera, capable of capturing images at 15,000 frames per second. In addition to the camera, rows of butterfly fiducials (black and white circles) were applied to the sled and to the inertial mass. These inertial mass fiducials are in Figure 7-23, above the honeycomb structure. Using distances measured before testing, the separation distance between the fiducials of the sled and mass can be calculated from the captured images. The photometric separation distance, also known as the crush distance, was compared to the results from the accelerometer data and used as a measure of the uncertainty present in the dynamic test data.

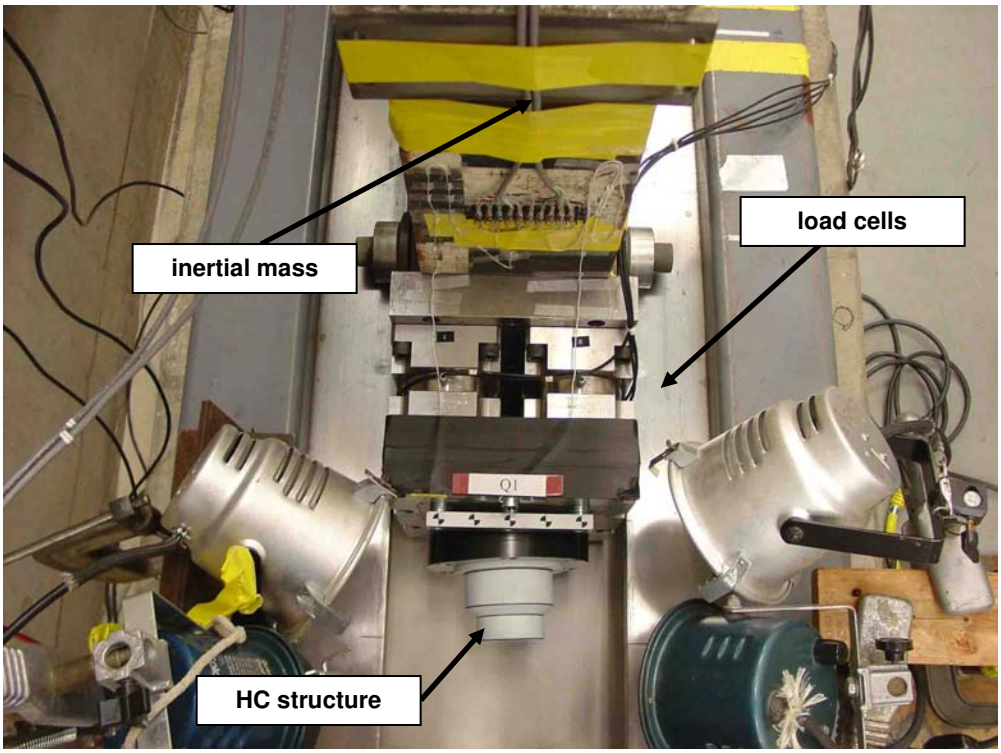

Figure 7-23. Inertial mass with assembled honeycomb test structure.

The most essential measurement obtained for each of the dynamic tests was the impact velocity of the sled. This impact velocity was required as an initial condition in the crush velocity calculation—performed by integrating the accelerometer data. To obtain the impact velocity, a three break-wire system was set up on the track, located just ahead of the honeycomb structure. When the sled broke the three wires, an attached timer recorded the time between the breaks, resulting in an estimation of the impact velocity.

In addition to the break-wire system, the previously mentioned photometric system was also used to estimate the impact velocity. The photometric impact velocities served as a useful check to the break-wire method and agreed quite well, with the maximum difference being only 1.7 percent. Consequently, the three break-wire impact velocity was used in the dynamic data analysis for the calculation of velocity and displacement. The impact velocities from both methods are listed in Table 7-5. The percent difference between the two methods is listed as well.

Table 7-5. Measured impact velocities.

Sample	Impact Velocity (ft/sec)		Difference %
	3 break-wire	photometric	
R1	85.5	84.96	0.6%
R2	85.4	84.52	1.0%
R3	85.2	84.55	0.8%
S1	85.2	84.60	0.7%
S2	85.0	84.37	0.7%
S3	85.2	84.52	0.8%
T1	68.5	67.93	0.8%
T2	68.8	67.63	1.7%
T3	69.2	69.09	0.2%
U1	69.2	68.20	1.4%
U2	9.0	69.11	-0.2%
U3	69.5	68.85	0.9%

The procedure used to analyze the force and acceleration data and compute the force versus crush is discussed below. Once the force and crush values were obtained, the energy was easily calculated using the same procedure as detailed in the quasi-static test section. Data used in the dynamic analysis were collected with the IDEAS data acquisition system. A comparison between these data and both the MIDAS and photometric data was made and is discussed as well. Only data from test Series R are shown in detail in the following analysis procedure. The data and intermediate analysis for the remaining test series (Series S, T, and U) is located in the section titled Dynamic Force and Energy Data.

Before interpreting the data analysis, the coordinate system used in the dynamic test setup must be addressed. In the test, the origin of the coordinate system was defined as the point of first contact between the sled and the honeycomb test structure, as illustrated in the diagram of the horizontal actuator (Figure 7-21). The positive direction of the coordinate system's x-axis was defined as the direction of the sled travel. Finally, time equals zero ($t = 0$) was defined as the instant of impact between the sled and test structure. These designations are essential in the explanation of the acceleration, velocity, and displacement results.

The term *crush* must be addressed as well. *Crush* was defined as the difference of the sled data from the inertial mass data. This term can be applied to all measured and calculated records—acceleration, velocity, or displacement. The crush values must be positive, occurring when the sled data are greater than the mass data. If this statement becomes untrue, then the crush event has ended.

The raw force and acceleration data for test Series R, Sample 1 (designated as R1) are in Figure 7-24 and Figure 7-25, respectively. The force data are in units of pounds (lbf), acceleration in units of inches per second squared (in./sec^2), and time in milliseconds (msec). The acceleration signals have been averaged for both the sled and the inertial mass, and the crush acceleration is plotted as well. The data shown include data collected before and after the crush event. The actual crush event lasts for approximately 3.5 msec.

The most noticeable characteristic in both force and acceleration data is the oscillatory response that occurs after impact. To investigate whether this was a resonance of the load-cell fixture or real data caused by the crushing of the honeycomb material, a frequency analysis was performed. The frequencies from three signals were analyzed: the signal during the crush event, the signal immediately following the crush event, and a response signal from a direct impact excitation to the force fixture with an attached test structure. The resulting analysis showed that frequencies present during the crush event (time from 0 to 3.5 msec) are not seen in the resonance frequencies of the plate. In addition, the frequencies found after the crush event were identical to the frequencies found from the direct impact response. Therefore, the measured response during the crush event is due to the buckling of the honeycomb material, and can be considered valid data. The acceleration data also illustrate the dynamic response of the sled and inertial mass when impact occurs. At impact, the sled experiences a deceleration while the inertial mass experiences acceleration.

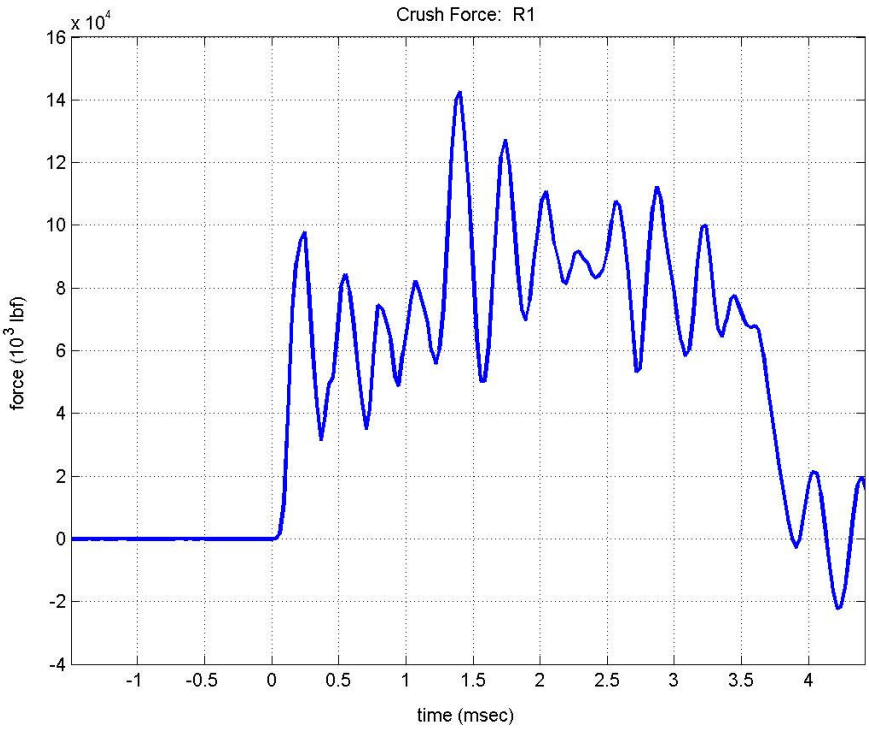

Figure 7-24. Force versus time for Sample R1.

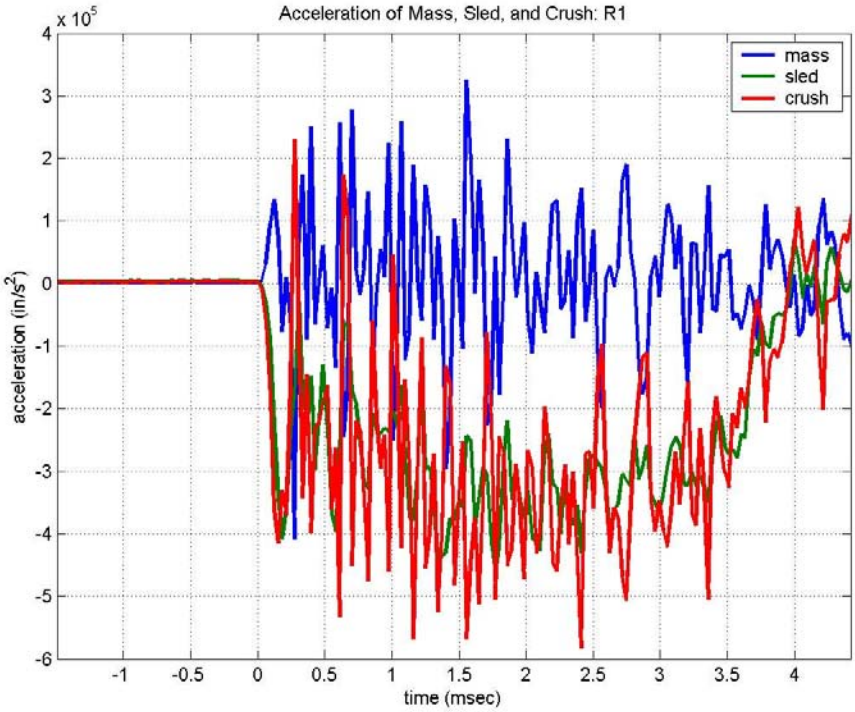

Figure 7-25. Acceleration versus time for Sample R1.

The first step in the data processing involves calculating velocity from the acceleration as a function of time, using numerical integration. To calculate the velocity, Equation 7-4 was used, where v is the velocity, v_o is the impact velocity of the sled, a is the acceleration signal, and t is the time. In order to calculate the sled velocity correctly, the impact velocity of the sled is required as the initial condition. The impact velocity value used in the data analysis was the three break-wire velocity. The calculated sled velocity, inertial mass velocity, and crush velocity for sample R1, in units of in./sec, are in Figure 7-26.

$$v(t) = \int_0^t a(\tau)d\tau + v_o \cong \sum_{s_i=0}^{s=t} a(\tau_i)\Delta\tau + v_o \qquad \text{(Eq. 7-4)}$$

As shown in the plot, at time before the event, the velocity of the sled is 1026 in./sec (85.5 ft/sec), and the velocity of the inertial mass is zero. Once impact occurs at $t = 0$, the sled velocity drops dramatically as the inertial mass velocity increases slightly. The crush velocity, the difference between the sled and inertial mass velocities, decreases dramatically as well. The plotted data can be used to extract the total time of the crush event. Once the sled velocity has decreased to that of the inertial mass velocity, the crushing of the honeycomb ceases, and the sled begins to rebound. The signs and directions of the velocities serve as a good check of the calculated data.

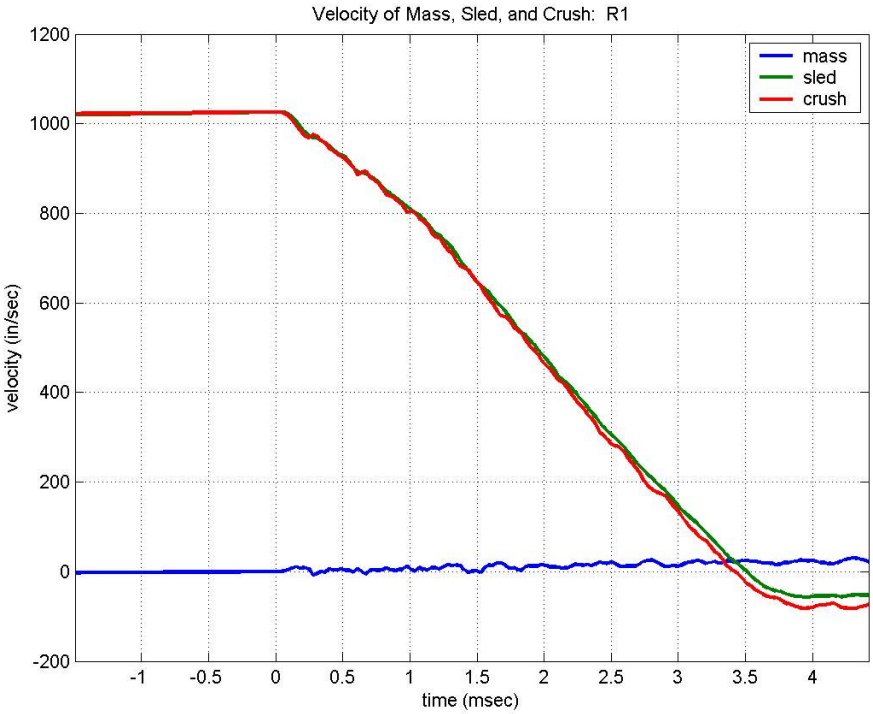

Figure 7-26. Velocity versus time for Sample R1.

The next step to determine the displacement from the measured data requires numerically integrating the calculated velocity as a function of time. To calculate the displacement, Equation 7-5 was used, where x is the displacement, v is the previously calculated velocity, and t is the time. The initial displacement conditions of both the sled and the inertial mass are zero at the time of impact ($t = 0$). The calculated sled displacement, inertial mass displacement, and crush displacement for sample R1, in units of inches, are in Figure 7-27.

$$x(t) = \int_{o}^{t} v(\tau)d\tau \cong \sum_{t_i=0}^{t_i=t} v(t_i)\Delta t \qquad \text{(Eq. 7-5)}$$

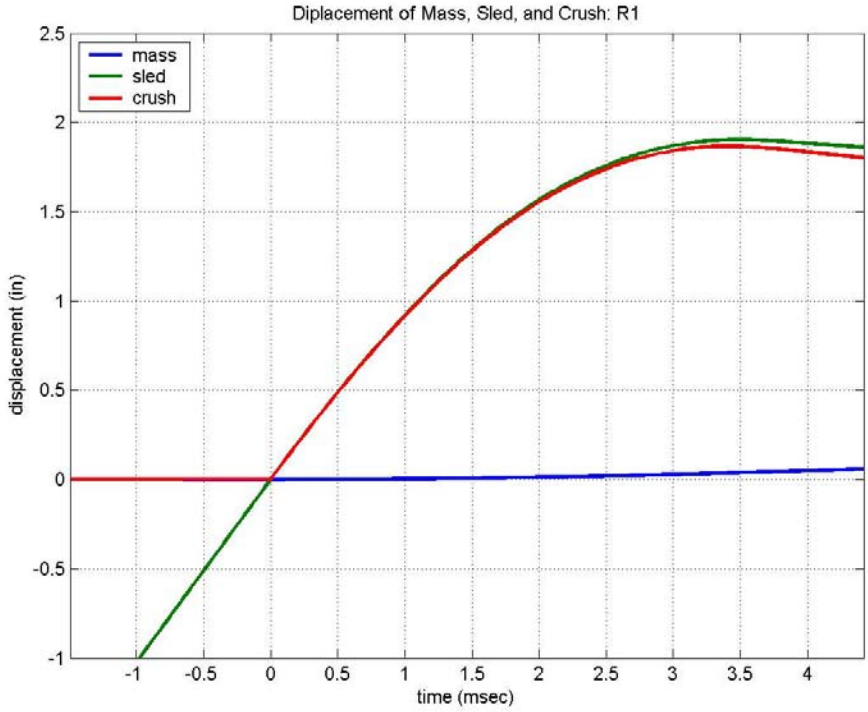

Figure 7-27. Displacement versus time for Sample R1.

If the data are viewed from the beginning of the time record to the point of impact, the sled displacement increases from an initial negative displacement, while the inertial mass and crush displacements are zero. Once impact occurs, the sled and inertial mass displace positively, as expected. Because the displacement of the sled is much larger than the very small inertial mass displacement, a large crush of the honeycomb occurs—only slightly less than the sled displacement. As in the velocity data, the time period of the crush event can be observed from the calculated displacements. Here, the crush event ends at the maximum crush displacement, at approximately 3.5 msec with a crush of about 1.9 in. Data that occur after this point in time reflect the rebounding of the sled away from the honeycomb structure, and are not used in further analysis.

As mentioned previously, two data acquisition systems were used to measure displacement indirectly, and an independent method, photometrics, was used to measure displacement directly. Comparing the displacement results from the three methods provides a check of the data analysis procedures and a measure of the uncertainty in the experiment.

Plotted in Figure 7-28 is the honeycomb crush from the IDEAS, MIDAS, and photometric results, designated as PHOTO, for Sample R1. As can be seen, the MIDAS and IDEAS data overlap, as they should, because the data analysis involved integrating the same acceleration signals, even though the signals were digitized and processed by two completely separate hardware and software systems. In contrast, the photometric data show a larger crush (approximately 0.1 in. larger) and reveal the peak crush at a later point in time. Of course, the time of impact ($t = 0$) was set independently for each of the three measurement techniques.

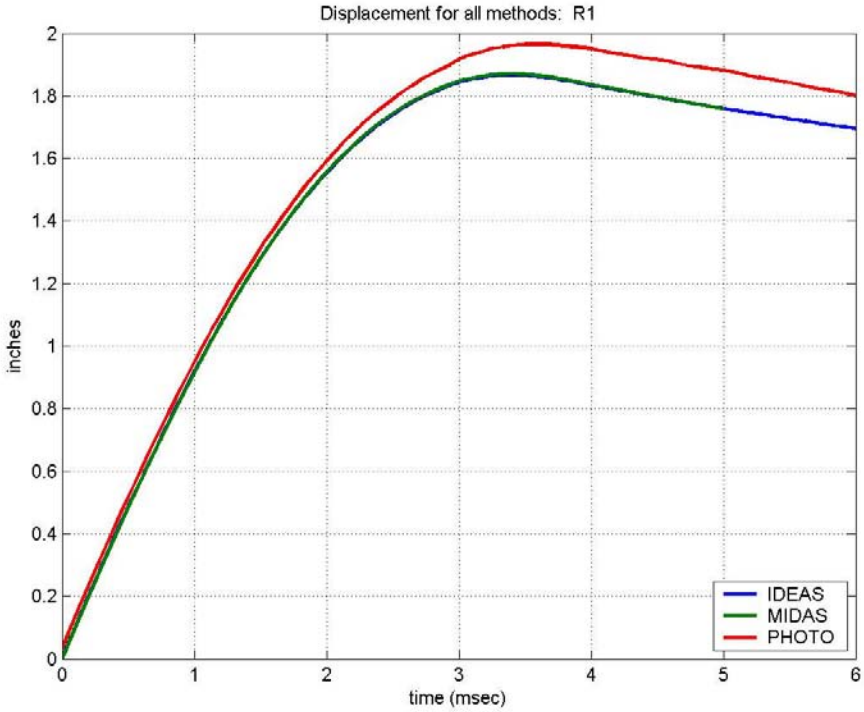

Figure 7-28. Comparison of IDEAS, MIDAS, and photometric data for Sample R1.

Although this observed difference and uncertainty is not large at all, approximately 5 percent, one would like to understand its source. One possible source is the uncertainty in the sensitivities of the accelerometers, which was 6 percent. Sensitivity uncertainty translates directly to displacement uncertainty after the double integration of the accelerometer signals.

Another source for the difference could be the independent determination of $t = 0$ for the three techniques. Because the maximum crush velocity occurs at $t = 0$, obtaining an accurate crush distance, either by integrating velocity or by direct observation, requires that the determination of the impact time must be accurate. IDEAS and MIDAS both used first observed acceleration due to impact in the accelerometer signals, while the photometrics attempted to observe impact directly. All three methods were dependent of data sample rate. MIDAS had sampled at 500,000 samples/second, IDEAS sampled at 32,768 samples/second, and the photometrics photographed at 15,000 samples/second. At 15,000 samples/second and at an impact velocity of 1000 in./sec, a single sample period represents 0.07 in. of displacement.

The measured maximum crush displacement for each of the 12 dynamic tests calculated from the IDEAS, MIDAS, and photometrics data is listed in Table 7-6. The differences between the IDEAS and the photometrics data varies from 8.8 percent to -0.6 percent. Note in particular that for the 20° AoA tests (Series T and Series U), the average difference is only 1.1 percent, much less than the 3° AoA tests, with an average difference of 6.9 percent, in which the photometrics results were always larger than the IDEAS or MIDAS. Observing first impact in the photos,

with the slower sample rate, is more difficult and more judgmental for the 3° AoA tests than for the 20° AoA tests.

Table 7-6. Maximum measured honeycomb crush.

Sample #3	AoA (deg)	Max crush			IDEAS & PHOTO % diff
		IDEAS (in)	MIDAS (in)	PHOTO (in)	
R1	3	1.87	1.87	1.97	5.26
R2	3	1.86	1.87	2.03	8.83
R3	3	1.84	n/a	1.94	5.38
S1	3	1.97	n/a	2.11	6.83
S2	3	1.97	n/a	2.12	7.87
S3	3	1.93	n/a	2.07	7.30
T1	20	1.69	1.70	1.75	3.01
T2	20	1.76	1.73	1.76	-0.31
T3	20	1.71	1.70	1.70	-0.61
U1	20	1.80	n/a	n/a	n/a
U2	20	1.82	n/a	1.85	1.96
U3	20	1.81	n/a	1.84	1.68
				Mean:	4.29

Whatever the source of the observed difference in the crush displacements, using three different techniques to measure these displacements provides confidence in this critical measured quantity for the validation, and more insight into the uncertainty. For the remainder of the data analysis and processing, only the IDEAS data were used, and the MIDAS and photometric data were used to determine uncertainty.

Once the honeycomb crush and crush force are obtained as a function of time, they can be plotted parametrically. The resultant function includes only displacement and force data that occur during the crush event, and resembles the data measured directly from the quasi-static tests. The crush force versus calculated displacement for all three samples in test Series R can be seen in Figure 7-29.

One noticeable aspect of the force data in Figure 7-29 is consistency of the data for the three samples over the length of the event, especially up to 1.6 in. of crush. The data resemble the quasi-static plot of Series J if an imaginary line were drawn through the oscillations of the data. As noted when discussing the force measurements of Series R, these oscillations are due to the dynamic buckling of the honeycomb during the dynamic event.

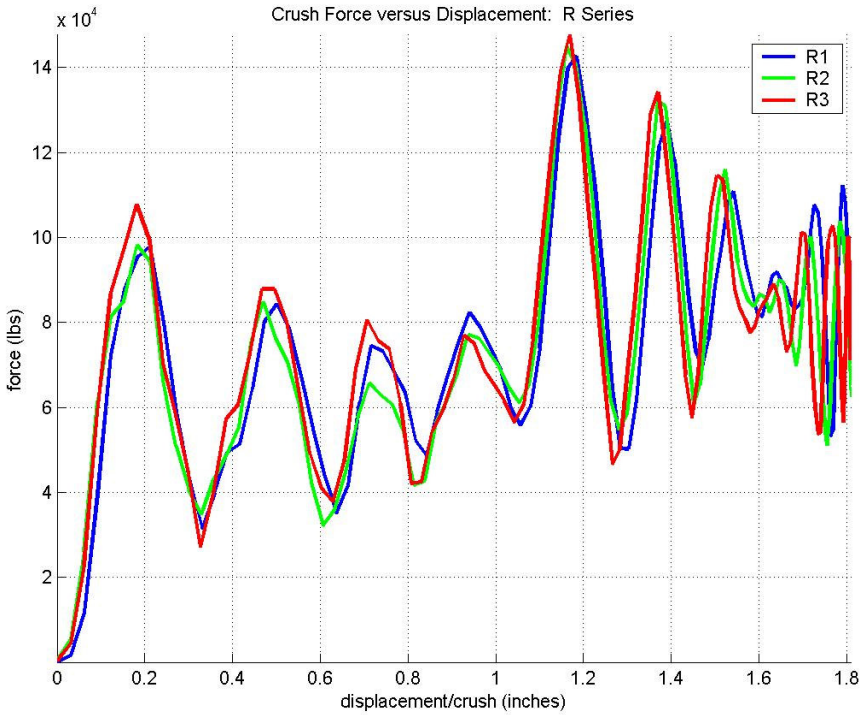

Figure 7-29. Crush force versus crush for Series R.

Now that the crush force as a function of displacement has been obtained, the crush energy absorbed by the honeycomb structure in a dynamic environment can be calculated. The procedure used to obtain the dynamic energy is the same as for the quasi-static data analysis. Following this procedure, the 1/3, 2/3, and 3/3 absorbed energies were calculated from the force data, along with their corresponding displacements. The 95 percent confidence intervals, due only to sample-to-sample variability, are shown in Figure 7-30.

The energy plot in Figure 7-30 indicates that at 0.75 in. of deformation, the amount of energy absorbed by the honeycomb structure is $44 \times 10^3 \pm 3.2$ in.-lb (1/3 of total energy). At 1.3 in. of deformation, the amount of energy absorbed is 86 ± 1.4 in.-lbs (2/3 total energy), and at the maximum deformation of 1.75 in., 127 ± 1.75 in.-lb of energy (3/3 energy) has been absorbed. Again, these uncertainty values define the 95 percent confidence interval due only to sample-to-sample variability.

The measurement uncertainty for the dynamic test was calculated using the same method as in the previously discussed quasi-static test. For the dynamic tests, the uncertainty of the force transducer remained at 1 percent. However, the transducer used to measure displacement (through double integration of the signal) was an accelerometer, with an uncertainty of 6 percent. Again, when calculating the energy, three uncertainties are present, and Equation 7-3 can be used to calculate the total measurement uncertainty. For the dynamic tests, $U_1 = 1\%$ for the force transducer, $U_2 = 6$ percent for the accelerometers, and $U_3 = 6$ percent for the additional uncertainty due to the force being a function of displacement. As a result, the total measurement uncertainty for the dynamic test was 8.5 percent.

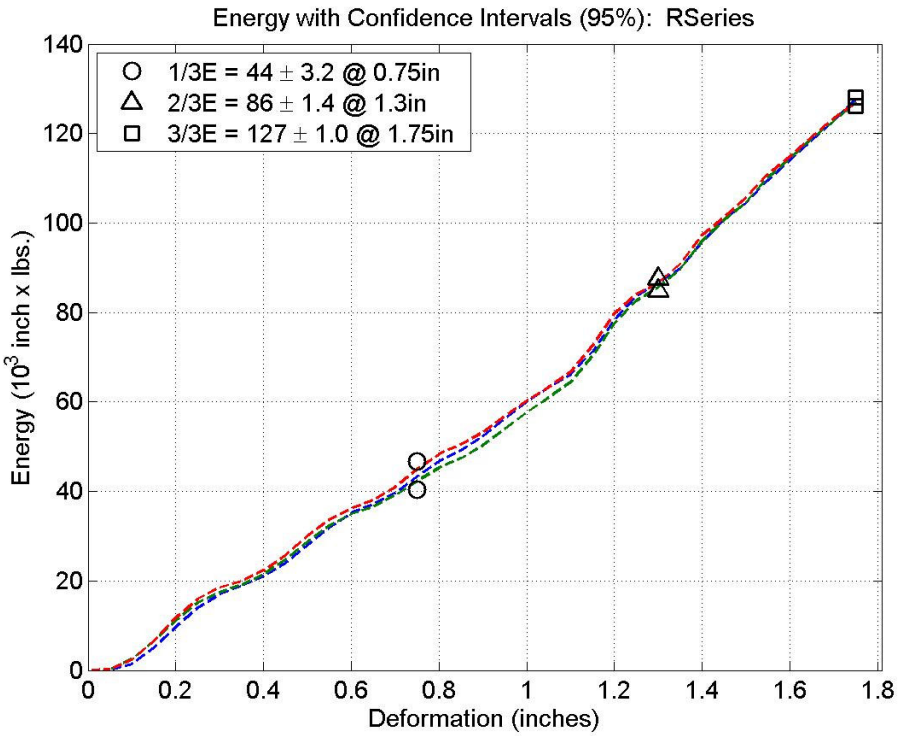

Figure 7-30. Energy for Series R with 95 percent CI (sample variability).

The validation crush energies, E, and their corresponding deformations, δ, for all dynamic test configurations are shown in Table 7-7. The E_1, E_2, and E_3 columns are the energy values at 1/3, 2/3, and 3/3 of the total energy, and the ±E% columns are the total uncertainties associated with the energy calculations. The total uncertainty values combine the sample-to-sample variability and measurement uncertainty using Equation 7-3 with only U_1 and U_2.

Table 7-7. Dynamic test energies.

Series	Configuration	Energy (10^3 in*lb) with 95% CI at Crush (inch)								
		E1	±E1%	δ1	E2	±E2%	δ2	E3	±E3%	δ3
R	3° X on L	43.50	11%	0.75	86.2	9%	1.30	127.2	9%	1.75
S	3° X on L (165 °F)	44.70	9%	0.80	85.5	9%	1.35	127.7	9%	1.90
T	20° X on L	26.2	17%	0.90	51.0	17%	1.30	75.0	13%	1.60
U	20° X on L (165 °F)	26.0	10%	0.95	52.3	9%	1.40	76.7	9%	1.70

Just as in the quasi-static analysis, comparing the dynamic force and energy results for the different honeycomb structure configurations is best done graphically. The following figures will compare the force and energy results between similar test configurations. For simplification purposes, only the mean force and mean energy values, calculated from the three samples in each configuration, will be plotted.

The first comparison is between Series R and Series T, shown in Figure 7-31. The only difference between the two configurations was the AoA—3º AoA for Series R and 20º AoA for Series T. The force data from Series R display well-defined honeycomb buckling during the deformation, due to the small AoA. Because of this smaller AoA, the Series R configuration is able to absorb more energy than the Series T configuration. The 3° AoA allows the honeycomb to absorb the energy along its strong t-axis without the shearing strains involved in the 20º AoA.

The following two comparisons will illustrate the effect of increasing the honeycomb material temperature, from room temperature to 165 °F, during a dynamic event. A comparison between Series R and Series S, both of which had a 3° AoA, is shown in Figure 7-32. Series R honeycomb was at room temperature (≅77 °F), and Series S was at 165 °F. In a similar comparison, Figure 7-33 consists of Series T and Series U, both of which had a 20° AoA. Series T honeycomb was at room temperature (≅77 °F), and Series U was at 165 °F. Previous test data had shown that honeycomb at 165 °F was weaker than honeycomb at room temperature. The temperature comparison plots in Figure 7-32 and Figure 7-33 indicate that this weakening of the honeycomb exists, but to a small extent, in a dynamic environment. The weakening is more evident in the 20° AoA configuration than the 3° AoA.

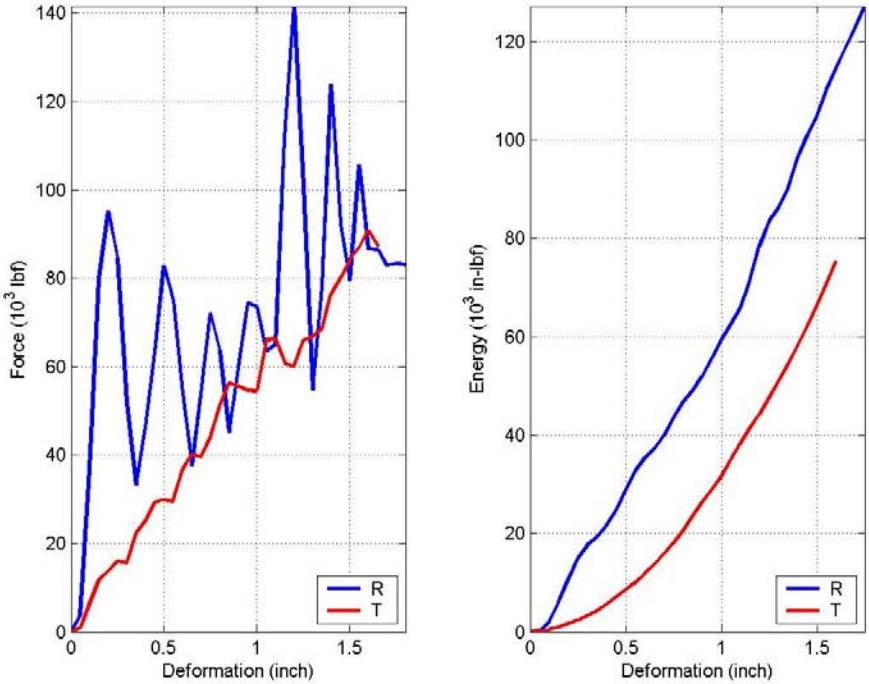

Figure 7-31. Series R (3º AoA) versus Series T (20º AoA).

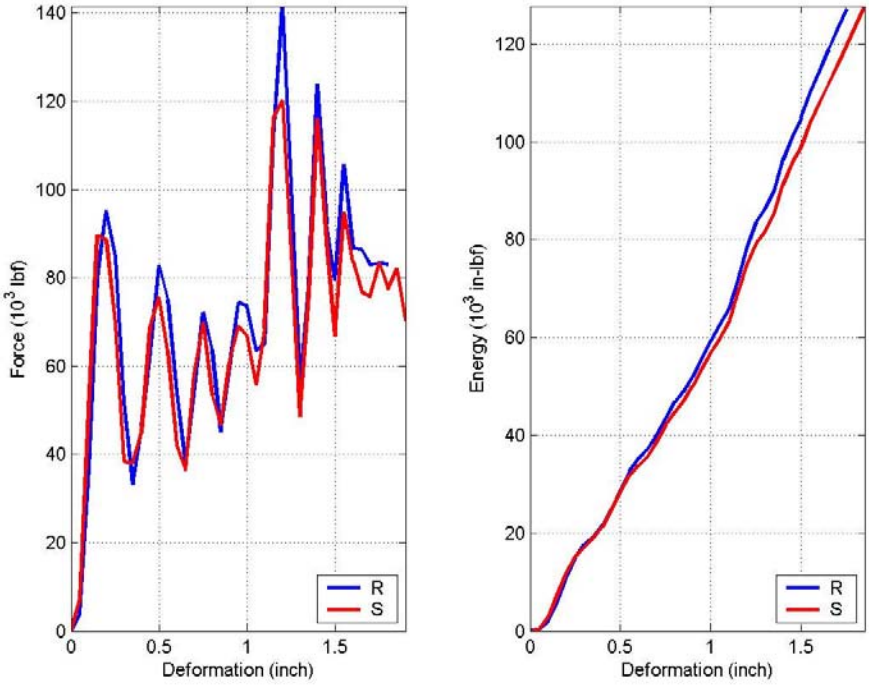

Figure 7-32. Series R (77 ºF) versus Series S (165 ºF), 3° AoA.

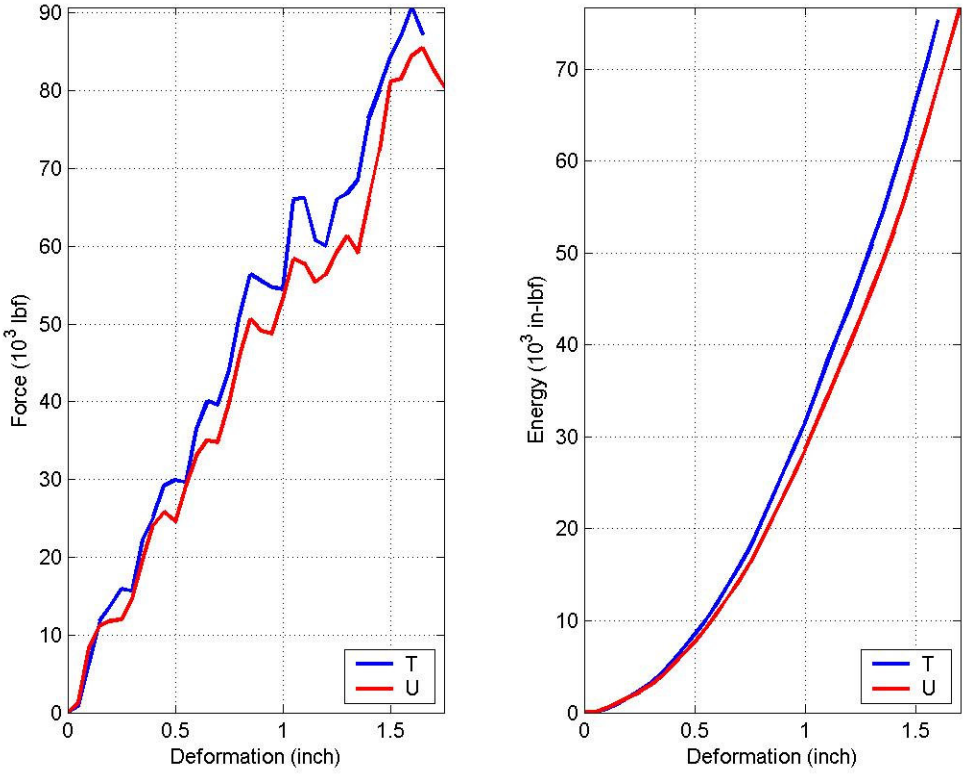

Figure 7-33. Series T (77 ºF) versus Series U (165 ºF), 20° AoA.

Crushing the honeycomb structures dynamically provided validation experiments which samples the validation space, including dynamic strain, confinement, off-axis loading, and high and moderate temperatures. The results of these dynamic tests will be used to validate the analytical model.

Quasi-Static versus Dynamic

To compare the honeycomb crush for quasi-static and dynamic crush tests, similar configurations for both environments will be evaluated together. The first comparison will be Series J and Series R; both have 3°AoA and were tested at room temperature. The force is plotted in Figure 7-34 and the energy in Figure 7-35. When viewing the static and dynamic force together, it seems that the static data move along the average of the dynamic data. However, the energy plot illustrates that the dynamic test absorbed more energy because of the increased crush strength of the honeycomb, which was due to the dynamic strains.

The next comparison will be Series K and Series T; both have 20° AoA and were tested at room temperature. The force is plotted in Figure 7-36, the energy in Figure 7-37. The force data for the dynamic test Series T are slightly larger in magnitude than the quasi-static test Series K for the deformation measured. Consequently, the dynamic data show a larger absorption of energy than the quasi-static, again because of the dynamic strains experienced by the honeycomb.

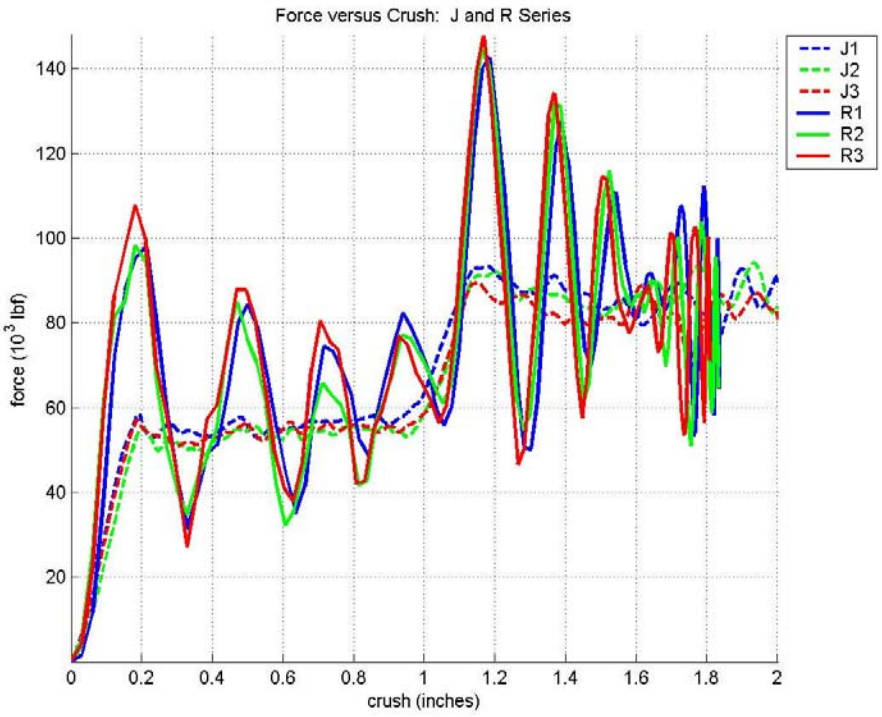

Figure 7-34. Force of Series J and Series R.

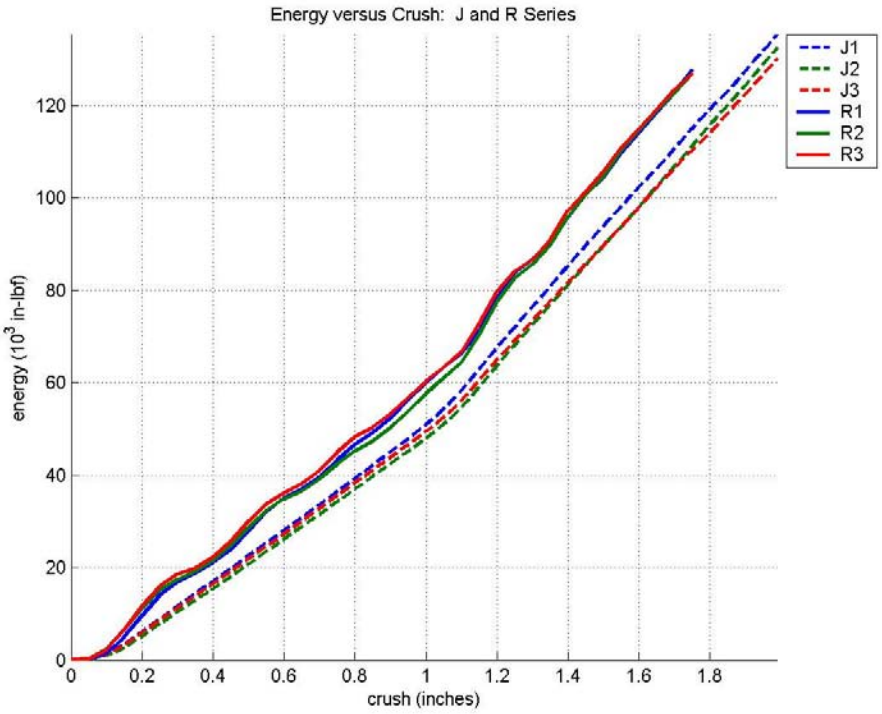

Figure 7-35. Energy of Series J and Series R.

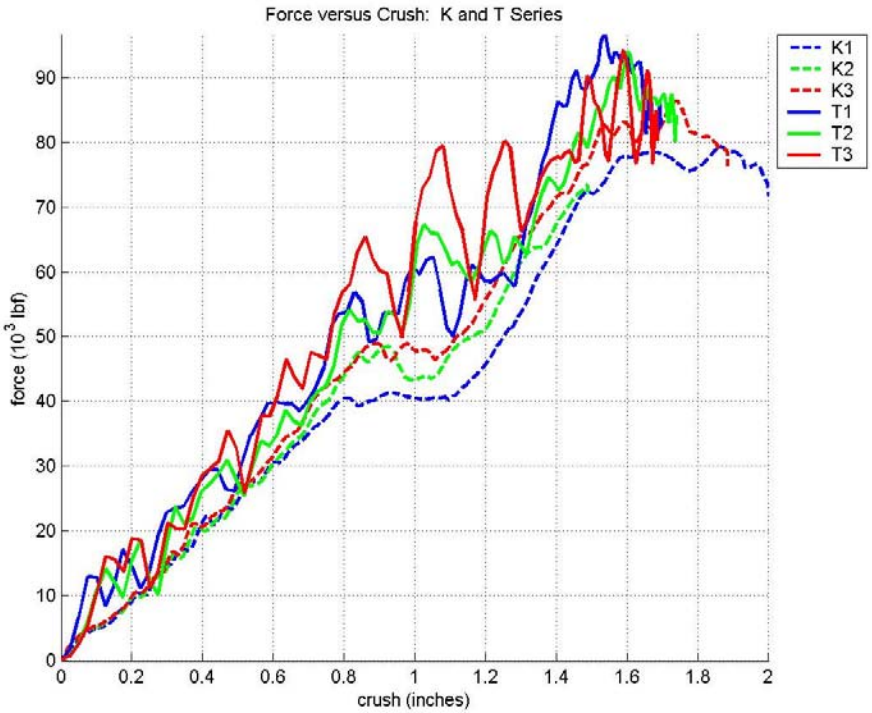

Figure 7-36. Force of Series K and Series T.

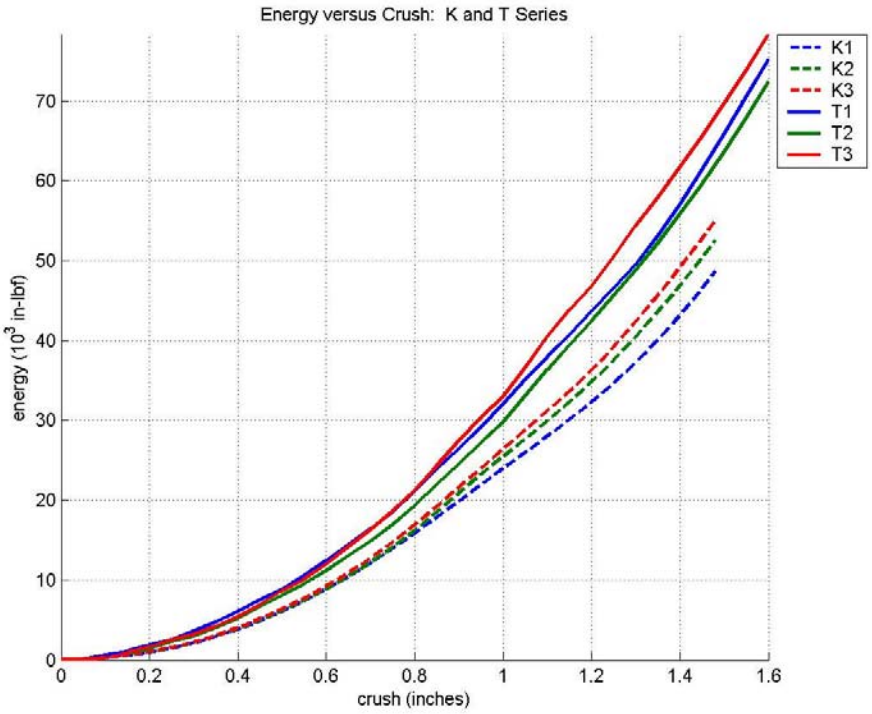

Figure 7-37. Energy of Series K and Series T.

Quasi-static Force and Energy

The measured force and calculated energy versus deformation data for quasi-static test Series K, L, M, and W are plotted in Figures 7-38 through 7-45. In the energy figures, the colors of the dashed lines correspond to the colors used for each sample in the preceding force figure. The legend of the energy figures displays values of the 1/3, 2/3, and 3/3 validation energies and their corresponding displacements (inches). The 95 percent uncertainty values listed in the legend represents sample-to-sample variability for each configuration. The test names, configurations, and figure numbers are listed in Table 7-8. Test Series J has already been shown in detail in the quasi-static section of this report.

Table 7-8. Quasi-static test figure listing.

Test Names	Configuration	Temp.	Force	Energy
K1, 2, 3	20° X on L	To	Figure 7-38	Figure 7-39
L1, 2, 3	20° + on L	To	Figure 7-40	Figure 7-41
M1, 2, 3	20° + on L	165 °F	Figure 7-42	Figure 7-43
W1, 2, 3	3° X on L	165 °F	Figure 7-44	Figure 7-45

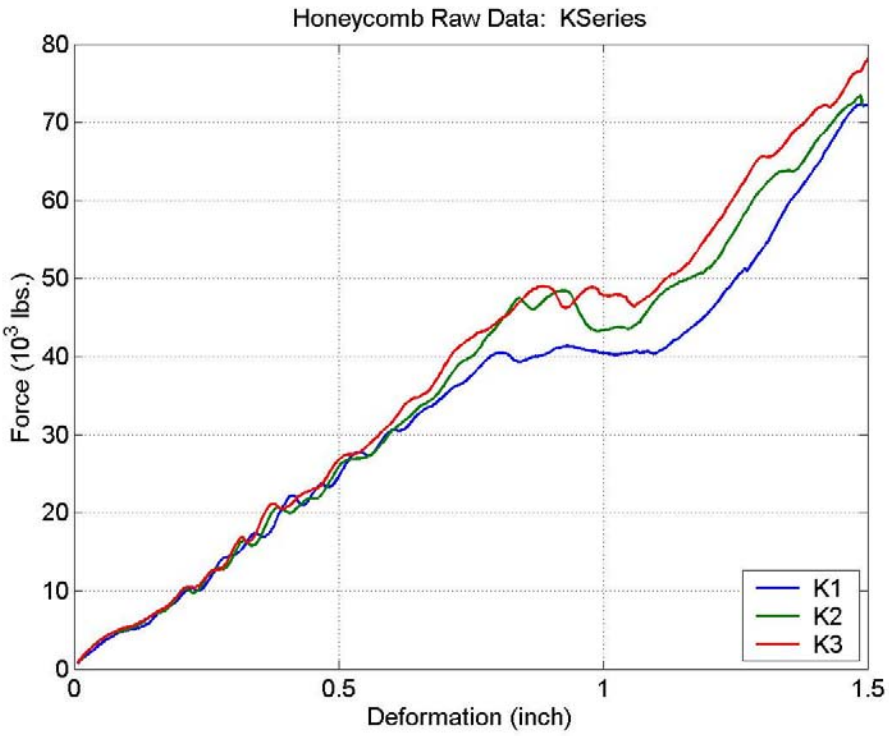

Figure 7-38. Crush force (Series K).

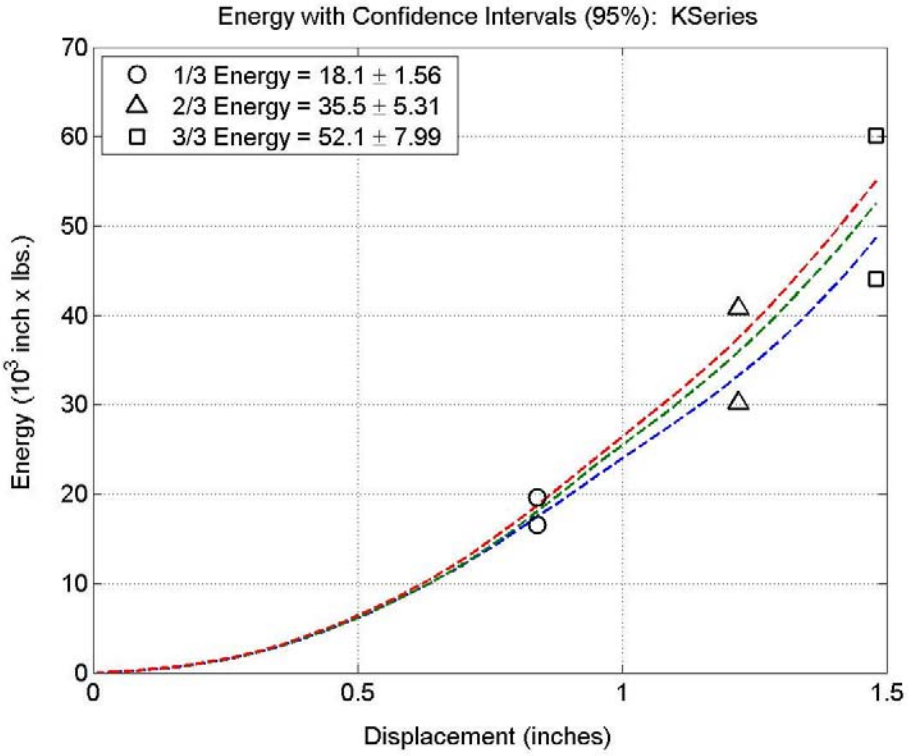

Figure 7-39. Crush energy (Series K).

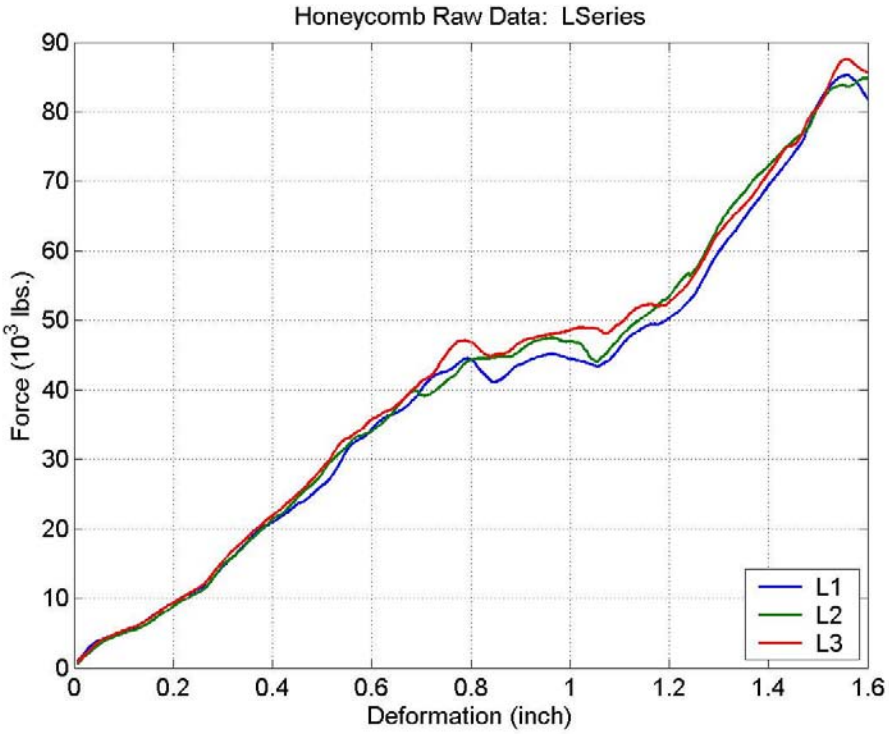

Figure 7-40. Crush force (Series L).

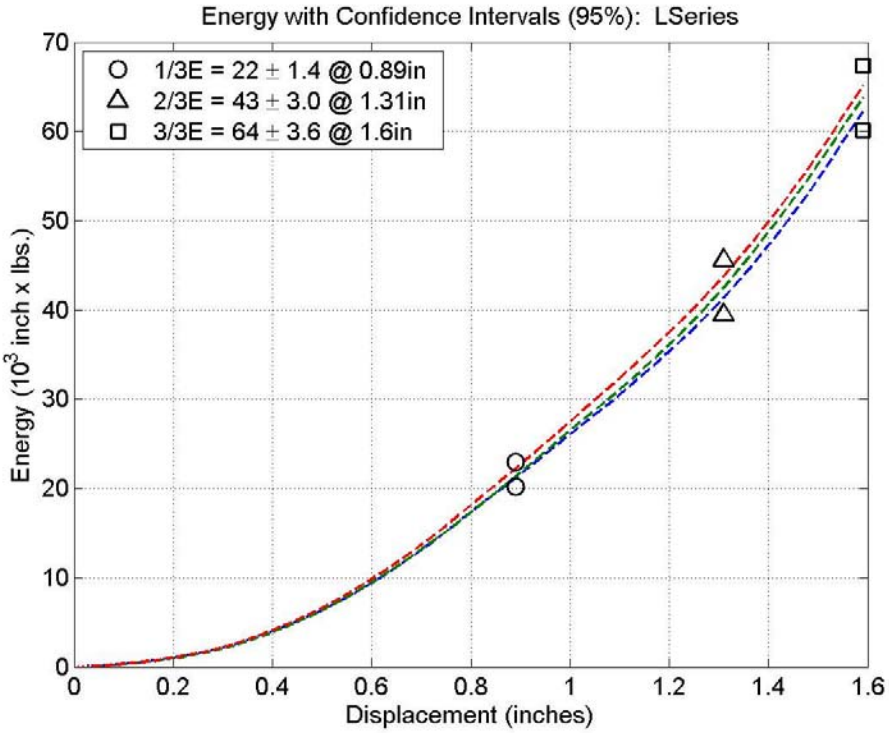

Figure 7-41. Crush energy (Series L).

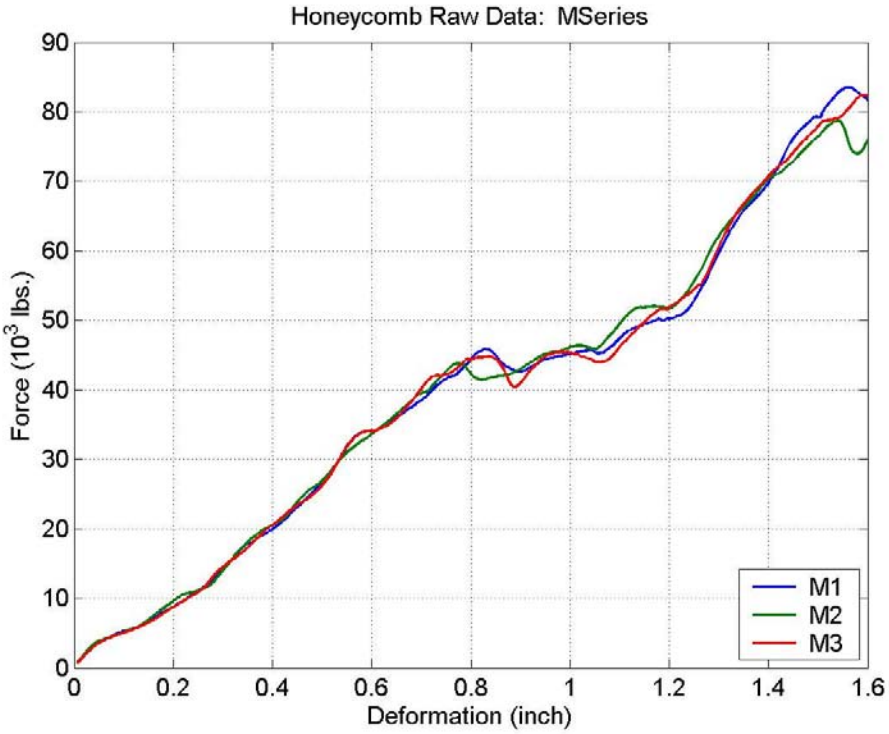

Figure 7-42. Crush force (Series M).

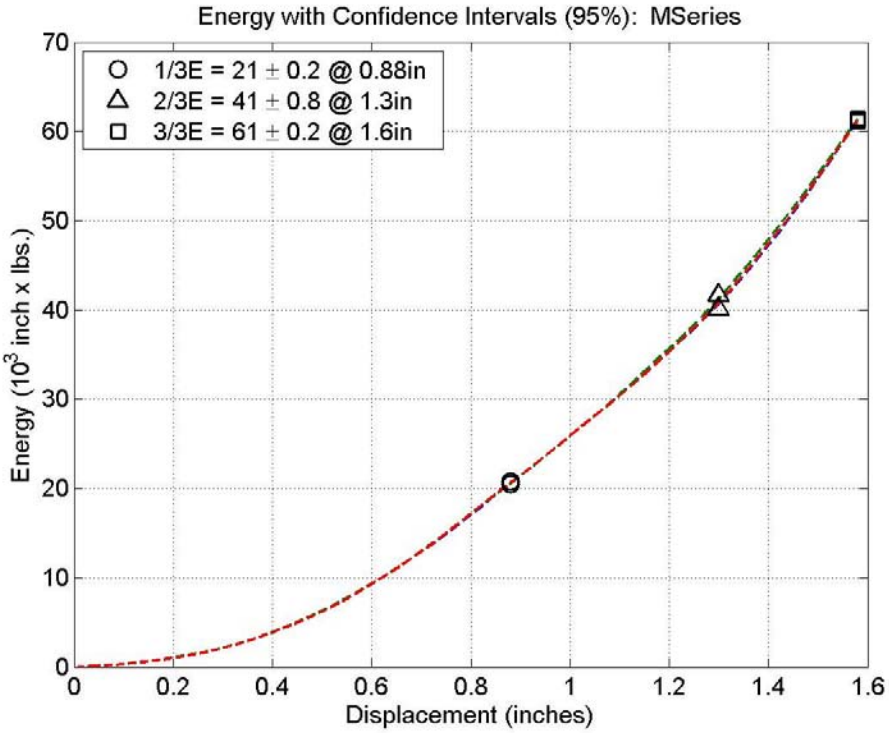

Figure 7-43. Crush force (Series M).

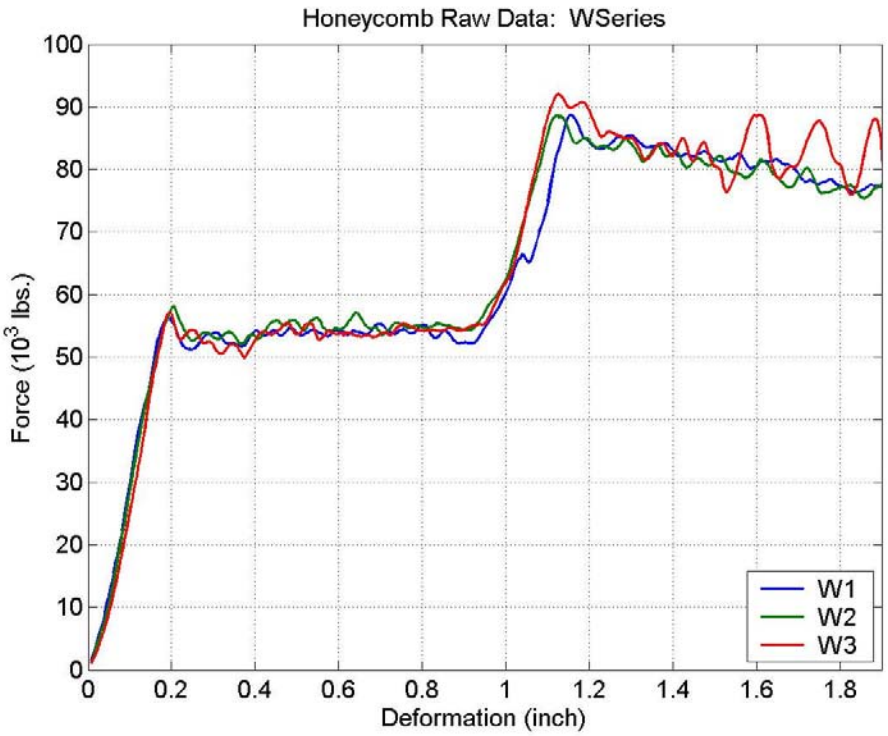

Figure 7-44. Crush force (Series W).

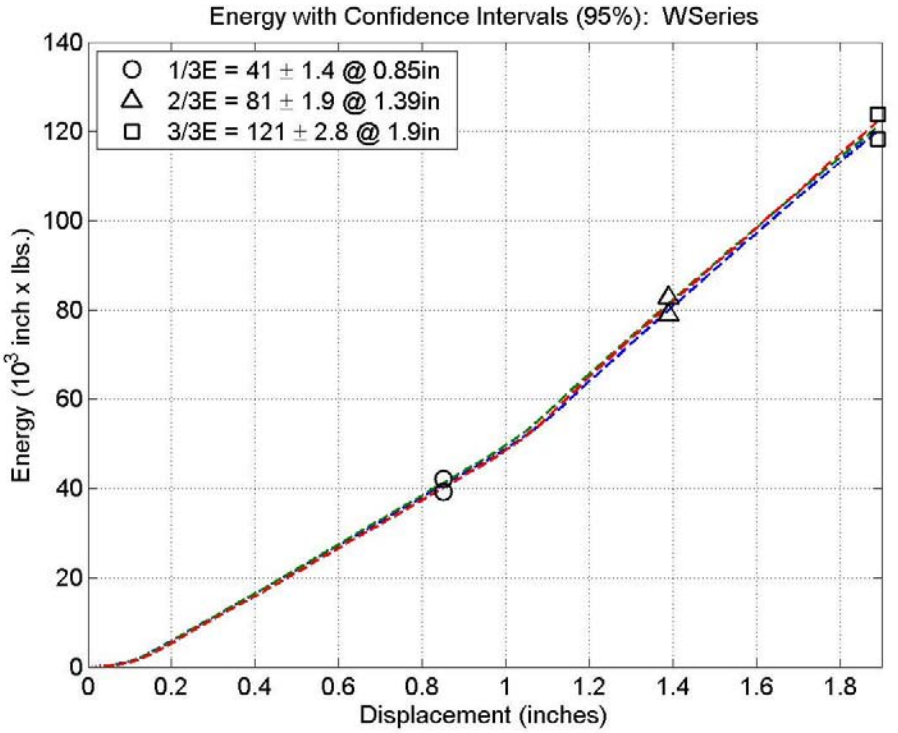

Figure 7-45. Crush force (Series W).

Dynamic Force and Energy Data

The measured force and calculated energy versus deformation data for dynamic test Series S, T, and U are plotted in Figures 7-46 through 7-51. In the energy figures, the colors of the dashed lines correspond to the colors used for each sample in the preceding force figure. The legend of the energy figures displays values of the 1/3, 2/3, and 3/3 validation energies and their corresponding displacements (inches). The 95 percent uncertainty values listed in the legend represents sample-to-sample variability for each configuration. The test names, configurations, and figure numbers are listed in Table 7-9. Test Series R has already been shown in detail in the dynamic test section of this report.

Table 7-9. Dynamic test matrix.

Test Names	Configuration	Temp.	Force	Energy
S1, 2, 3	3° X on L	165 °F	Figure 7-46	Figure 7-47
T1, 2, 3	20° X on L	To	Figure 7-48	Figure 7-49
U1, 2, 3	20° X on L	165 °F	Figure 7-50	Figure 7-51

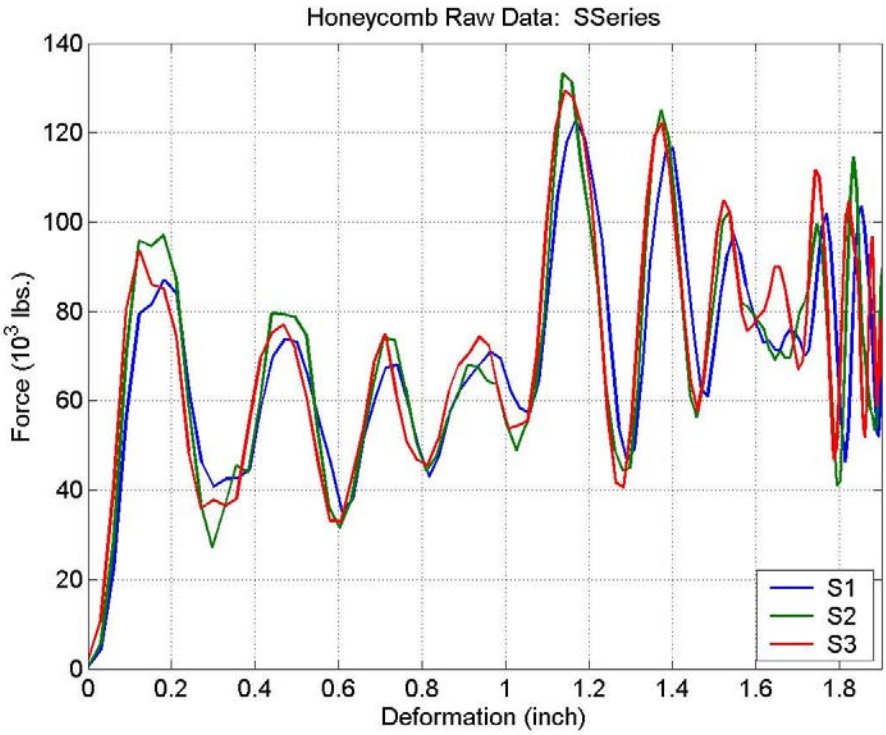

Figure 7-46. Crush force (Series S).

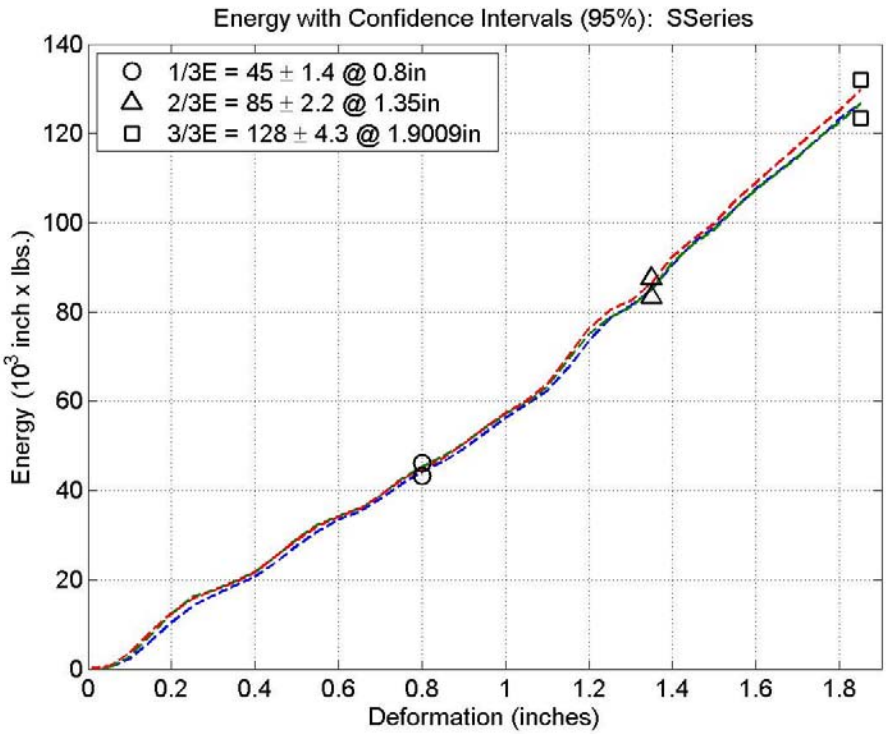

Figure 7-47. Crush energy (Series S).

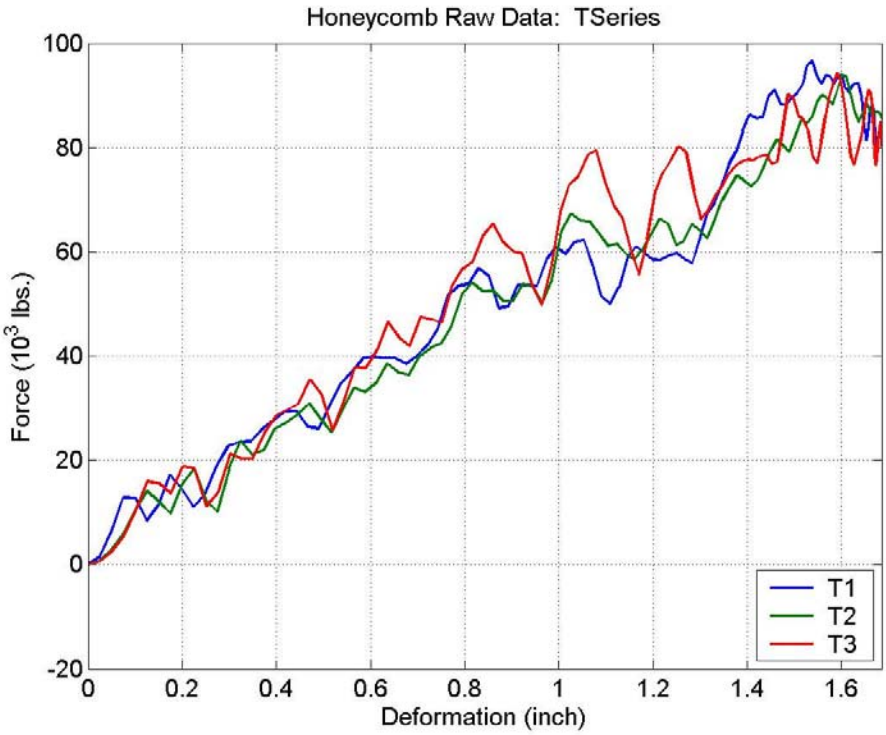

Figure 7-48. Crush force (Series T).

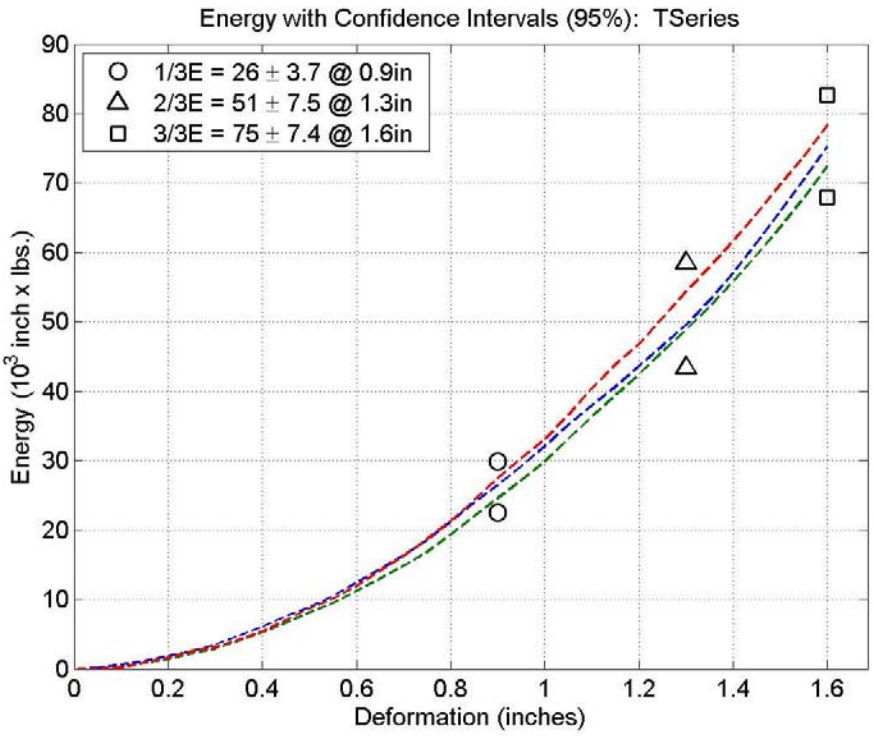

Figure 7-49. Crush energy (Series T).

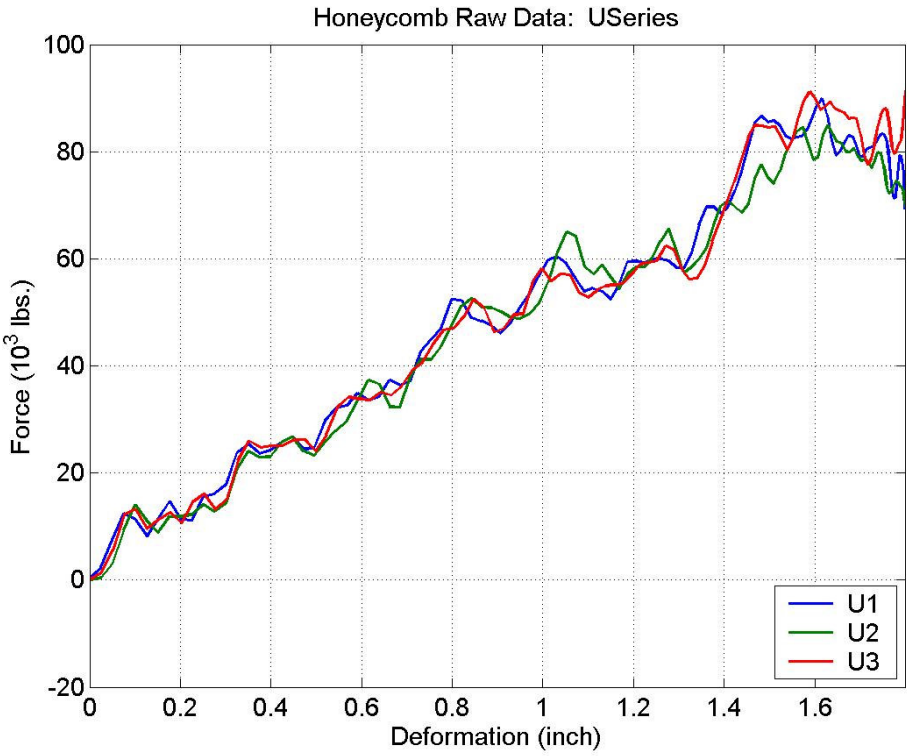

Figure 7-50. Crush force (Series U).

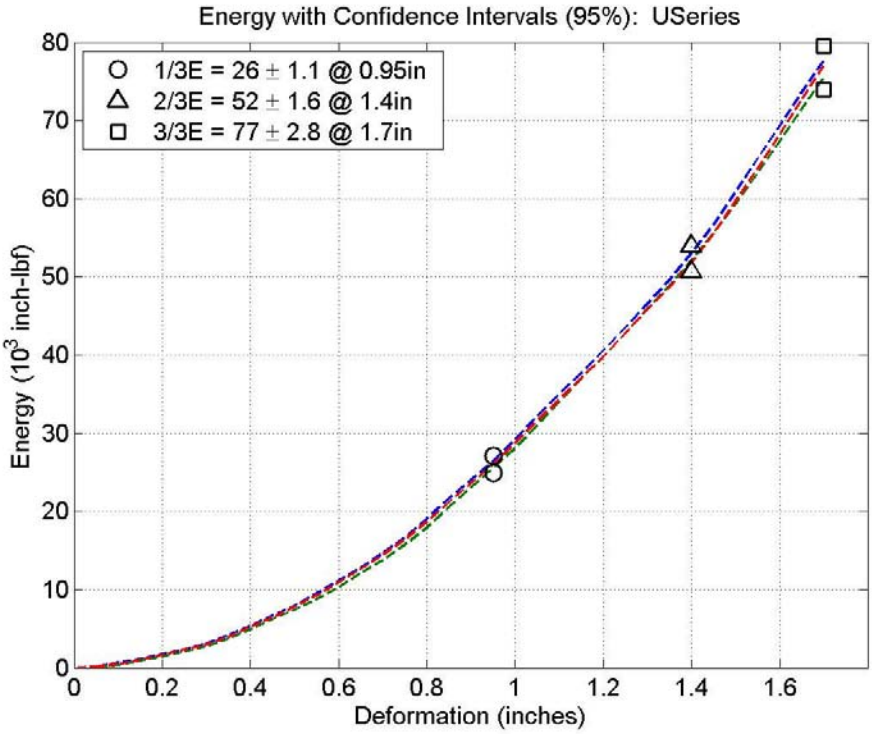

Figure 7-51. Crush energy (Series U).

Summary and Conclusions

Experimental tests were performed on a two-layer honeycomb test structure to provide validation data for the analytical model of the honeycomb material. The two-layer test structure, designed to measure the energy-absorbing qualities of the material in its design application, was tested quasi-statically and dynamically with several configurations for each type of test. Crush energies at 1/3, 2/3, and 3/3 of the total absorbed energy, their corresponding displacements, and the 95 percent confidence intervals, containing sample-to-sample variability and measurement uncertainty, were calculated from the test results. These energies are to be used as the validation metric for the analytic model of the honeycomb material.

Several generalizations can be made from the validation test results. For both quasi-static and dynamic tests, an increased AoA results in less energy absorbed by the test structure. The smaller 3° AoA allows the honeycomb to absorb the energy along its strong t-axis without the shearing strains involved in the larger 20º AoA. The orientation of the segmented honeycomb (x orientation, + orientation) at the top of the two-layer test structure has little to no effect on the energy-absorbing qualities of the honeycomb in a quasi-static environment. Increasing the temperature of the test structure resulted in a small decrease of the energy-absorbing property of the honeycomb material for both static and dynamic environments. Finally, the dynamic tests were shown to absorb more energy than the quasi-static tests, due to the increased crush strength of the honeycomb that is caused by the dynamic strains.

References

1. *Mechanical Properties of Hexcel Honeycomb*, TSB-120, Hexcel Corporation, Dublin, CA, 1992.

2. Bitzer, T., *Honeycomb Technology*. Chapman & Hall, London, UK, 1997.

3. Lu, W.-Y. and Terry D. Hinnerichs, *Crush of High Density Aluminum Honeycombs*, IMECE/AMD-25453, 2001.

4. Lu, W.-Y., J. Korellis, and T. Hinnerichs, *Shear Deformation of High Density Aluminum Honeycombs*, IMECE/AMD-44092, 2003.

5. Walpole, Ronald E., Raymond H. Meyers, and Sharon Myers, *Probability and Statistics for Engineers and Scientists*, 6th ed., Prentice Hall, New Jersey, 1998.

6. Colman, Hugh W., and W. Glenn Steele, *Experimentation and Uncertainty Analysis for Engineers*, 2nd ed., John Wiley and Sons, Inc., New York, NY, 1999.

7. http://www-irn.sandia.gov/afsec/facility/mech.htm (Internal Sandia website), 2004.

8. Stasiunas, E. C. and T. Hinnerichs, Axial Crush Strength of Tape-confined and Segmented Honeycomb, Sandia National Laboratories memo, November 2004.

Intentionally Left Blank

CHAPTER 8. TIER III VALIDATION: LATERAL CRUSH

Eric C. Stasiunas, Thomas G. Carne, and Terry Hinnerichs

Introduction

Validation experiments were performed on honeycomb disks in order to evaluate the energy absorption of the material in a quasi-static, lateral crush environment. Once the honeycomb crush energy was calculated from measured force and deformation data, displacements at 1/3, 2/3, and 3/3 of the total absorbed energy and their corresponding 95 percent confidence intervals (CIs) were calculated. These energy and displacement values were the validation metric for the analytical honeycomb model. The deformations at which the honeycomb splitting occurred have been measured as well. The test matrix for the lateral honeycomb crush validation tests is listed in Table 8-1.

Table 8-1. Test matrix.

Series	Configuration	Type	Size	Temp.	Units
A	L orientation	Homogeneous	5.1 in. dia. x 2.5 in.	T_o	3
B	X orientation	Segmented	5.1 in. dia. x 2.25 in.	T_o	3
C	+ orientation	Segmented	5.1 in. dia. x 2.25 in.	T_o	3

This chapter closely follows Chapter 7. In this work, however, only the honeycomb material itself was crushed—no honeycomb confining structures were included. In addition, the quasi-static crush was performed on honeycomb disks in the lateral direction, as opposed an almost-axial crush as presented in the previous chapter. The calculations used to obtain energy and uncertainty from the measured force versus deformation data, as well at the energy validation metric, are the same as in Chapter 7. Therefore, refer to Chapter 7 for a more thorough explanation of these procedures, if required.

Honeycomb Configurations

Different configurations of the honeycomb material were tested quasi-statically, as listed in the test matrix of Table 8-1. Each tested configuration consisted of three samples. The test samples themselves were disks of honeycomb with a 5.1-in. diameter and two different thicknesses. All testing was performed at room temperature, T_o.

The honeycomb material itself is modeled as an orthotropic material with three defined orthogonal directions—the T, L, and W directions as shown in Figure 8-1—used to fully describe the material parameters. From previous experimentation, the T direction has been proven to exhibit the highest yield strength, followed by the much lower yield strength L direction, followed by even weaker yield strength W direction.

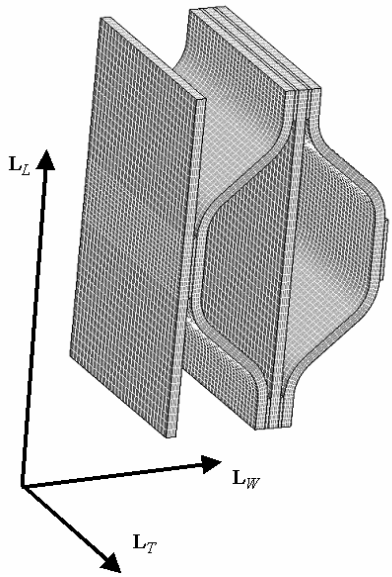

Figure 8-1. Orthogonal directions of honeycomb.

Segmented honeycomb is a design concept that creates a cylindrical section of honeycomb that exhibits approximately the same crush strength in any radial direction. In Figure 8-2, the original honeycomb material has been cut into four 90° wedges and glued together so that the L direction is aligned approximately in the radial direction. The other type of honeycomb tested, homogeneous (unsegmented) honeycomb, is simply a single cut of the original honeycomb material.

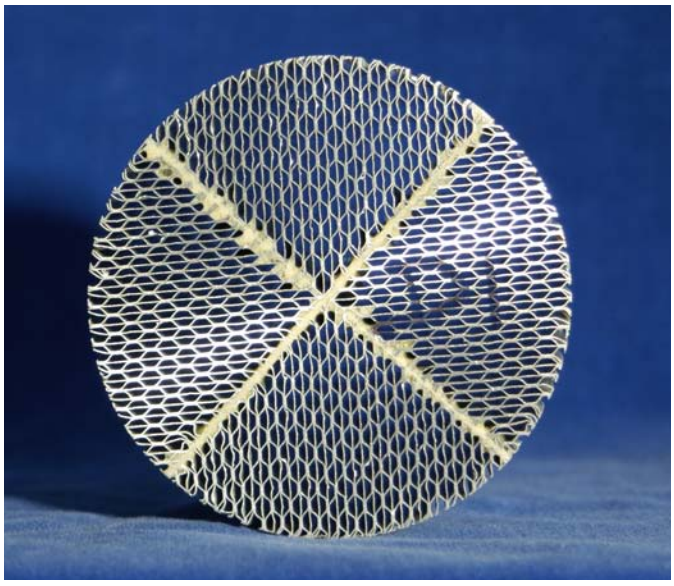

Figure 8-2. Segmented honeycomb.

For the lateral crush of segmented honeycomb, the response of the test sample will differ depending on the exact orientation of the segmented honeycomb in relation to the applied force location. This orientation, defined as X or +, is determined by what point on the segmented honeycomb first comes into contact with the applied force. If the applied force contacts the honeycomb segment located between the glue joints, this is considered an X orientation. Alternately, if the applied force contacts the honeycomb at a glue joint, this is considered a + orientation. A diagram illustrating the two orientations can be seen in Figure 8-3. The thick, black lines drawn on the honeycomb disks represent the glue used to bond the honeycomb segments together.

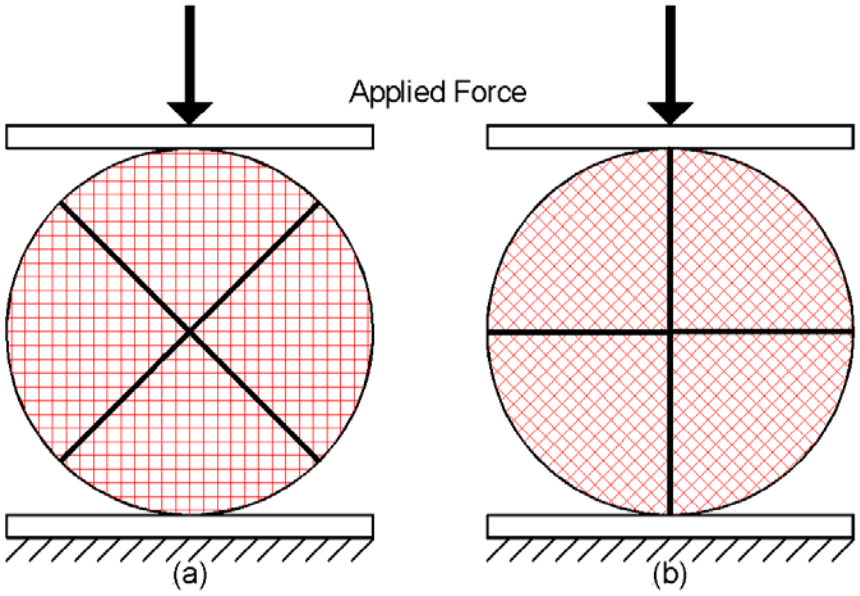

Figure 8-3. Segmented honeycomb (a) X orientation (b) + orientation.

Validation Metric

The metric used for validating the analytic honeycomb model was the energy absorbed during crush, or crush energy (in.-lb). Energy was not measured directly during the quasi-static test but it was calculated from the integration of the force as a function of the displacement. The crush energy metric was determined as the best metric for validation purposes since the ability to absorb energy is the critical design feature of the honeycomb material.

The first step in validating the honeycomb model involved defining a total crush displacement from the measured data, for each test configuration. Next, the total energy absorbed during this crush displacement was calculated from the force data. Finally, the honeycomb crush displacement values corresponding to the 1/3, 2/3, and 3/3 energy values were determined. These energy and displacement values will provide validation data for the analytical model and will help determine whether the model is acceptable.

Validation Experiments

Quasi-static testing provided a way to obtain quality force and lateral crush displacement data from the honeycomb test structures through precise instrumentation. An MTS load frame from the Sandia Structures Laboratory was used to perform these validation tests with a nominal displacement rate of 1.0 in./min. During the test, force and crush displacement was measured, and a digital camera was used to capture images of the crush process every 5 seconds. Once the test fixture had been crushed approximately 2 in., the test was concluded. The setup for all three test configurations is shown in Figure 8-4.

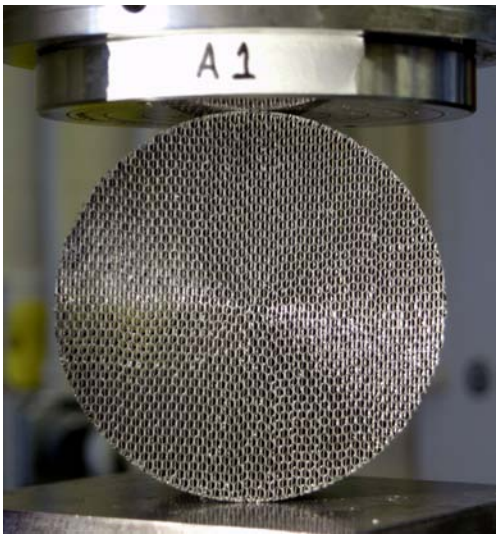

(a) Sample A1 (L orientation)

(b) Sample B1 (X orientation)

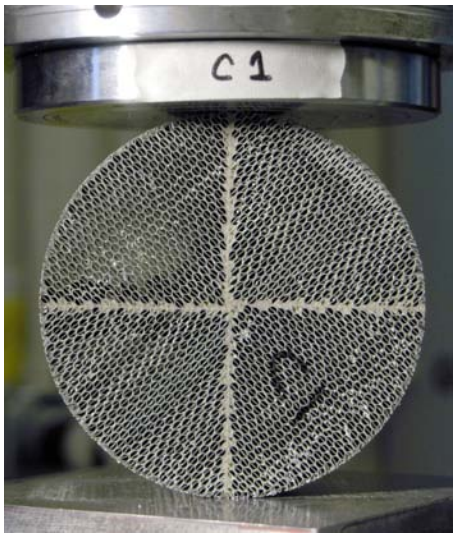

(c) Sample C1 (+ orientation)

Figure 8-4. Quasi-static test setup for all three configurations.

The resulting force and deformation data measured for Series A, B, and C are shown in Figures 8-5 through 8-7, respectively. The units of force and deformation are pounds (lbf) and inches (in.), respectively. Each plot has the same scale of both deformation and force axes for ease of comparison.

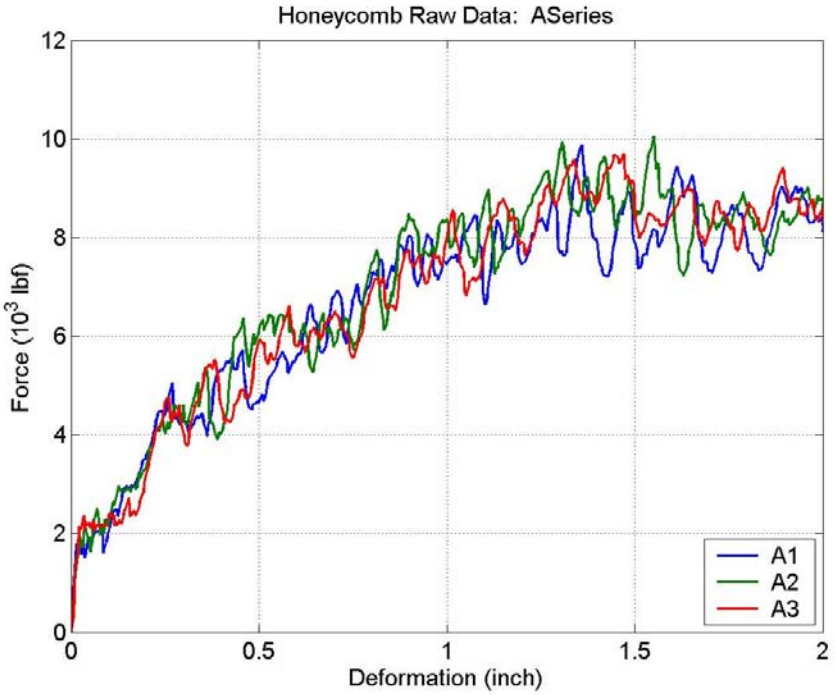

Figure 8-5. Crush Force of Series A (L orientation).

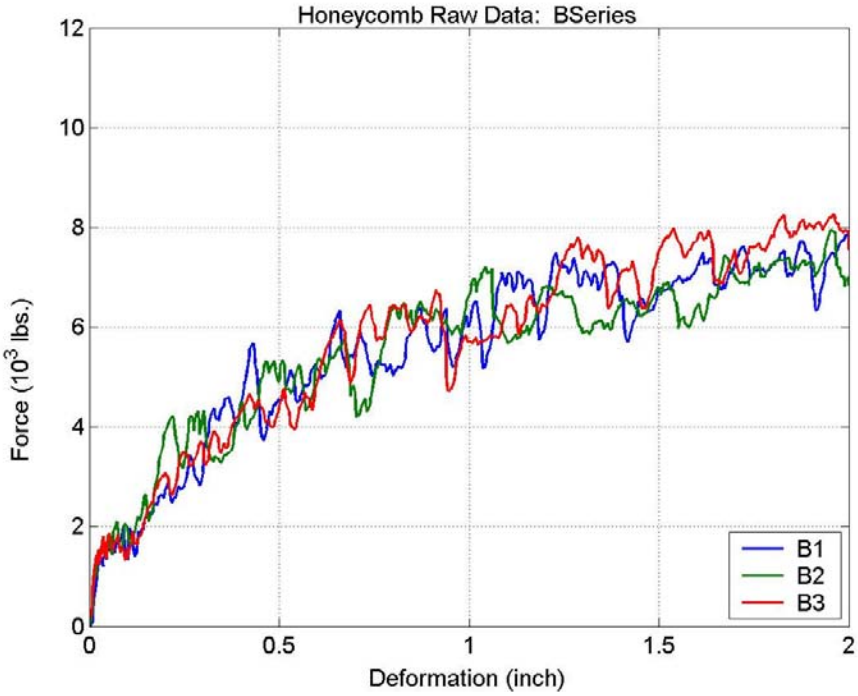

Figure 8-6. Crush Force of Series B (X orientation).

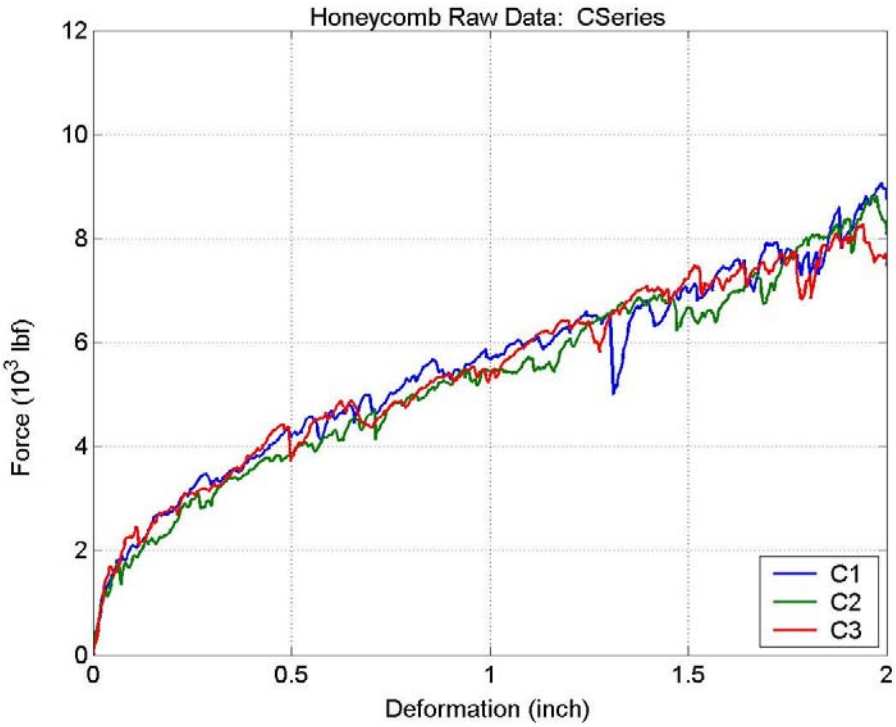

Figure 8-7. Crush Force of Series C (+ orientation)

In the test data for all honeycomb samples, a very small elastic range can be seen from zero to approximately 0.02 in. of deformation. In addition, every sample exhibits jagged force measurements that seem to be random over the measured deformation range. This jaggedness is caused by the plastic buckling of the honeycomb.

The mode of failure for the circular test samples in lateral compression was the separation of the honeycomb layers. An example of honeycomb separation for each test configuration is shown in Figure 8-8. In each case, the separation occurred along the axis of crush. The deformation value at which initial separation occurs is listed in Table 8-2 for Series A and B. For Series C, the separation always occurred at the bonding joint used to hold honeycomb segments together, at the beginning of the crush event.

The data from the test Series A honeycomb configuration, shown in Figure 8-5, were able to support the highest load of all three configurations over the 2-in. deformation range. If the average of the force data is estimated, it seems that the force flattens out at deformations of 1.5 in. and above. This force plateau is more than likely due to separation of the honeycomb that occurs during the crush process, as shown in Figure 8-8(a) for Sample A1, which was confirmed by analyzing the photographs recorded during testing. This analysis revealed that for the L configuration initial honeycomb separation occurred at deformations of approximately 1.4 to 1.6 in.

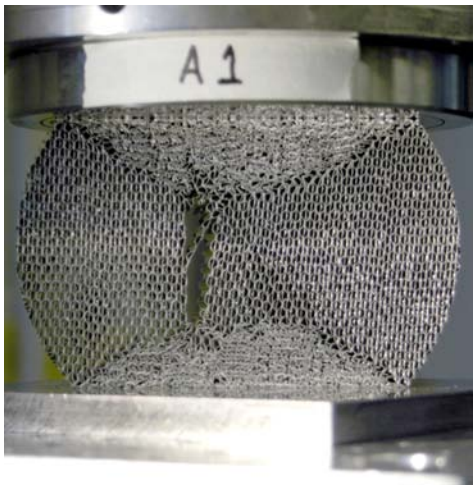

(a) Series A

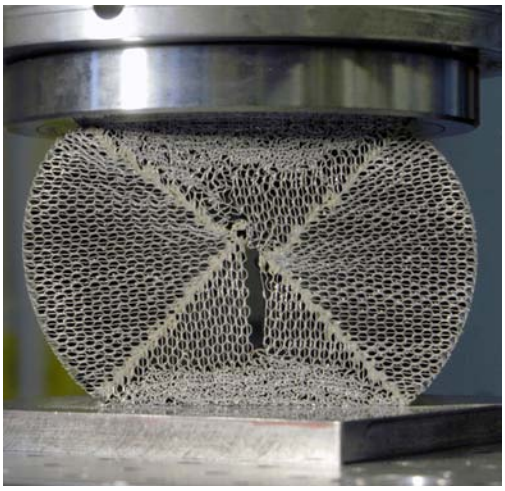

(b) Series B

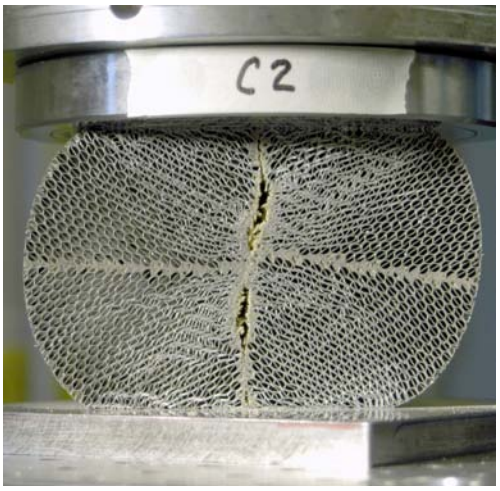

(c) Series C

Figure 8-8. Separation of honeycomb configurations during load.

Table 8-2. Deformation of initial honeycomb separation.

Sample Name	Separation (in.)
A1	1.42
A2	1.59
A3	1.51
B1	1.33
B2	1.04
B3	1.42

The test Series B data in Figure 8-6 exhibit the same force ramp-up as Series A, but does not experience a definite force plateau in the higher deformation range. However, an analysis of the test photos reveal that honeycomb separation does occur at deformations from 1.0 to 1.4 in., as shown in Figure 8-8(b). The segmentation of the honeycomb may prevent higher loads as compared to Series A, but Series B appears less affected by the separation when it does occur.

The data from the final test series, Series C as shown in Figure 8-7, exhibits an almost linear force loading that occurs from 0.5 in. of deformation to the final deformation of 2 in. From the data plot, it appears that the configuration would continue to load up past the 2-in. limit. When Series C failed, it failed along the bonding agent used to glue the four pieces of honeycomb together to form the segmented honeycomb, as shown in Figure 8-8(c).

Using the measured force versus deformation data, the energy absorbed by the honeycomb structure during crush—the crush energy—can be calculated to obtain the desired validation metrics. To calculate the energy, the force curve was integrated numerically, using Equation 8-1, where E is absorbed energy, F is the applied force, and x is the deformation.

$$E(x) = \int_{o}^{x} F(s)ds = \sum_{x_i=0}^{s-x} F(s)\Delta s \qquad \text{(Eq. 8-1)}$$

The crush energy calculated from the force data for test Series A, B, and C is shown in Figures 8-9 through 8-11, respectively. The energy is in units of in.-lbf and the deformation units are inches. In addition to the energy, the measured force data has been superimposed upon the plots as dashed lines.

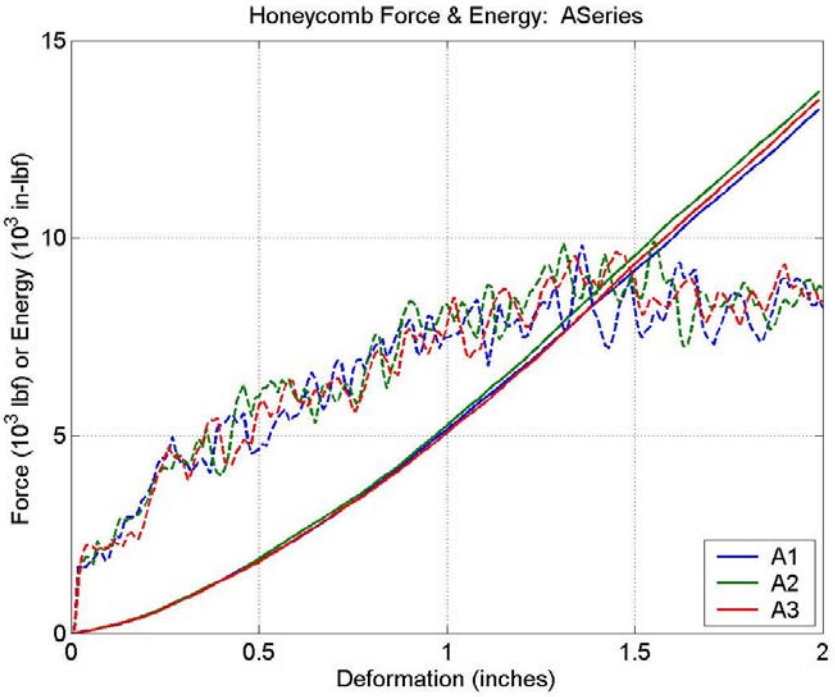

Figure 8-9. Energies of Series A (L orientation).

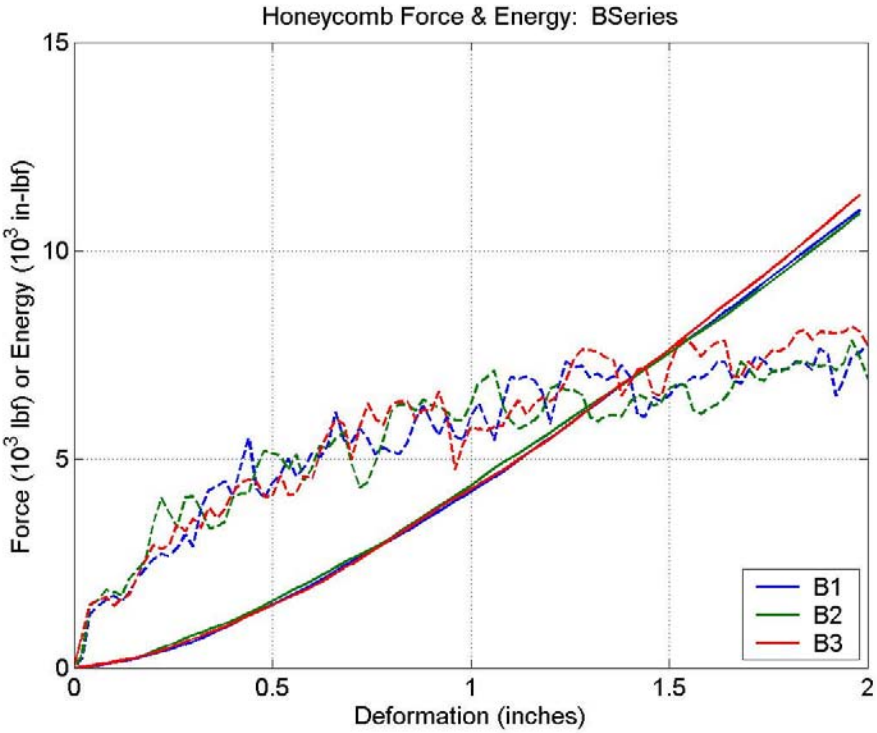

Figure 8-10. Energies of Series B (X orientation).

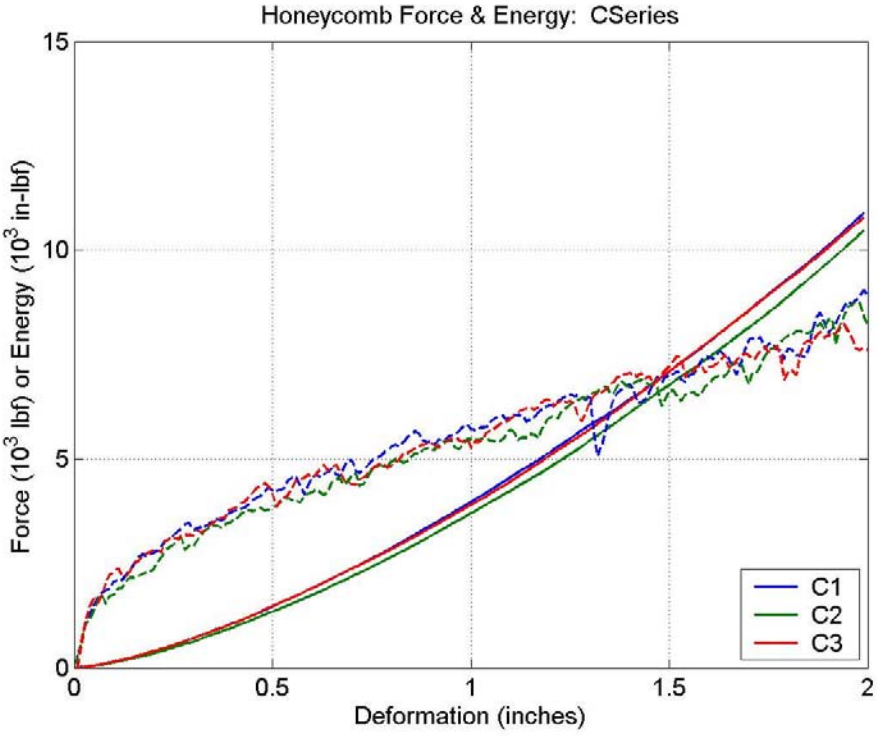

Figure 8-11. Energies of Series C (+ orientation).

With the calculated energy data, the total amount of energy absorbed during the entire crush event could be obtained. The 1/3 and 2/3 total energy values were then calculated, along with their corresponding displacements. Finally, the 95 percent energy confidence intervals were calculated at each displacement to account for sample-to-sample variability.

The validation energies with a 95 percent CI for test Series A, B, and C are shown in Figures 8-12 through 8-14, respectively. The dashed lines represent the energy curves calculated from each test sample. The legend displays the values of the 1/3, 2/3, and 3/3 energies and their corresponding displacements. Again, all figures were plotted on the same scale for ease of comparison.

As an example that can be applied to the rest of the test series, the energy results for Series A will be interpreted from Figure 8-12. At 0.92 in. of deformation (or crush), the amount of energy absorbed by the honeycomb structure is 4.55 ± 0.2 ×103 in.-lb (1/3 of total energy). At 1.46 in. of crush, the amount of energy absorbed is 9.01 ± 0.5 ×103 in.-lb (2/3 total energy), and at the maximum deformation of 2 in., 13.48 ± 0.6 ×103 in.-lb of energy (3/3 energy) has been absorbed. These uncertainty values define the 95 percent CI due only to sample-to-sample variability. The measurement uncertainty for the quasi-static, lateral crush tests was 1.7 percent. The derivation of this value was discussed in detail in Chapter 7.

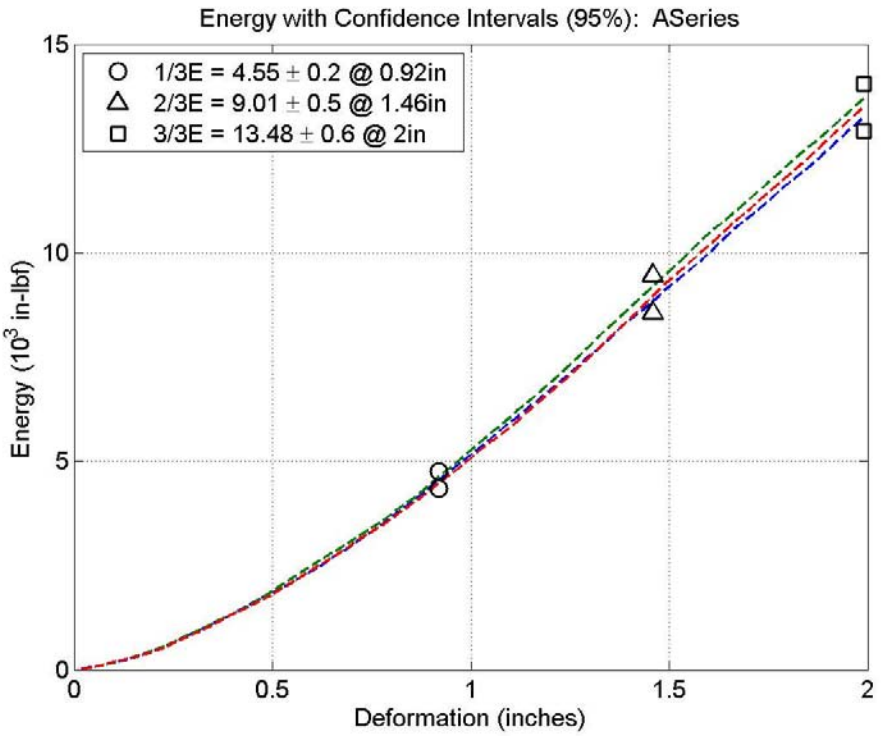

Figure 8-12. Energies of Series A (L orientation).

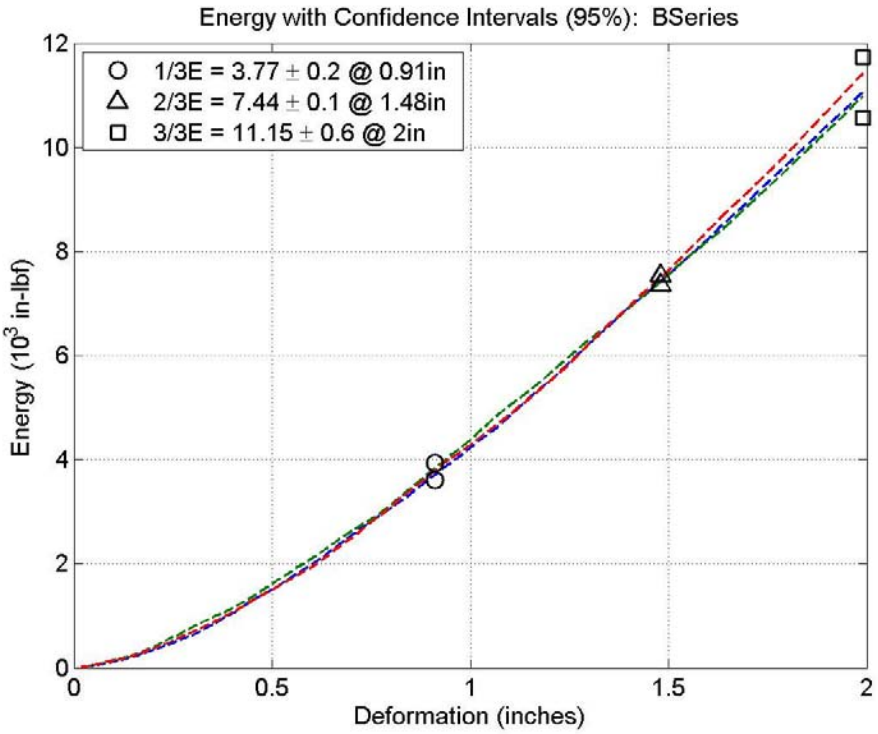

-

Figure 8-13. Energies of Series B (X orientation).

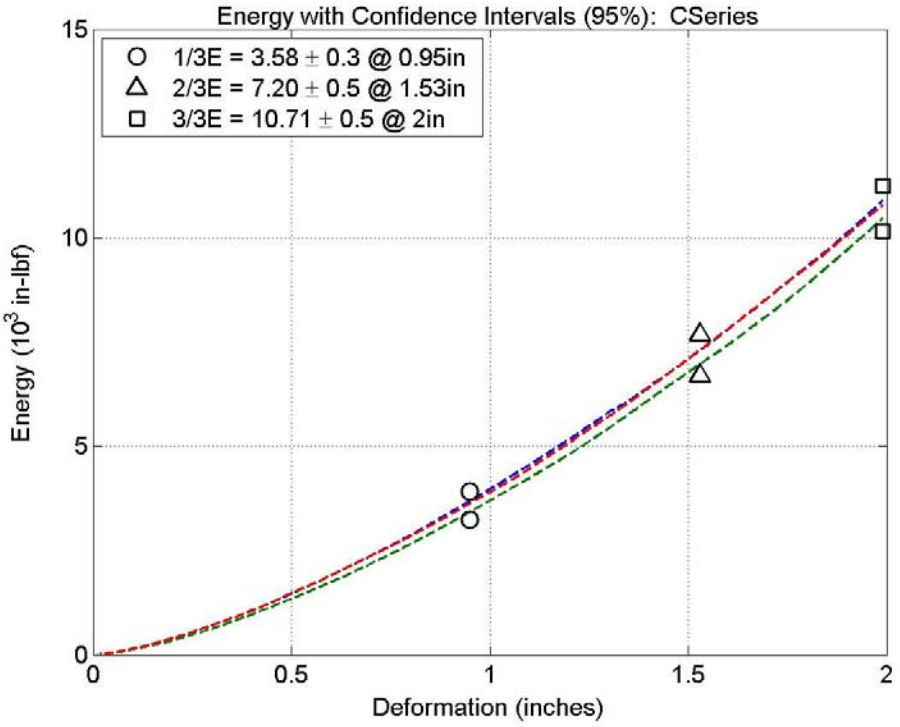

Figure 8-14. Energies of Series C (+ orientation).

The validation crush energies, E, and their corresponding deformations, δ, for all test configurations are shown in Table 8-3. The E_1, E_2, and E_3 columns are the energy values at 1/3, 2/3, and 3/3 of the total energy, and the ±E% columns are the total uncertainties associated with the energy calculations. The total uncertainty values combine the sample-to-sample variability and measurement uncertainty.

Table 8-3. Honeycomb lateral crush energy results.

Sample Name	Configuration	Energy (10^3 in.*lb) with 95% Ci								
		E_1	±E_1%	δ_1	E_2	±E_2%	δ_2	E_3	±E_3%	δ_3
A	L orientation	4.6	5%	0.92	9.0	6%	1.46	13.5	5%	2.00
B	X orientation	3.8	6%	0.91	7.4	2%	1.48	11.2	6%	2.00
C	+ orientation	3.6	9%	0.95	7.2	7%	1.53	10.7	5%	2.00

A direct comparison of the measured forces and calculated energies of the various test configurations is shown in Figure 8-15. For simplification purposes, only the mean values, calculated from the three samples in each configuration, are plotted.

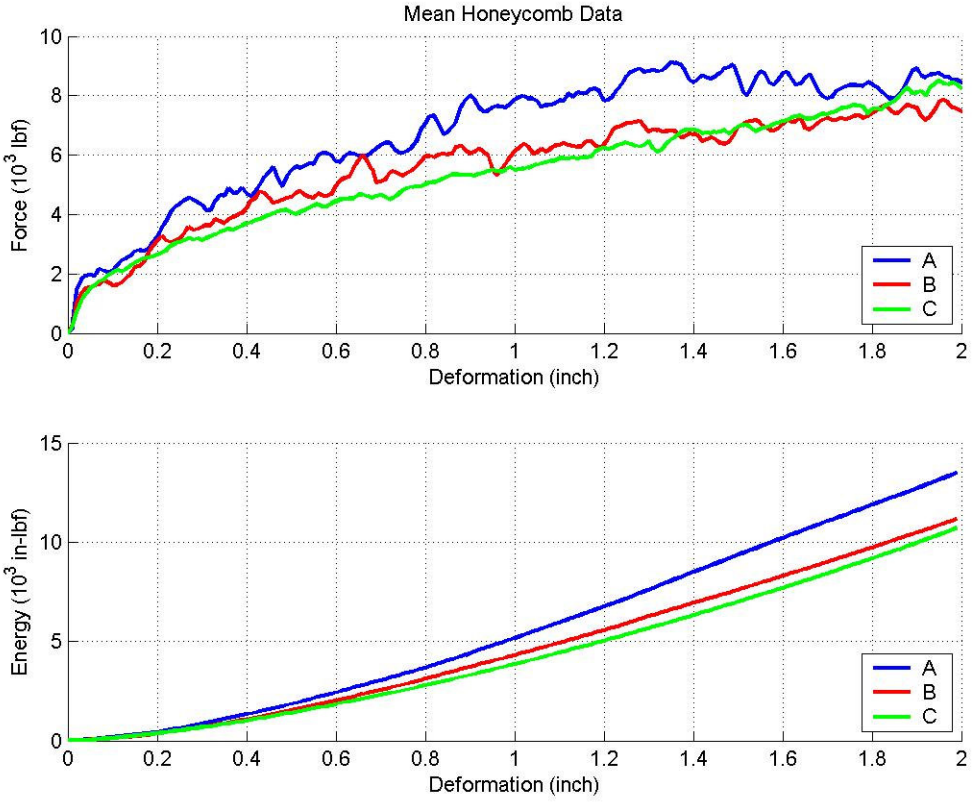

Figure 8-15. Comparisons of honeycomb test series.

From the examination of both Table 8-1 and Figure 8-15, the conclusion can be made that in a lateral crush, unsegmented honeycomb in the L orientation (Series A) absorbs more energy than the other honeycomb orientations. Following Series A in energy absorption is the X orientation segmented honeycomb, Series B. The least amount of energy absorbed during the honeycomb crush was the + orientation segmented honeycomb, Series C. From the figure, the generalization can be made that for a strain of almost 40 percent—2 in. of crush over a 5.1-in. diameter—the orientation of the segmented honeycomb during crush could be considered insignificant due to the negligible difference between the crush energies.

Summary and Conclusions

The results of the lateral crush tests of honeycomb serve two useful purposes. First, the energy absorption properties for each of the three honeycomb configurations were determined, which is useful when designing the structures and honeycomb configurations for applications. Second, the validation energies calculated with their 95 percent CIs are useful for the validation of the analytical models of the honeycomb material. Without the presented validation tests and results, the models would be meaningless.

Intentionally Left Blank

DISTRIBUTION

External distribution:

Hexcel Corporation
Attn: Jim Kindinger
11711 Dublin Blvd.
Dublin, CA 94568

Alcore Inc.
Attn: Bernie Nimeth/Bob Woods
1502 Quarry Drive
Edgewood, MD 21040

Dr. Shen Wu
Ford Motor Company
Science Research Laboratory
Department of Safety Research and Development
SRL Ð MD 2115 20000 Rotunda Drive
P.O. Box 2053
Dearborn, MI 48121

Director
US Army Research Laboratory
Attn Rick Bogdan
AMSRD-ARL-CI-OK-T
2800 Powder Mill Rd
Adelphi, MD 20783-1197

Dr. Tomasz Wierzbicki
Impact and Crashworthiness Laboratory, Rm 5-218
Massachusetts Institute of Technology
Cambridge, MA 02139

2 MS9018 Central Technical Files, 8944

Internal distribution:

1	MS-0325	D. A. Hoke	2615
1	MS-0370	T. G. Trucano	1411
1	MS-0372	J. Pott	1524
1	MS-0372	J. D. Gruda	1524
1	MS-0372	K. W. Gwinn	1524
10	MS-0372	T. D. Hinnerichs	1524
1	MS-0372	T. C. Jones	1524
1	MS-0372	C. S. Lo	1524
1	MS-0372	K. E. Metzinger	1524
1	MS-0372	W. M. Scherzinger	1524
1	MS-0372	J. Jung	1525
1	MS-0372	C. M. Stone	1525
1	MS-0372	G. W. Wellman	1525
1	MS-0380	H. S. Morgan	1540
1	MS-0384	A. C. Ratzel	1500
1	MS-0437	R. C. Hartwig	2100
1	MS-0437	J. M. McGlaun	12930
1	MS-0447	J. G. Lewis	2111
1	MS-0447	K. R. Eklund	2111
1	MS-0447	J. A. Rohwer	2111
1	MS-0447	C. Post	2111
1	MS-0447	W. T. Reutzel	2111
1	MS-0447	P. D. Hoover	2111
1	MS-0447	J. D. Mangum	2111
1	MS-0453	M. A. Rosenthal	2130
1	MS-0457	J. S. Rottler	2000
1	MS-0464	T. D. Hernandez	2996
1	MS-0481	J. M. Montoya	2132
1	MS-0481	L. L. Luna	2132
1	MS-0481	D. R. Martinez	2136
1	MS-0521	J. L. Moya	2540
1	MS-0529	G. K. Froehlich	5345
1	MS-0557	D. B. Clauss	1521
1	MS-0557	V. I. Bateman	1521
1	MS-0557	R. A. May	1522
1	MS-0557	E. C. Stasiunas	1521
1	MS-0557	T. G. Carne	1525
1	MS-0632	V. O. Willan	2916
1	MS-0634	D. J. Giersch	2951
1	MS-0718	D. J. Ammerman	6141
1	MS-0774	E. M. Pulling	2991
1	MS-0828	M. Pilch	1533
1	MS-0828	V. J. Romero	1533
1	MS-0836	E. S. Hertel	1516

1	MS-0842	M. K. Neilsen	1526
1	MS-0847	P. J. Wilson	1520
1	MS-0847	T. J. Baca	1523
1	MS-0847	J. M. Redmond	1526
1	MS-0847	L. N. Kmetyk	1523
1	MS-0965	B. D. Boughton	5714
1	MS-1135	N. T. Davie	1535
1	MS-1393	H. J. Abeyta	12120
1	MS-9042	T. Chen	8776
1	MS-9404	D. M. Kwon	8770
10	MS-9409	W. Lu	8725
2	MS-0899	Technical Library	4536
2	MS-9018	Central Technical Files	8944

This page intentionally left blank